UNIVERSITÀ
DEGLI STUDI
DI PADOVA

Università degli Studi di Padova

CENTRO DI ATENEO DI STUDI E ATTIVITÀ SPAZIALI "G. COLOMBO"
Corso di Dottorato di Ricerca in: Scienze Tecnologie e Misure Spaziali
Curricolo: Scienze e Tecnologie per Applicazioni Satellitari e Aeronautiche

XXXI CICLO

Quantum Optics Experiments in Space

Dottorando:
Francesco Vedovato

Supervisore:
Ch. mo Prof. Paolo Villoresi

Coordinatore:
Ch. mo Prof. Giampiero Naletto

To my father Redi,
my mother Stefania,
and my sister Elisabetta
with no doubt whatsoever

Table of Contents

Sommario

Da sempre lo Spazio è stato fonte di ispirazione per lo sviluppo del pensiero scientifico, tecnologico, artistico, filosofico e religioso per tutta l'umanità. Le esplorazioni spaziali hanno segnato la storia del XX secolo, portando un incredibile sviluppo tecnologico e permettendo di investigare i fenomeni naturali a scale e dettagli che semplicemente non si possono ottenere restando sulla Terra. Oggi lo Spazio è il banco di prova di una nuova *rivoluzione quantistica*, che annuncia di poter cambiare il modo in cui oggigiorno comunichiamo, misuriamo e facciamo di conto, grazie all'utilizzo e al controllo di ciò che avviene su scala microscopica. Infatti, la teoria quantistica, nata all'inizio del XX secolo proprio per descrivere il comportamento delle particelle elementari costituenti la Natura, ha raggiunto oggi un grado di affidabilità strabiliante. Come qualsiasi teoria scientifica infatti, la Meccanica Quantistica è valida entro i confini in cui è stata verificata sperimentalmente, e lo Spazio è il palcoscenico principale in cui poter validare le predizioni della teoria quantistica a grandi scale, in un dominio completamente diverso da quello microscopico entro cui è stata ideata. I progressi tecnologici nel campo della *fotonica*, che permette la manipolazione e il controllo dei singoli quanti di luce, i fotoni, rendono oggi fattibili test fondamentali di Meccanica Quantistica nello Spazio, esperimenti in cui indagare, per esempio, se l'*entanglement* si mantiene anche a migliaia di chilometri o se il *dualismo onda-corpuscolo* si manifesta anche dopo un viaggio spaziale. Inoltre, lo Spazio offre di per sé accesso a regimi *relativistici* in cui le velocità e le distanze in gioco possono permettere di indagare il puzzle irrisolto della fisica moderna, l'unione di Meccanica Quantistica e gravitazione. Per queste ragioni, questa tesi è dedicata agli *esperimenti di Ottica Quantistica nello Spazio* in cui sono stato coinvolto durante il mio dottorato.

Abstract

Space has always been a primary source of inspiration for the development of the scientific, technological, artistic, philosophical and religious thinking of the whole humankind. Space explorations marked the history of the XX century, bringing an incredible technological advancement and allowing to investigate the natural phenomena over scales and into details which are simply not available on Earth. Nowadays, the Space is the benchmark of the new *quantum revolution*, which promises to change the way we communicate, measure and calculate, thank to the exploitation and the control of what happens at the microscopic scale. Indeed, the quantum theory, born at the beginning of the XX century to describe the behaviour of the elementary particles of Nature, has reached today an incredible reliability. As any scientific theory, Quantum Mechanics is valid within the limits in which it has been experimentally verified, and the Space is the main stage where to validate quantum predictions at large scales, in a domain that is completely different with respect to the microscopic one from which it moved. The technological advances in *photonics*, which allows the manipulation and the control of the single quanta of light, the photons, make today feasible fundamental tests of Quantum Mechanics in Space, experiments to investigate, for example, if *entanglement* is preserved along thousands of kilometers or if the *wave-particle duality* survives even after a Space trip. Furthermore, Space makes available *relativistic* regimes, in which the velocities and the distances could allow to experimentally investigate the unresolved puzzle of modern physics, that is, the interplay between Quantum Mechanics and gravitation. For these reasons, this thesis is dedicated to the *Quantum Optics experiment in Space* I have been involved during my PhD.

List of acronyms

ASI	Italian Space Agency (Agenzia Spaziale Italiana)
BS	Beam Splitter
CCR	Corner Cube Retroreflector
CHSH	Clauser-Horne-Shimony-Holt
CW	Continuous Wave
FPGA	Field Programmable Gate Array
GNSS	Global Navigation Satellite Service
HWP	Half waveplate
ILRS	International Laser Ranging Service
LCR	Liquid Crystal Retarder
LEO	Low Earth Orbit
MEO	Medium Earth Orbit
MLRO	Matera Laser Ranging Observatory
MZI	Mach-Zehnder Interferometer
PAT	Pointing, Acquisition and Tracking
PBS	Polarizing Beam Splitter
PID	Proportional-Integral-Derivative
PM	Phase-Modulator
POVM	Positive Operator Valued Measure
QKD	Quantum Key Distribution
QWP	Quarter waveplate
QRNG	Quantum Random Number Generator
RTT	Round Trip Time
SHG	Second Harmonic Generation
SLR	Satellite Laser Ranging
SNR	Signal To Noise Ratio
SPAD	Single Photon Avalanche Diode
SPDC	Spontaneous Parametric Down Conversion
TB	Time-bin

Introduction to Thesis Contents

This thesis work is dedicated to the Quantum Optics experiments I took part in during my PhD activities at the *Luxor Laboratories* at the *Institute of Photonics and Nanotechnology* (IFN) of the *National Council Research* (CNR) and at the *Matera Laser Ranging Observatory* (MLRO) of the *Italian Space Agency* (ASI). My work was part of the activities in experimental Quantum Optics conducted by the *QuantumFuture* group led by my supervisor prof. Paolo Villoresi at the *Department of Information Engineering* of the *University of Padova*. Part of my work was also supported by the project *Moonlight-2* of the *National Institute for Nuclear Physics* (INFN).

The work presented here is well placed within the context of *quantum communications*, a research field ranging from fundamental tests of physics, e.g. Quantum Mechanics, over long distances, to the implementation of Quantum Information protocols in photonics free-space and fiber-based systems. In particular, my works are related to *Space* quantum communications, which could guarantee, in the next future, the security of the telecommunications at the global scale and also open new possibilities for testing the implications and exploiting the applications of Quantum Mechanics around the planet and beyond.

Chapter 1 and 2 are two introductory chapters in which I will focus on the machinery needed to understand the contents of this thesis work by selecting material from standard textbooks on Quantum Mechanics and Quantum Optics. These chapters can be considered the minimum baggage of an experimenter working on photonic implementations of Quantum Information protocols, collecting here some useful contents that are usually spread over many different textbooks and papers.

In Chapter 3, I will present the realization of a time-bin entanglement source not affected by the post-selection loophole, which was part of the activities performed at Luxor Laboratories. I followed the whole development of the source, from the design of the optical setup to the assembling, as well as the data acquisition and analysis. These activities ended with the publication of the relative manuscript in *Physical Review Letters* [F. Vedovato *et al., Postselection-Loophole-Free Bell Violation with Genuine Time-Bin Entanglement*, Phys. Rev. Lett. **121**, 190401 (2018)], of which I am the first author.

In Chapter 4, I will present the motivations and goals behind Space quantum communication and then I will focus on the general idea of the two-way experiments I took part in at MLRO. At the end of this chapter, I will focus on the last two experiments I was

involved in the last year of my PhD, namely the single photon exchange with a terminal of the Russian GNSS constellation GLONASS [L. Calderaro *et al.*, *Towards Quantum Communication from Global Navigation Satellite System*, Quantum Science and Technology *(in press)*; preprint available at arXiv:1804.05022 [quant-ph] (2018) and the preliminary test performed for establishing a Quantum Key Distribution link with the Chinese quantum satellite Micius.

In Chapter 5, I will present the first experiment I was involved in during my PhD, regarding the observation of single-photon interference exploiting time-bin encoding along satellite-ground channels. I took part in the whole experiment, from the design of the optical setup and the preliminary tests at Luxor Laboratories (in particular, I designed the double $4f$ system), to the assembling and data acquisition at MLRO. Then, I focused on the data analysis finding a method to high-light the interference effect even in the presence of low visibility by exploiting the satellite-induced modulation in the interference pattern. I participated in writing the manuscript and in the peer-review process, which ended with the publication in *Physical Review Letters* [G. Vallone *et al.*, *Interference at the Single Photon Level Along Satellite-Ground Channels*, Phys. Rev. Lett. **116**, 253601 (2016)].

In Chapter 6, I will present the experiment which mostly kept me busy during my PhD, that is, the first Space implementation of Wheeler's delayed-choice experiment. I was the person in charge of this experiment, and I took part in all the experimental phases, from the design and the preliminary tests, to the data acquisition and analysis. My colleague Dr. Costantino Agnesi and I mostly wrote the draft of the manuscript, and we managed the peer-review process, which ended with the publication in *Science Advances* [F. Vedovato *et al.*, *Extending Wheeler's delayed-choice experiment to space*, Sci. Adv. **3**, e1701180 (2017)], of which we are the first authors.

Chapter 1

Elements of Quantum Mechanics

In this introductory chapter, we will present some basic elements of Quantum Mechanics which are needed to understand the contents of this thesis work. First, a brief review of the mathematical formalism of quantum theory is presented, then two peculiar traits of of Quantum Mechanics, *entanglement* and *non-locality*, are described in more details.

The contents of this chapter are a selection of what can be found in standard textbooks on Quantum Mechanics, as [1, 2, 3, 4, 5, 6].

Quantum properties of light can be exploited, for example, to generate random numbers.

1.1 The quantum mechanical formalism

In this section we will present the postulates of Quantum Mechanics and some basic elements of Quantum Information theory. This section is inspired by the clear presentation given in [6].

1.1.1 Quantum states, evolution and measurements

The basic laws of Quantum Mechanics can be cast in four postulates, which describe how to represent the state of a physical system, how such system evolves until it is "measured", how to carry out measurements and how to describe a system which consists of more subsystems. Since we will deal with Quantum Optics experiments in which the relevant degrees of freedom can take only a finite number of values, typically two, we will describe only quantum systems of finite dimension. The postulates of Quantum Mechanics can be written as:

1. *States*. Associated to any isolated physical system is a *Hilbert space* $\mathcal{H} \simeq \mathbb{C}^d$ of dimension d. The physical state of the system is completely described by a unit vector ψ in the Hilbert space. The *state vector* is represented by the symbol $|\psi\rangle \in \mathcal{H}$ by using the Dirac notation.
2. *Evolution*. The evolution of a closed quantum system is described by a *unitary transformation*, i.e., an unitary operator acting on the Hilbert space $\mathcal{H}$. The state $|\psi(t)\rangle$ of the system at time t is related to the state $|\psi(t')\rangle$ of the system at time t' by a unitary operator $\hat{U}(t,t')$ which depends only on the times t and t',
$$\left|\psi(t')\right\rangle = \hat{U}(t,t')|\psi(t)\rangle \ . \tag{1.1}$$
3. *Measurements*. Quantum measurements are described by a collection of *measurement operators* $\{\hat{\mathcal{M}}_m\}$ where m is a M-valued symbol, e.g. $m = 1,\ldots,M$. These operators act on the Hilbert space $\mathcal{H}$ and the index m labels the measurement outcomes that may occur in the observations.
   If $|\psi\rangle$ is the state of the system immediately before the measurement, then the probability that result m occurs is given by
$$p(m) = \langle\psi|\,\hat{\mathcal{M}}_m^\dagger \hat{\mathcal{M}}_m\,|\psi\rangle \ , \tag{1.2}$$
   where $\langle\psi|$ is the dual to $|\psi\rangle$ and $\hat{\mathcal{M}}_m^\dagger$ is the adjoint of operator $\hat{\mathcal{M}}_m$. The state of the system immediately after the measurement becomes
$$\left|\psi'\right\rangle = \frac{1}{\sqrt{p(m)}}\hat{\mathcal{M}}_m\,|\psi\rangle \ . \tag{1.3}$$

The measurement operators must satisfy the *completeness relation*

$$\sum_m \hat{\mathcal{M}}_m^\dagger \hat{\mathcal{M}}_m = \mathbb{1}_{\mathcal{H}} \,, \tag{1.4}$$

where $\mathbb{1}_{\mathcal{H}}$ is the identity operator.

4. *Composite systems*. The Hilbert space $\mathcal{H}$ of a composite physical system is the tensor product of the Hilbert spaces $\mathcal{H}_j$ of the different subsystems

$$\mathcal{H} = \bigotimes_j \mathcal{H}_j \,. \tag{1.5}$$

If the subsystems are numbered 1 through N and the j-th system is prepared in the state ψ_j, then the joint state $|\Psi\rangle \in \mathcal{H}$ of the total system is

$$|\Psi\rangle = |\psi_1\rangle \otimes |\psi_2\rangle \otimes \cdots \otimes |\psi_N\rangle \,. \tag{1.6}$$

A general collection of measurement operators acting on the composite Hilbert space $\mathcal{H}$ is given by the tensor product of the measurement operators $\hat{\mathcal{M}}_{m_j}$ of the j-th component

$$\hat{\mathcal{M}}_m = \hat{\mathcal{M}}_{m_1} \otimes \hat{\mathcal{M}}_{m_2} \otimes \cdots \otimes \hat{\mathcal{M}}_{m_N} \,, \tag{1.7}$$

which is composed by $M = M_1 M_2 \cdots M_N$ elements. Hence, the probability of obtaining the outcome $m = (m_1, m_2, \ldots, m_N)$ is

$$p(m_1, m_2, \ldots, m_N) = \langle \Psi | \hat{\mathcal{M}}_{m_1} \otimes \hat{\mathcal{M}}_{m_2} \otimes \cdots \otimes \hat{\mathcal{M}}_{m_N} | \Psi \rangle \,. \tag{1.8}$$

We presented the postulates of Quantum Mechanics using the language of *pure states*, assuming that the state of the system is completely known. However, we can suppose that the system is in one of a number of states $|\psi_i\rangle$ with probabilities p_i respectively. The ensemble $\{p_i, |\psi_i\rangle\}$ is an *ensemble of pure states* and the quantum state of the system in this case is a *mixed state* defined by the *density operator*

$$\hat{\rho} := \sum_i p_i \, |\psi_i\rangle\langle\psi_i| \tag{1.9}$$

acting on the Hilbert space $\mathcal{H}$ of the system. It is easy to show that for the density operator defined in (1.9) one has that its *trace* is 1, i.e. $\mathrm{Tr}[\hat{\rho}] = 1$, and $\hat{\rho}$ is a positive operator, i.e., $\langle\varphi|\hat{\rho}|\varphi\rangle \geq 0$ for any $|\varphi\rangle \in \mathcal{H}$, symbolically $\hat{\rho} \geq 0$. It is worth noticing that, conversely, if an operator $\hat{\rho}'$ satisfies $\mathrm{Tr}[\hat{\rho}'] = 1$ and $\hat{\rho}' \geq 0$, it represents the density operator for some ensemble $\{p_i, |\psi_i\rangle\}$. Moreover, two different ensembles of quantum states could give rise to the same density matrix [6].

Regarding the relation between pure and mixed staes, the density operator for a pure state $|\psi\rangle$ has the form $\hat{\rho} = |\psi\rangle\langle\psi|$ and a density operator $\hat{\rho}$ represents a pure state *if and only if* $\mathrm{Tr}\left[\hat{\rho}^2\right] = 1$.

The postulates presented above can be rewritten in the formalism of density operators [6]. Here we limit to observe that the unitary evolution from t to t' takes is given by

$$\hat{\rho}_t \to \hat{\rho}_{t'} = \hat{U}(t,t')\hat{\rho}_t\hat{U}^\dagger(t,t') \tag{1.10}$$

and that the probability to obtain the result m given the measurement operators $\{\hat{\mathcal{M}}_m\}$ and the state $\hat{\rho}$ is

$$p(m) = \mathrm{Tr}\left[\hat{\mathcal{M}}_m^\dagger\hat{\mathcal{M}}_m\hat{\rho}\right] . \tag{1.11}$$

1.1.2 Projective measurements and the POVM formalism

The third postulate about quantum measurement is often given in terms of *projective measurements*, or *von Neumann measurements*, that are a special class of measurements. A projective measurement is described by an *observable*, a Hermitian operator $\hat{\mathcal{O}} = \hat{\mathcal{O}}^\dagger$ acting on the Hilbert space. The observable, being Hermitian, has a spectral decomposition (assuming no degeneracy in its eigenvalues),

$$\hat{\mathcal{O}} = \sum_{m=1}^{d} m\hat{P}_m , \tag{1.12}$$

where $\hat{P}_m$ is the projector ($\hat{P}_m = \hat{P}_m^\dagger = \hat{P}_m^2$) onto the eigenspace of $\hat{\mathcal{O}}$ with eigenvalue m, which naturally labels the possible outcomes of a measurement of the observable $\hat{\mathcal{O}}$. Hence, projective measurements are a special case of measurements operators: each $\hat{P}_m$ is a measurement operator in the collection $\{\hat{P}_m\}$. Hence, upon measuring the state $|\psi\rangle$, the probability of getting the result m is given by, according to (1.2),

$$p(m) = \langle\psi|\hat{P}_m|\psi\rangle \tag{1.13}$$

and, given the outcome m occurred, the state after the measurement is

$$|\psi'\rangle = \frac{\hat{P}_m|\psi\rangle}{\sqrt{\langle\psi|\hat{P}_m|\psi\rangle}} . \tag{1.14}$$

The average value of the observable $\hat{\mathcal{O}}$ if the system is described by the pure state $|\psi\rangle$ is given by

$$\langle\hat{\mathcal{O}}\rangle_{|\psi\rangle} = \sum_m m\,p(m) = \sum_m m\,\langle\psi|\hat{P}_m|\psi\rangle = \langle\psi|\hat{\mathcal{O}}|\psi\rangle , \tag{1.15}$$

while, if the system is in the mixed state (1.9), we have

$$\langle \hat{\mathcal{O}} \rangle_{\hat{\rho}} = \sum_i p_i \langle \psi_i | \hat{\mathcal{O}} | \psi_i \rangle = \mathrm{Tr}\left[\hat{\rho} \hat{\mathcal{O}} \right] . \tag{1.16}$$

It is worth noticing that, rather than giving the observable $\hat{\mathcal{O}}$, often a projective measurement is provided by listing a complete set of d orthogonal projectors $\hat{P}_m := |m\rangle\langle m|$ using the phrase "measuring in the basis $\{|m\rangle\}$". Indeed, these projectors obey the completeness relation and $\hat{P}_m \hat{P}_n = \hat{P}_m \delta_{mn}$ where δ_{mn} is the Kronecker' symbol: implicitly, the corresponding observable is $\hat{\mathcal{O}} := \sum_{m=1}^{d} m\, |m\rangle\langle m|$.

However, in modern literature the most used measurements are not of the type of von Neumann, which suppose that there exist physical quantities, the observables, that can be measured by the exerimenters. Going beyond this idea, we could assume that the experimenters only perform macroscopic operations, or tests, on quantum systems, which have probabilistic outcomes. This approach is more general than the von Neumann's one and it constitutes the *Positive Operator Valued Measure* (POVM) formalism [4, 6].

Suppose to perform the measurements of the collection $\{\hat{\mathcal{M}}_m\}$ upon the state $\hat{\rho}$ and define the operators $\hat{\Pi}_m := \hat{\mathcal{M}}_m^\dagger \hat{\mathcal{M}}_m$. The properties the operators must obey and linear algebra guarantee that:

$$\hat{\Pi}_m \geq 0 , \tag{1.17}$$

$$\sum_m \hat{\Pi}_m = \mathbb{1}_{\mathcal{H}} , \tag{1.18}$$

$$p(m) = \mathrm{Tr}\left[\hat{\Pi}_m \hat{\rho} \right] . \tag{1.19}$$

The set $\{\hat{\Pi}_m\}$ is sufficient to determine the probabilities of the different measurement outcomes m and it is known as a POVM. It is worth noticing that a set $\{\hat{P}_m\}$ defining a projective measurement is also a POVM through $\hat{\Pi}_m := \hat{P}_m^\dagger \hat{P}_m = \hat{P}_m$.

Suppose now to take an arbitrary set $\{\hat{\Pi}_a\}$ of positive operators (and so self-adjoint $\hat{\Pi}_a = \hat{\Pi}_a^\dagger$) acting on $\mathcal{H}$ which sum up to the identity, i.e., $\sum_a \hat{\Pi}_a = \mathbb{1}_{\mathcal{H}}$, and in which the label a, contrary to projective measurements, spans a range that could be also greater than the dimension d of the Hilbert space. It is possible to show that such set defines a POVM by requiring, in addition, that the probability of obtaining the results labelled a when the system is in the state $\hat{\rho}$ is $p(a) = \mathrm{Tr}\left[\hat{\Pi}_a \hat{\rho} \right]$ [6].

We will use the POVM formalism in analyzing our work on post-selection-free time-bin entanglement in Chapter 3.

1.1.3 The qubit

The *bit* is the basic entity of classical information theory. A bit can take only two values, 0 or 1, representing its state. Similarly, we can represent the quantum analogue to classical bit by defining it as a object living in a 2-dimensional Hilbert space $\mathcal{H}_{1q} \simeq \mathbb{C}^2$. It is usual to define the "computational basis" as $\{|0\rangle, |1\rangle\}$, which, in matrix notation, can be written as

$$|0\rangle := \begin{pmatrix} 1 \\ 0 \end{pmatrix}, \quad |1\rangle := \begin{pmatrix} 0 \\ 1 \end{pmatrix} \tag{1.20}$$

The great difference between bits and qubits is that a qubit can be in a state *other* than $|0\rangle$ or $|1\rangle$. Indeed, any linear combination of these two states, called *superposition*,

$$|\psi\rangle = \alpha\,|0\rangle + \beta\,|1\rangle \ , \tag{1.21}$$

where $\alpha, \beta \in \mathbb{C}$, is also a possible quantum state, provided that

$$|\alpha|^2 + |\beta|^2 = 1 \ . \tag{1.22}$$

An useful representation for a generic qubit can be obtained rewriting (1.21) as

$$|\psi\rangle = \cos\frac{\theta}{2}\,|0\rangle + e^{i\varphi}\sin\frac{\theta}{2}\,|1\rangle \tag{1.23}$$

using the normalization condition (1.22). The angles θ and φ define a point on the unit three-dimensional sphere, called *Bloch sphere*, that is represented in Figure 1.1.

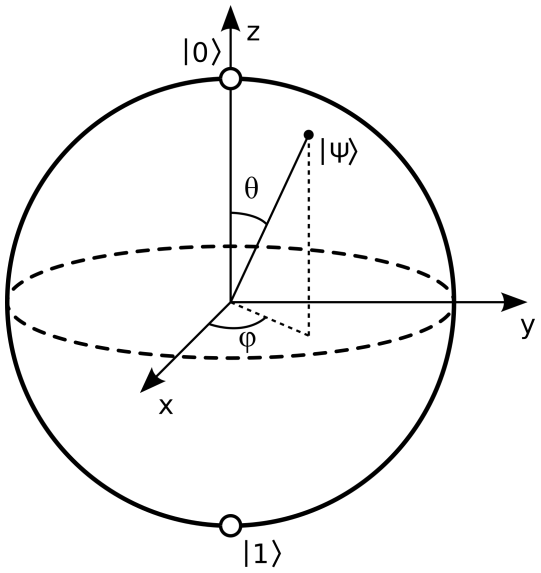

Figure 1.1: Bloch sphere representation of a qubit $|\psi\rangle = \cos\frac{\theta}{2}|0\rangle + e^{i\varphi}\sin\frac{\theta}{2}|1\rangle$. Picture taken from Wikipedia.

In (1.21) the qubit is given by a pure state and it is represented by a point on the surface of the Bloch sphere. On the contrary, an arbitrary density matrix for a mixed one-qubit state may be written as

$$\hat{\rho} = \frac{1}{2}(\mathbb{1}_2 + \mathbf{r}\cdot\boldsymbol{\sigma})\,, \tag{1.24}$$

where $\mathbb{1}_2$ is the 2-dimensional identity matrix, $\mathbf{r}$ is a three-dimensional real vector called *Bloch vector* such that $||\mathbf{r}|| \leq 1$ and $\boldsymbol{\sigma}$ is the "vector" composed by the three *Pauli matrices*

$$\hat{\sigma}_1 = \hat{\sigma}_x := \begin{pmatrix} 0 & 1 \\ 1 & 0 \end{pmatrix},\ \hat{\sigma}_2 = \hat{\sigma}_y := \begin{pmatrix} 0 & -i \\ i & 0 \end{pmatrix},\ \hat{\sigma}_3 = \hat{\sigma}_z := \begin{pmatrix} 1 & 0 \\ 0 & -1 \end{pmatrix}, \tag{1.25}$$

as components. The Pauli matrices respect the commutation relations

$$[\hat{\sigma}_i, \hat{\sigma}_j] = 2i\epsilon_{ijk}\hat{\sigma}_k\,, \tag{1.26}$$

where ϵ_{ijk} is the Levi-Civita symbol. It can be shown that a pure state is characterized by a unit vector $\mathbf{r}$ such that $||\mathbf{r}|| = 1$ that gives a point on the surface of the sphere, while a true mixed state is represented by a point inside the sphere.

Stokes parameters.—It is worth noticing that density matrix of a one-qubit can be expanded as

$$\hat{\rho} = \frac{1}{2}\sum_{i=0}^{3} S_i \hat{\sigma}_i \tag{1.27}$$

where we defined the *Stokes parameters*

$$S_i := \mathrm{Tr}[\hat{\sigma}_i\hat{\rho}] \equiv \langle\hat{\sigma}_i\rangle_\rho \tag{1.28}$$

with $\hat{\sigma}_0 := \mathbb{1}_2$. The Stokes parameters for $i = 1,2,3$ give the components of the Bloch vector $\mathbf{r}$, i.e., $r_i = S_i$. The *degree of polarization* (DOP) of the state $\hat{\rho}$ is then defined as the length of the Bloch vector $\mathbf{r}$

$$\mathrm{DOP}(\rho) := ||\mathbf{r}|| = \sqrt{r_1^2 + r_2^2 + r_3^2}\,. \tag{1.29}$$

Rotations on the Bloch sphere.—The Pauli matrices provide useful unitary matrices when exponentiated, which are called *rotation operators* about the x-, y- or, z-axis of the Bloch sphere. They are defined by (in the convention of [6]):

$$\hat{R}_x(\phi) := e^{-i\frac{\phi}{2}\hat{\sigma}_x} = \cos\frac{\phi}{2}\mathbb{1}_2 - i\sin\frac{\phi}{2}\hat{\sigma}_x = \begin{pmatrix} \cos\frac{\phi}{2} & -i\sin\frac{\phi}{2} \\ -i\sin\frac{\phi}{2} & \cos\frac{\phi}{2} \end{pmatrix} \tag{1.30}$$

$$\hat{R}_y(\phi) := e^{-i\frac{\phi}{2}\hat{\sigma}_y} = \cos\frac{\phi}{2}\mathbb{1}_2 - i\sin\frac{\phi}{2}\hat{\sigma}_y = \begin{pmatrix} \cos\frac{\phi}{2} & -\sin\frac{\phi}{2} \\ \sin\frac{\phi}{2} & \cos\frac{\phi}{2} \end{pmatrix} \tag{1.31}$$

$$\hat{R}_z(\phi) := e^{-i\frac{\phi}{2}\hat{\sigma}_z} = \cos\frac{\phi}{2}\mathbb{1}_2 - i\sin\frac{\phi}{2}\hat{\sigma}_z = \begin{pmatrix} e^{-i\frac{\phi}{2}} & 0 \\ 0 & e^{i\frac{\phi}{2}} \end{pmatrix} \tag{1.32}$$

The effect of a rotation $\hat{R}_i(\phi)$ on a qubit state as in (1.23) is to rotate it by an angle ϕ around the axis specified by $i = x, y, z$ of the Bloch sphere.

It is worth noticing that any unitary operation on a single qubit can be decomposed into three rotations around two specific non-parallel axes. For Quantum Optics purposes, as we will see in the following chapter, we will use the case of rotations around y- and x-axes, i.e. any unitary operation $\hat{U}$ on a single qubit can be decomposed as [6]

$$U = e^{i\alpha}\hat{R}_y(\beta)\hat{R}_x(\gamma)\hat{R}_y(\delta)\,, \tag{1.33}$$

choosing appropriate $\alpha, \beta, \gamma, \delta \in \mathbb{R}$.

It is possible to use any two-level quantum system in order to create a physical qubit. For example, the spin of an electron or two electronic levels of an atom can be considered for qubit realization. For our purpose, the most important physical system to realize a quantum bit is the *photon*, the light particle, as we will describe in Chapter 2.

1.2 Entanglement and Bell's test

The outstanding beauty of Quantum Mechanics relies on its peculiar traits that rend it astonishing far from common sense. Among the others, entanglement and the fact that Quantum Mechanics predictions cannot be described by any *local and realistic* theory are maybe the most disturbing.

1.2.1 Entanglement

Entanglement is a property of two (or more) quantum systems exhibiting *correlations* that cannot be explained by classical physics. The capability of Quantum Mechanics to show such strong correlations is related to the fourth postulate presented above, which rules composite systems.

Suppose we have a quantum system made up of two subsystems A and B, usually called Alice and Bob. The Hilbert space $\mathcal{H}$ of the system is given by

$$\mathcal{H}_{AB} = \mathcal{H}_A \otimes \mathcal{H}_B \tag{1.34}$$

where $\mathcal{H}_A$ and $\mathcal{H}_B$ are the Hilbert spaces for the quantum systems A and B respectively. A pure state $|\psi\rangle \in \mathcal{H}_{AB}$ is called *separable* if there exist two pure states $|a\rangle_A \in \mathcal{H}_A$ and $|b\rangle_B \in \mathcal{H}_B$ such that

$$|\psi\rangle = |a\rangle_A \otimes |b\rangle_B \equiv |a\rangle_A |b\rangle_B \equiv |a_A b_B\rangle \equiv |ab\rangle\ , \tag{1.35}$$

where in the last equalities we introduced a shorter notation for composite states. If the pure state $|\psi\rangle$ is not separable, it is called *entangled*.

In the following we will consider systems made up of two qubits, whose Hilbert space is

$$\mathcal{H}_{2q} = \mathcal{H}_{1q,A} \otimes \mathcal{H}_{1q,B} \simeq \mathbb{C}^2 \otimes \mathbb{C}^2 \,. \tag{1.36}$$

The four states

$$|\Phi^{\pm}\rangle := \frac{1}{\sqrt{2}} \left(|0\rangle_A |0\rangle_B \pm |1\rangle_A |1\rangle_B\right) \,, \tag{1.37}$$

$$|\Psi^{\pm}\rangle := \frac{1}{\sqrt{2}} \left(|0\rangle_A |1\rangle_B \pm |1\rangle_A |0\rangle_B\right) \tag{1.38}$$

are examples of entangled states because they cannot be expressed as a tensor product of two qubit states. They are called *Bell states* and form an orthonormal basis for the Hilbert space $\mathcal{H}_{2q}$ of the two-qubit system.

However, we can be interested in described one of the subsystems, for example Alice, regardless of Bob. Such description can be obtained by using the *reduced density matrix*. Suppose the state of the composite system of Alice and Bob is given by the density matrix $\hat{\rho}_{AB}$. The reduced density matrix for Alice is then defined by

$$\hat{\rho}_A = \mathrm{Tr}_B \left[\hat{\rho}_{AB}\right] \tag{1.39}$$

where the trace operation is now the *partial* trace over the subsystem B, defined as

$$\mathrm{Tr}_B \left[|a_1\rangle\langle a_2| \otimes |b_1\rangle\langle b_2|\right] := |a_1\rangle\langle a_2| \,\mathrm{Tr}\left[|b_1\rangle\langle b_2|\right] = |a_1\rangle\langle a_2| \,\langle b_2|b_1\rangle \tag{1.40}$$

and by requiring to be linear in its input [6].

It is worth noticing that the reduced density matrix of a pure state can be a mixed state. Take for example the Bell state $|\Phi^+\rangle$, whose density matrix is

$$\hat{\rho}_{|\Phi^+\rangle} := |\Phi^+\rangle\langle\Phi^+| = \frac{|00\rangle\langle 00| + |11\rangle\langle 00| + |00\rangle\langle 11| + |11\rangle\langle 11|}{2} \,. \tag{1.41}$$

Tracing out Bob's qubit, the reduced density matrix of Alice is

$$\hat{\rho}_A = \mathrm{Tr}_B \left[\hat{\rho}_{|\Phi^+\rangle}\right] = \frac{|0\rangle\langle 0| + |1\rangle\langle 1|}{2} = \frac{\mathbb{1}_2}{2} \,. \tag{1.42}$$

Hence, $\hat{\rho}_A$ is not a pure state since $\mathrm{Tr}[\hat{\rho}_A] = 1/2$ which is less than 1. Moreover, $\hat{\rho}_A$ is a *maximally mixed state*, i.e., it describes the mixture given by the two quantum states $|0\rangle$ and $|1\rangle$ which are equally weighted with $p = 1/d$, with $d = 2$ the dimension of the Hilbert space. When the reduced density matrix of an entangled state gives raise to a maximally mixed state, the entangled state is called maximally entangled. All the four Bell states are maximally entangled.

1.2.2 Bell's test of local realistic theories

We will see now a counter-intuitive implication of quantum entanglement, which is related to the investigation of *quantum non-locality* performed in the experiments called "Bell tests". In 1964, John Stewart Bell proved that the predictions of quantum theory are not compatible with those of any realistic physical theory satisfying a *natural* notion of *locality* [7], which, in relativistic terms, means that events in one region of space-time should not influence events in spacelike separated regions [8].

Locality.—In a typical Bell test, two systems, which may have been generated by a common source, are measured by two separated observers, traditionally called Alice and Bob. They can choose to perform several measurements on their own system, and we will denote with x and y the measurement they choose to perform respectively. After the measurement, they yield the outcomes a and b. Alice and Bob repeat the experiment for many runs. Even if they set the same measurement choices x and y, the outcomes a and b may vary from run to run due to the probabilistic nature of the theory, hence their results are governed by a conditional probability distribution $p(a,b|x,y)$.

By repeating the experiment many times and collecting the observed data, Alice and Bob can experimentally estimate such probabilities. In general, Alice and Bob will found that

$$p(a,b|x,y) \neq p(a|x)p(b|y)\,, \tag{1.43}$$

i.e., their outcomes are not statistically independent. This is not strange or unexpected, since, as stressed before, the two systems may have interacted in the past.

The assumption of locality implies that they should be able to identify a set of factors, described by some *local hidden variables* λ, having a joint causal influence on both the outcomes, and which fully account for their interdependence. Hence, the probabilities for a and b should factorize according to

$$p(a,b|x,y,\lambda) = p(a|x,\lambda)p(b|y,\lambda)\,, \tag{1.44}$$

that is: the probability for a depends only on the past variables λ and on the local measurement x, but it does *not* on the distant measurement y and outcome b (and analogously for Bob). It is not necessary for λ to be constant for all runs of the experiment, e.g. λ may involve physical quantities which are not fully controllable. Hence, λ should be characterized by a probability distribution $q(\lambda)$. Combined with (1.44), it is possible to write

$$p(a,b|x,y) = \int_\Lambda d\lambda\; q(\lambda)p(a|x,\lambda)p(b|y,\lambda) \tag{1.45}$$

where we also implicitly assumed that the measurements x and y can be freely chosen in a way that is independent of λ, i.e. $q(\lambda|x,y)=q(\lambda)$. The decomposition in (1.45) represents a precise condition of locality for the Bell tests.

The Bell-CHSH inequality.—We now specialize the description of the Bell test for the case in which Alice and Bob can choose between two measurement choices only $x,y\in\{0,1\}$, and the outcomes a,b are dichotomous variables, i.e. $a,b\in\{-1,+1\}$. The expectation value of the product ab, given the measurement choice (x,y), is

$$\langle a_x b_y\rangle := \sum_{a,b} a\,b\,p(a,b|x,y)\,. \tag{1.46}$$

Then, we can consider the linear combination of the probabilities $p(a,b|x,y)$ defined by the the *S-parameter*,

$$S := \langle a_0 b_0\rangle + \langle a_0 b_1\rangle + \langle a_1 b_0\rangle - \langle a_1 b_1\rangle\,. \tag{1.47}$$

If the locality constraint (1.45) holds, then the S-parameter cannot be greater than 2, i.e.

$$S\leq 2\,, \tag{1.48}$$

which is known as the Clauser-Horne-Shimony-Holt (CHSH) Bell-inequality [9]. In fact, by using (1.45) in the calculation of the S-parameter we have that

$$\langle a_x b_y\rangle = \sum_{a,b}\int_\Lambda d\lambda\, q(\lambda)\, a\,p(a|x,\lambda)\; b\,p(b|y,\lambda) = \int_\Lambda d\lambda\, q(\lambda)\,\langle a_x\rangle_\lambda\langle b_y\rangle_\lambda\,, \tag{1.49}$$

where the expectation values of the local outcomes are $\langle a_x\rangle_\lambda := \sum_a a\,p(a|x,\lambda)$ and $\langle b_y\rangle_\lambda := \sum_b b\,p(b|y,\lambda)$. Thus, inserting (1.49) into the definition (1.47), it is possible to write

$$S = \int_\Lambda d\lambda\, q(\lambda)\, S_\lambda \tag{1.50}$$

with

$$S_\lambda = \langle a_0\rangle_\lambda(\langle b_0\rangle_\lambda + \langle b_1\rangle_\lambda) + \langle a_1\rangle_\lambda(\langle b_0\rangle_\lambda - \langle b_1\rangle_\lambda)\,. \tag{1.51}$$

Since the local expectations $\langle a_x\rangle_\lambda$ and $\langle b_y\rangle_\lambda$ are in the range $[-1,1]$ it follows that S_λ is upper-bounded by 2 and thus (1.48) holds.

Let's now see how Quantum Mechanics allows to violate (1.48). Suppose the Bell state $|\Phi^+\rangle$ is given to Alice and Bob, who choose to measure the local observables $\hat{\mathcal{O}}_{a|x}$ and $\hat{\mathcal{O}}_{b|y}$ defined by

$$\hat{\mathcal{O}}_{a|0} := \hat{\sigma}_3\,,\quad \hat{\mathcal{O}}_{a|1} := \hat{\sigma}_1\,,\quad \hat{\mathcal{O}}_{b|0} := \frac{1}{\sqrt{2}}(\hat{\sigma}_3+\hat{\sigma}_1)\,,\quad \hat{\mathcal{O}}_{b|1} := \frac{1}{\sqrt{2}}(\hat{\sigma}_3-\hat{\sigma}_1)\,. \tag{1.52}$$

According to the quantum mechanical rules presented above, the expectation values are given by

$$\langle a_x b_y \rangle = \langle \Phi^+ | \hat{O}_{a|x} \otimes \hat{O}_{b|y} | \Phi^+ \rangle \ , \tag{1.53}$$

that explicitly yield

$$\langle a_0 b_0 \rangle = \langle a_0 b_1 \rangle = \langle a_1 b_0 \rangle = \frac{1}{\sqrt{2}} \ , \quad \langle a_1 b_1 \rangle = -\frac{1}{\sqrt{2}} \ . \tag{1.54}$$

Hence, the S-parameter, according to the rules of Quantum Mechanics, results equal to $2\sqrt{2} \approx 2.81$, which is notably greater than 2, contrarily to equation (1.48). This fact implies that Quantum Mechanics cannot be explained in terms of local realistic models respecting (1.45), and Bell provided a tool, now experimentally accessible, to test this counter-intuitive character of quantum theory.

We will present a Bell test exploiting time-bin entanglement in Chapter 3.

Chapter 2

Elements of Quantum Optics

Quantum Optics describes the quantum behaviour of electromagnetic waves, i.e., the application of the formalism of Chapter 1 to *light* and its elementary constituents, the *photons*. Since photons are the best candidates for performing quantum experiments in Space along great distances, we will dedicate this chapter to the machinery which allows the description of what happens in a typical Quantum Optics experiment.

The contents of this chapter are a selection of what can be found in standard textbooks on Quantum Optics, as [10, 11, 12, 13]. Reference [14] is a standard textbook on photonics and laser theory.

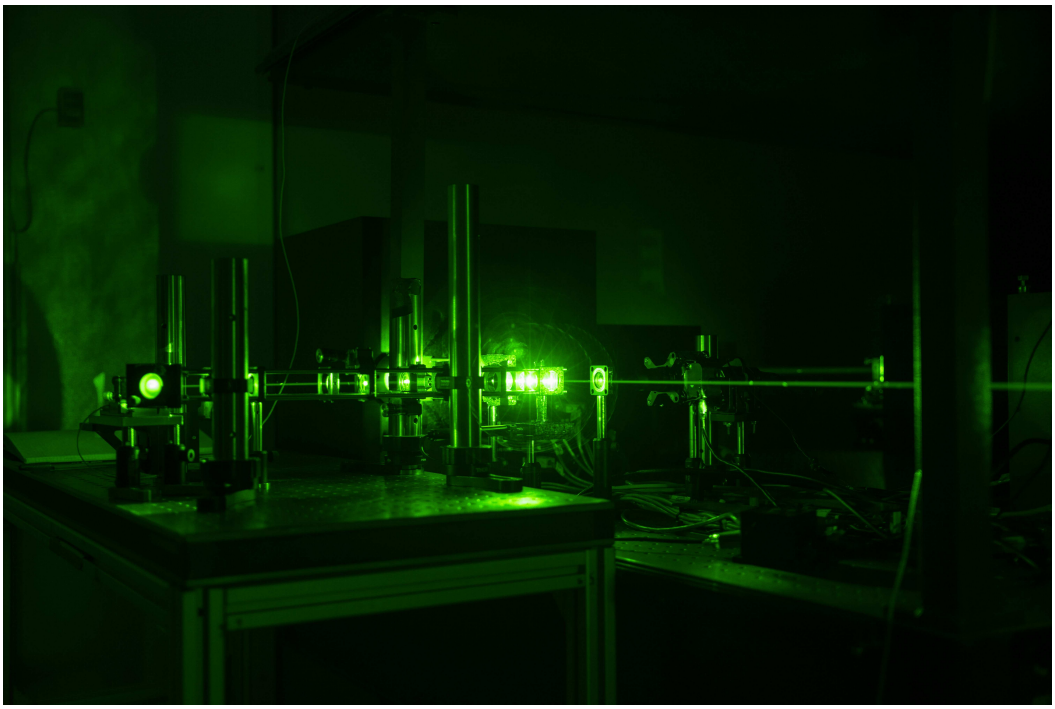

The interferometric quantum optical setup used in Chapter 5 (photo by Paolo Villoresi).

2.1 Quantum description of light

In this section we will see how to apply the formalism of Quantum Mechanics to the electromagnetic field via the *quantization* procedure. Then, we will focus on linear optical devices, the ones typically used in the experiments, and on the mathematical description of the photon's wavepacket.

2.1.1 Quantization of the electromagnetic field

The quantum description of electromagnetic waves is usually presented by using the technique called *second quantization*, through which, starting from the classical solution to the free radiation, i.e. Maxwell's equations with no charges and currents, it is possible to obtain the full quantum description of electromagnetism.

The classical solution for the electric and magnetic fields can be written by expanding the *vector potential* $\mathbf{A}(\mathbf{r},t)$ as a superposition of planewaves in the form

$$\mathbf{A}(\mathbf{r},t)=\sum_{\mathbf{k}}\sum_{\lambda}\mathbf{e}_{\mathbf{k},\lambda}\left[A_{\mathbf{k},\lambda}(t)e^{i\mathbf{k}\cdot\mathbf{r}}+A^{*}_{\mathbf{k},\lambda}(t)e^{-i\mathbf{k}\cdot\mathbf{r}}\right] \tag{2.1}$$

where $A_{\mathbf{k},\lambda}(t)$ is the complex amplitude of the vector field, imagining that free space can be modelled as a cubic cavity of side length L with perfectly reflecting walls, and where $\mathbf{e}_{\mathbf{k},\lambda}$ with $\lambda=1,2$ is a real polarization vector. The sum over

$$\mathbf{k}=\frac{2\pi}{L}(m_x,m_y,m_z) \tag{2.2}$$

with $m_i=0,\pm1,\pm2,\ldots$ simply means that the sum is over the set of integers (m_x,m_y,m_z) specifying the 3-dimensional modes in the cavity and the sum over λ is the sum over the two independent polarizations.

The electromagnetic field is quantized by promoting each possible radiation mode $A_{\mathbf{k},\lambda}$ (and its complex conjugate $A^{*}_{\mathbf{k},\lambda}$) in the cavity to a quantum operator $\hat{a}_{\mathbf{k},\lambda}$ (and its adjoint $\hat{a}^{\dagger}_{\mathbf{k},\lambda}$) and imposing the commutation relations

$$\left[\hat{a}_{\mathbf{k},\lambda},\hat{a}^{\dagger}_{\mathbf{k}',\lambda'}\right]=\delta_{\mathbf{k},\mathbf{k}'}\delta_{\lambda,\lambda'}\,,\quad \left[\hat{a}_{\mathbf{k},\lambda},\hat{a}_{\mathbf{k}',\lambda'}\right]=\left[\hat{a}^{\dagger}_{\mathbf{k},\lambda},\hat{a}^{\dagger}_{\mathbf{k}',\lambda'}\right]=0\,. \tag{2.3}$$

By doing this, the Hamiltonian of the system, that is the observable associated to the energy and also the generator of the time evolution, can be written as

$$\hat{H}=\sum_{\mathbf{k}}\sum_{\lambda}\hbar\omega_k\left(\hat{a}^{\dagger}_{\mathbf{k},\lambda}\hat{a}_{\mathbf{k},\lambda}+\frac{1}{2}\right)=\sum_{\mathbf{k}}\sum_{\lambda}\hbar\omega_k\left(\hat{n}_{\mathbf{k},\lambda}+\frac{1}{2}\right) \tag{2.4}$$

with $\omega_k = |\mathbf{k}|c$ where c is the speed of light in the vacuum, and where we defined the *number operator*

$$\hat{n}_{\mathbf{k},\lambda} := \hat{a}^\dagger_{\mathbf{k},\lambda}\hat{a}_{\mathbf{k},\lambda} \tag{2.5}$$

for the mode labelled by $(\mathbf{k},\lambda)$.

Now, the physical interpretation of the operators introduced is straightforward, since the Hamiltonian is an infinite sequence of harmonic oscillators: $\hat{a}^\dagger_{\mathbf{k},\lambda}$ creates one light quanta, the so-called *photon*, of energy $\hbar\omega_k$ in the mode labelled by $(\mathbf{k},\lambda)$, while $\hat{a}_{\mathbf{k},\lambda}$ destroys it. The number operator has eigenvalues $n_{\mathbf{k},\lambda} = 0,1,2,\ldots,\infty$ and eigenstates $\left|n_{\mathbf{k},\lambda}\right\rangle$ and represents the *number of photons* in that mode.

Let's group the mode labels $(\mathbf{k},\lambda) := j$ to simplify the notation (we will use this simplified notation also in the description of the linear optical devices in Section 2.1.2). The operators introduced above act in the Fock space, i.e. the infinite dimensional Hilbert space of "number representation" where a generic state with n_{j_1} photons in the mode j_1, n_{j_2} photons in the mode j_2 and so on has the form

$$\left|n_{j_1} n_{j_2} \cdots\right\rangle \equiv \left|n_{j_1}\right\rangle \otimes \left|n_{j_2}\right\rangle \otimes \cdots . \tag{2.6}$$

The action of the creation and annihilation operators is

$$\hat{a}^\dagger_j \left|\cdots n_j \cdots\right\rangle = \sqrt{n_j + 1}\left|\cdots n_j + 1 \cdots\right\rangle , \tag{2.7}$$

$$\hat{a}_j \left|\cdots n_j \cdots\right\rangle = \sqrt{n_j}\left|\cdots n_j - 1 \cdots\right\rangle . \tag{2.8}$$

The ground state of the electromagnetic field is the *vacuum state* where there are no photons

$$|\text{vac}\rangle := \left|\{0_j\}\right\rangle = \left|0_{j_1}\right\rangle \otimes \left|0_{j_2}\right\rangle \otimes \cdots . \tag{2.9}$$

Applying each one of the annihilation operators to the vacuum state we obtain

$$\hat{a}_j |\text{vac}\rangle = 0 \tag{2.10}$$

because there are no photons to destroy. We can also generate the quantum state $\left|\{n_j\}\right\rangle$ that has $n = \sum_j n_j$ photons by applying the creation operators $\hat{a}^\dagger_j$ to the vacuum state,

$$\left|\{n_j\}\right\rangle = \prod_j \frac{\left(\hat{a}^\dagger_j\right)^{n_j}}{\sqrt{n_j!}} |\text{vac}\rangle . \tag{2.11}$$

The state vectors $\left|\{n_j\}\right\rangle$ for all values of the integers $\{n_j\}$ form a complete orthonormal set spanning the whole Fock space.

Coherent states.—Another important complete set is given by the *coherent states*, which are the states satisfying

$$\hat{a}\,|\alpha\rangle = \alpha\,|\alpha\rangle \ . \tag{2.12}$$

with $\alpha \in \mathbb{C}$ for each mode j. They are obtained by applying the *displacement operator*, defined by

$$\hat{D}(\gamma) := e^{\gamma\hat{a}^\dagger - \gamma^*\hat{a}} \ , \tag{2.13}$$

to the vacuum state for all the modes. An explicit formula for the coherent state is given by

$$|\alpha\rangle = \hat{D}(\alpha)|\text{vac}\rangle = e^{-\frac{1}{2}|\alpha|^2}\sum_{n=0}^{\infty}\frac{\alpha^n}{\sqrt{n!}}\,|n\rangle \tag{2.14}$$

where we used the state with n photons in the selected mode

$$|n\rangle = \frac{(\hat{a}^\dagger)^n}{\sqrt{n!}}\,|\text{vac}\rangle \ . \tag{2.15}$$

It is worth noticing that the quantum state of the light generated by a laser operating well above its threshold is given, if a reference for the phase is available, by the coherent state$|\alpha\rangle \equiv \left||\alpha|e^{i\theta}\right\rangle$. In this case, the mean number of photons per mode μ is

$$\mu := \langle\hat{n}\rangle = \langle\alpha|\,\hat{n}\,|\alpha\rangle = |\alpha|^2 \ . \tag{2.16}$$

If, on the other hand, the phase reference is not available, the emitted state is described by the mixed state [15]

$$\hat{\rho} = \int_0^{2\pi}\frac{d\theta}{2\pi}\left|\sqrt{\mu}e^{i\theta}\right\rangle\left\langle\sqrt{\mu}e^{i\theta}\right| = \sum_{n=0}^{\infty}p(n|\mu)|n\rangle\langle n| \tag{2.17}$$

where

$$p(n|\mu) = e^{-\mu}\frac{\mu^n}{n!} \tag{2.18}$$

is a Poissonian distribution with mean value μ. Hence, with no reference for the phase, the laser produces a Poissonian mixture of number states.

2.1.2 Quantum description of linear optical devices

In this section we present the description of *linear optics*, i.e. the optical components largely used in quantum optics experiments, following the presentation given in [16].

An optical component is linear if the output fields are linearly related to the input fields. We consider the component like a *multiport* with N input fields and N output fields. In the conventional treatment of linear optical networks the fields are usually assumed to be monochromatic, but in all practical realizations the optical signals have finite duration so a time-domain formulation is necessary and we will present it in the following.

We denote the complex classical fields in the input and output ports with their mode coefficients a_i and b_i respectively ($i = 1,\dots,N$). Input and output modes with the same index may share the same physical port if they propagate in different directions, but they also may share the same physical port if they are separated for example in frequency or polarization. Input and output fields are related by the linear relation

$$b_i = \sum_{j=1}^{N} S_{ij} a_j \tag{2.19}$$

where S_{ij} are the element of a N x N unitary matrix S called *scattering matrix*.

The N input and N output monochromatic fields of the multiport are described quantum mechanically replacing the a_i and b_i fields with the quantum annihilation operators $\hat{a}_i$ and $\hat{b}_i$ respectively. Input operators respect the commutation relations

$$\left[\hat{a}_i, \hat{a}_j^\dagger\right] = \delta_{ij}, \quad \left[\hat{a}_i, \hat{a}_j\right] = 0\,, \tag{2.20}$$

because modes with different index are independent. We have replaced the classical fields with annihilation operators, but the relation between $\hat{b}_i$ and $\hat{a}_i$ still can be written using (2.19) as

$$\hat{b}_i = \sum_{j=1}^{N} S_{ij} \hat{a}_j\,. \tag{2.21}$$

We have also to replace the complex conjugates field a_i^* and b_i^* with creation operators $\hat{a}_i^\dagger$ and $\hat{b}_i^\dagger$ respectively, and, by using the relation between input and output creation operators

$$\hat{b}_i^\dagger = \sum_{j=1}^{N} S_{ij}^* \hat{a}_j^\dagger\,, \tag{2.22}$$

it is possible to demonstrate that output operators satisfy the usual commutation relations

$$\left[\hat{b}_i, \hat{b}_j^\dagger\right] = \left[\sum_{k=1}^{N} S_{ik}\hat{a}_k, \sum_{l=1}^{N} S_{jl}^* \hat{a}_l^\dagger\right] = \sum_{k,l=1}^{N} S_{ik} S_{jl}^* \left[\hat{a}_k, \hat{a}_l^\dagger\right] = \sum_{k,l=1}^{N} S_{ik} S_{jl}^* \delta_{kl} = \delta_{ij} \tag{2.23}$$

where in the last passage we used also the fact that the scattering matrix is unitary.

The scattering matrix describes the evolution of the mode operators, hence we are presenting the evolution of the system in the *Heisenberg picture*, where the vector states remain constant and the operators evolve [2].

To calculate the detection probabilities at the output port for the Quantum Optics experiment we will present in the following, it is useful to express the constant state of the system $|\Psi\rangle$ by using both the input operators or the output ones. We have, from equation (2.22), that

$$\hat{a}_i^\dagger = \sum_{j=1}^{N} \hat{b}_j^\dagger S_{ji} \ . \tag{2.24}$$

Hence, the constant state $|\Psi\rangle$ of the system will be some function $\mathscr{F}$ of the input operators, but it can be written also as a function $\mathscr{F}'$ of the output operators according to (2.24), that is:

$$|\Psi\rangle = \mathscr{F}(\{\hat{a}_i^\dagger\})|\text{vac}\rangle = \mathscr{F}\left(\left\{\sum_{j=1}^{N} \hat{b}_j^\dagger S_{ji}\right\}\right)|\text{vac}\rangle = \mathscr{F}'(\{\hat{b}_i^\dagger\})|\text{vac}\rangle \ , \tag{2.25}$$

where $|\text{vac}\rangle$ is the vacuum state of the linear multiport.

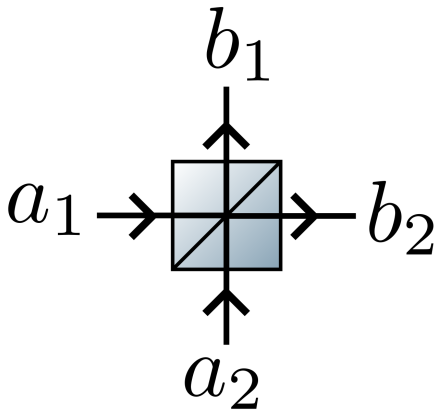

Figure 2.1: Input-output modes representation of a beam splitter (BS).

The beam-splitter.—Let's consider now an example: the *50:50 beam splitter* (BS) of Figure 2.1. The beam splitter is a optical component that has two input ports and two output ports so its scattering matrix is a 2 x 2 matrix. Physically, it is a semireflecting mirror with equal transmission and reflection coefficients. The phase shift between the reflected and transmitted fields depend on the construction of the beam splitter and if it is constructed as a single dielectric layer, the reflected and transmitted beams will differ in phase by a factor of $e^{i\pi/2} = i$. Assuming that the reflected field suffers a $\pi/2$ phase shift, the input $\hat{a}_i$ and output $\hat{b}_i$ modes are related according to the matrix

$$S_{BS} = \frac{1}{\sqrt{2}} \begin{pmatrix} i & 1 \\ 1 & i \end{pmatrix} . \tag{2.26}$$

We can think to a single-photon input state impinging at port a_1 of the 50:50 beam splitter of Figure 2.1. The state of the system is transformed according to

$$|1\rangle_{a_1}|0\rangle_{a_2} = \hat{a}_1^\dagger|\text{vac}\rangle \xrightarrow{(2.25)} \frac{1}{\sqrt{2}}\left(i\hat{b}_1^\dagger + \hat{b}_2^\dagger\right)|\text{vac}\rangle = \frac{1}{\sqrt{2}}\left(i|1\rangle_{b_1}|0\rangle_{b_2} + |0\rangle_{b_1}|1\rangle_{b_2}\right), \quad (2.27)$$

which is notably entangled in the two output modes. Thus, we can detect the single input photon in each of the two output ports b_1 and b_2 with equal probability 1/2.

The balanced Mach-Zehnder interferometer.—It is worth noticing that a cascade of M multiports whose scattering matrix are $S_1, S_2 \dots S_M$ is equivalent to a single multiport of scattering matrix $S = S_M \cdots S_2 S_1$. This tool allows to treat, for example, the *balanced Mach-Zehnder interferometer* of Figure 2.2. This interferometer is composed by two 50:50 beam

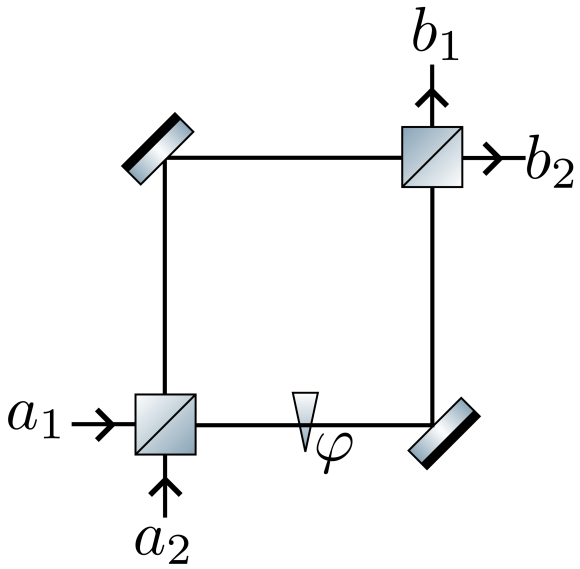

Figure 2.2: The balanced Mach-Zehnder interferometer.

splitters and a phase shift in one of the arms. The scattering matrix for this optical system is given by

$$S = S_{BS}\begin{pmatrix} 1 & 0 \\ 0 & e^{i\varphi} \end{pmatrix} S_{BS} = \frac{1}{2}\begin{pmatrix} e^{i\varphi}-1 & i(1+e^{i\varphi}) \\ i(1+e^{i\varphi}) & 1-e^{i\varphi} \end{pmatrix}. \quad (2.28)$$

Now, given the input state $|\Psi\rangle = \hat{a}_1^\dagger|\text{vac}\rangle$ as before, it becomes, in terms of the output operator,

$$\begin{aligned} |\Psi\rangle &= \left[\frac{e^{i\varphi}-1}{2}\hat{b}_1^\dagger + \frac{i(e^{i\varphi}+1)}{2}\hat{b}_2^\dagger\right]|\text{vac}\rangle \\ &= \frac{e^{i\varphi}-1}{2}|1\rangle_{b_1}|0\rangle_{b_2} + \frac{i(e^{i\varphi}+1)}{2}|0\rangle_{b_1}|1\rangle_{b_2}. \end{aligned} \quad (2.29)$$

In this case, the probability to get the photon at the output ports b_1 and b_2 are

$$p(b_1) = \left|\frac{e^{i\varphi}-1}{2}\right|^2 = \sin^2\frac{\varphi}{2}\,, \quad p(b_2) = \left|\frac{i(e^{i\varphi}+1)}{2}\right|^2 = \cos^2\frac{\varphi}{2}\,. \tag{2.30}$$

If the phase shift φ between the two arms of the interferometer is zero, the input photon can be detected only at port b_2. This is an quantum mechanical interference phenomena realized with single photons. In fact, to arrive at one of the two detectors placed in b_1 or b_2 the photon can take one on the two paths given by each of the two arms of the interferometer. We cannot say which of the possible paths the photon actually takes and so the two quantum amplitude related to the two different path have a well-defined phase relationship and interfere.

2.1.3 Quantum wavepacket for the photon

In Section 2.1.1 we described the quantization of electromagnetic field by modelling the free space as a cavity. This led to the fact that the modes of the electromagnetic field are described by a discrete wavevector $\mathbf{k}$ and the polarization. However, real experiments use light beams travelling in straight lines from the source to the detectors in regions that cannot be contained in a optical cavity. Hence, it is necessary, for some experiment as the one on single-photon interference along space channels in Chapter 5 to describe moving photons as localized pulse travelling along a straight line. We will follow the description given in [10].

A *pulse*, such the one produced by a mode-locking laser [14], necessarily contains a continuous band of frequency ω around a central frequency ω_0, since it has a finite duration. We assume the pulse propagates along the direction given by the z-axis. We have to take the limit of a L-long quantization-axis extending in parallel to the propagation axis, whose one-dimensional mode spacing is

$$\Delta\omega = \frac{2\pi c}{L} \tag{2.31}$$

which tends to zero when L goes to infinity. Thus, the summation over the wavenumber $k = \omega_k/c$ are replaced by integral of the form

$$\sum_k \to \int dk\,\frac{L}{2\pi} = \int d\omega_k\,\frac{L}{2\pi c} = \frac{1}{\Delta\omega}\int d\omega, \tag{2.32}$$

and the discrete and continuous delta functions are related by

$$\delta_{k,k'} \to \Delta\omega\,\delta(\omega-\omega_0)\,. \tag{2.33}$$

Then, the discrete creation and annihilation operators $\hat{a}_k^\dagger$,$\hat{a}_k$ are replaced by their continuous-mode counterparts

$$\hat{a}_k \to \sqrt{\Delta\omega}\,\hat{a}(\omega), \quad \hat{a}_k^\dagger \to \sqrt{\Delta\omega}\,\hat{a}^\dagger(\omega) \tag{2.34}$$

in order to satisfy the commutation relation

$$\left[\hat{a}(\omega),\hat{a}^\dagger(\omega')\right] = \delta(\omega-\omega')\,. \tag{2.35}$$

It is useful to define the Fourier transformed operators in the time domain according to

$$\hat{a}(t) := \frac{1}{\sqrt{2\pi}}\int d\omega\;\hat{a}(\omega)\,e^{-i\omega t}\,, \tag{2.36}$$

that lead to the relation

$$\left[\hat{a}(t),\hat{a}^\dagger(t')\right] = \delta(t-t')\,. \tag{2.37}$$

The inverse Fourier transformation is

$$\hat{a}(\omega) := \frac{1}{\sqrt{2\pi}}\int dt\;\hat{a}(t)\,e^{+i\omega t} \tag{2.38}$$

while the analogue of the number operators is given by

$$\hat{n} := \int d\omega\;\hat{a}^\dagger(\omega)\,\hat{a}(\omega) \equiv \int dt\;\hat{a}^\dagger(t)\,\hat{a}(t) \tag{2.39}$$

As usual, the continuous-mode vacuum state satisfies

$$\hat{a}(\omega) = \hat{a}(t)\,|\mathrm{vac}\rangle = 0\,, \tag{2.40}$$

while

$$|\omega\rangle = \hat{a}^\dagger(\omega)\,|\mathrm{vac}\rangle\;, \quad |t\rangle = \hat{a}^\dagger(t)\,|\mathrm{vac}\rangle\;. \tag{2.41}$$

However, these states are still not a realistic representation of the photon-number states generated in the experiments. The latter are best described by *wavepacket* covering a continuous range of frequencies, as in the case of pulses.

We will describe Gaussian pulses, whose spectral amplitude is represented by the function

$$\xi_{t_0}(\omega) := \left(2\pi\Delta^2\right)^{1/4} e^{-i(\omega_0-\omega)t_0} e^{-\frac{(\omega_0-\omega)^2}{4\Delta^2}}\,, \tag{2.42}$$

where ω_0 is the central frequency of the pulse spectrum, t_0 is the time at which the peak of the pulse passes the coordinate origin $z = 0$, and Δ is the bandwidth of the spectrum, assumed to be $\Delta \ll \omega_0$. The relation between the bandwidth Δ and the *coherence time* τ_c of the pulse is

$$\tau_c := \frac{\sqrt{\pi}}{\Delta}\,. \tag{2.43}$$

By using the same convention on the Fourier transformation of the continuous-mode filed operators in (2.36) and (2.41) the wavepacket amplitude in the time domain can be written as

$$\xi_{t_0}(t) = \left(\frac{2\Delta^2}{\pi}\right)^{1/4} e^{-i\omega_0 t} e^{-\Delta^2(t-t_0)^2} = \left(\frac{2}{\tau_c^2}\right)^{1/4} e^{-i\omega_0 t} e^{-\pi\frac{(t-t_0)^2}{\tau_c^2}} . \tag{2.44}$$

It is worth noticing that the wavepacket is normalized

$$\int d\omega |\xi_{t_0}(\omega)|^2 = \int dt |\xi_{t_0}(t)|^2 = 1 . \tag{2.45}$$

Hence, a photon described by the wavepacket (2.42) or, equivalently, by (2.44) is created by the *photon-wavepacket creation operator*

$$\hat{a}^\dagger_{\xi_{t_0}} := \int d\omega\ \xi_{t_0}(\omega)\, \hat{a}^\dagger(\omega) = \int dt\ \xi_{t_0}(t)\, \hat{a}^\dagger(t) \tag{2.46}$$

and it is represented by the state

$$\left|1_{\xi_{t_0}}\right\rangle := \hat{a}^\dagger_{\xi_{t_0}} |\text{vac}\rangle . \tag{2.47}$$

The probability of getting a photon in a time interval large $2\Delta w$ around t_0, if the state is $\left|1_{\xi_{t_0}}\right\rangle$, is given by

$$p([t_0-\Delta w, t_0+\Delta w]) = \left\langle 1_{\xi_{t_0}}\right| \left[\int_{t_0-\Delta w}^{t_0+\Delta w} dt \hat{a}^\dagger(t)\hat{a}(t)\right] \left|1_{\xi_{t_0}}\right\rangle = \int_{t_0-\Delta w}^{t_0+\Delta w} dt |\xi_{t_0}(t)|^2 , \tag{2.48}$$

that is analogue to Born's rule if we replace the wavefunction of a unidimensional quantum particle in the x-representation $\psi(x) = \langle x|\psi\rangle$ with the photon wavepacket $\xi_{t_0}(t)$ [2].

It is worth noticing that two pulses separated by more than the coherence time τ_c can be considered independent one from each other. More precisely, the commutation relations for the operators in (2.46) are

$$\left[\hat{a}_{\xi_{t_0}}, \hat{a}^\dagger_{\xi_{t_0+\Delta t}}\right] = e^{-\frac{1}{2}\left(\frac{\Delta t}{\tau_c}\right)^2} \tag{2.49}$$

ans so, if $\Delta t \gg \tau_c$, two Gaussian pulses in the same mode can be treated as orthogonal,

$$\left\langle 1_{\xi_{t_0+\Delta t}}\right| \left|1_{\xi_{t_0}}\right\rangle = \langle \text{vac}| \hat{a}_{\xi_{t_0+\Delta t}} \hat{a}^\dagger_{\xi_{t_0}} |\text{vac}\rangle = \langle \text{vac}| \left[\hat{a}_{\xi_{t_0}}, \hat{a}^\dagger_{\xi_{t_0+\Delta t}}\right] |\text{vac}\rangle = e^{-\frac{1}{2}\left(\frac{\Delta t}{\tau_c}\right)^2} \xrightarrow{\Delta t \gg \tau_c} 0 . \tag{2.50}$$

Moreover, continuous-mode field operators can be used in the linear multiport of Section 2.1.2 simply asking that two different inputs modes respect

$$\left[\hat{a}_i(\omega), \hat{a}^\dagger_j(\omega')\right] = \delta_{ij}\delta(\omega-\omega') . \tag{2.51}$$

Then, generalizing equation (2.24), we have

$$\hat{a}^\dagger_{i,\xi_{t_0}} = \sum_{j=1}^{N} \int d\omega\ \xi_{t_0}(\omega) S_{ji}(\omega) \hat{b}^\dagger_j(\omega) , \tag{2.52}$$

which will be used for the time-bin encoding in Section 2.2.3.

2.2 Encoding quantum information into photons

In this section we will see why the *laser* is the master tool implemented in Quantum Optics experiment. We will see when a weak-coherent laser is a good approximation of a single photon source, and then we will investigate the two main encodings used in photonic implementations of Quantum Information, that are, polarization and time-bin. The goal of this section is to render the connection between what happens in the lab and what the abstract quantum theory predicts as close as possible.

2.2.1 Weak-coherent states for Quantum Optics experiments

We have seen in Section 2.1.1 that a laser operating well above its threshold outputs the mixed state given by (2.17) and we saw that the probability of finding n photon in a pulse or a time interval, given the mean number $\mu = |\alpha|^2$, is described by the Poissonian distribution in (2.18). In the following, we will deal with laser pulses in which the probability of finding two photons in a pulse, or in a time interval, becomes negligible. These attenuated laser pulses are called *weak-coherent* (WC). We will see now when it is possible to use weak coherent light as an approximation for single-photon states, which are experimentally much more difficult to generate. A good reference for this section is the book in [13].

By assuming a small mean photon number $\mu \ll 1$, it is possible to expand the mixture (2.17) as

$$\begin{aligned}\hat{\rho}_{\mathrm{WC}} &= \sum_{n=0}^{\infty} p(n|\mu \ll 1)\,|n\rangle\langle n| \\ &\approx \left(1-\mu+\frac{\mu^2}{2}+\mathcal{O}(\mu^3)\right)\left[|0\rangle\langle 0|+\mu\,|1\rangle\langle 1|+\frac{\mu^2}{2}+\mathcal{O}(\mu^3)\right] \\ &\approx \left(1-\mu+\frac{\mu^2}{2}\right)|0\rangle\langle 0|+(\mu-\mu^2)\,|1\rangle\langle 1|+\frac{\mu^2}{2}\,|2\rangle\langle 2|+\mathcal{O}(\mu^3)\,. \end{aligned} \tag{2.53}$$

Such expansion shows the probability of finding one photon in a pulse is of the order μ, while the two-photon contribuiton appears with probability $\mu^2/2$.

When only *one* weak coherent beam is used, for example in a interferometry experiment, the pulses containing one or more photons can trigger a detection. In this case, the rate of one photon generation is small, proportional to μ, but the two-photon contribution is even smaller, going as $\mu^2/2$. Thus, the *post-selection* on the actual detections in this case is a valid procedure, and visibilities arbitrarily close to one can be achieved.

On the other hand, such post-selection can fail when *two* or more weak coherent sources are used in a interferometry experiment where two photons are typically detected

in each run or within a fixed *coincidence* window. In this case, the two photons may have come from the one-photon contribution in both the beams with probability μ^2, which is of the same order of magnitude of the probability $\mu^2/2$ that the two photons actually came from only one of the two beams. When it is not possible to discriminate between these two possibilities, the post-selection procedure is not valid and the single-photon approximation is not applicable.

In the following we will use weak coherent pulses imping onto linear optical devices. To understand the evolution of the system is it useful to describe what happens to a coherent state $|\alpha\rangle$ entering the port a_1 of the beam splitter of Figure 2.1. It is worth noticing that the displacement operator can be written as [12]

$$\hat{D}_a(\gamma) = e^{\gamma\hat{a}^\dagger - \gamma^*\hat{a}} = e^{-|\gamma|^2/2} e^{\gamma\hat{a}^\dagger} e^{-\gamma^*\hat{a}} \tag{2.54}$$

and thus

$$|\alpha\rangle_{a_1} = e^{-|\alpha|^2/2} e^{\alpha\hat{a}_1^\dagger} e^{-\alpha^*\hat{a}_1} |\text{vac}\rangle = e^{-|\alpha|^2/2} e^{\alpha\hat{a}_1^\dagger} |\text{vac}\rangle \ . \tag{2.55}$$

By using the mode transformation of the beam splitter in (2.27)

$$\hat{a}_1^\dagger \to \frac{1}{\sqrt{2}} \left(i\hat{b}_1^\dagger + \hat{b}_2^\dagger \right) , \tag{2.56}$$

the output state is

$$\begin{aligned}
|\alpha\rangle_{a_1} &\to e^{-|\alpha|^2/2} e^{\alpha \frac{1}{\sqrt{2}} \left(i\hat{b}_1^\dagger + \hat{b}_2^\dagger \right)} |\text{vac}\rangle \\
&= e^{-|\alpha|^2/2} \, e^{\frac{\alpha i \hat{b}_1^\dagger}{\sqrt{2}} + \frac{\alpha \hat{b}_2^\dagger}{\sqrt{2}}} |\text{vac}\rangle \\
&= e^{-|\alpha|^2/2} \, e^{\frac{\alpha i \hat{b}_1^\dagger}{\sqrt{2}}} |0\rangle_{b_1} \otimes e^{\frac{\alpha \hat{b}_2^\dagger}{\sqrt{2}}} |0\rangle_{b_2} \\
&= e^{-|\alpha|^2/4} \sum_{n=0}^{+\infty} \frac{(i\alpha/\sqrt{2})^n}{\sqrt{n!}} |n\rangle_{b_1} \otimes e^{-|\alpha|^2/4} \sum_{l=0}^{+\infty} \frac{(\alpha/\sqrt{2})^l}{\sqrt{l!}} |l\rangle_{b_2} \\
&= \left| \frac{i\alpha}{\sqrt{2}} \right\rangle_{b_1} \otimes \left| \frac{\alpha}{\sqrt{2}} \right\rangle_{b_2}
\end{aligned} \tag{2.57}$$

where we noted that that for $\gamma \in \mathbb{C}$

$$\left| \frac{\gamma}{\sqrt{2}} \right\rangle = e^{-|\gamma|^2/4} \sum_{n=0}^{+\infty} \frac{(\gamma/\sqrt{2})^n}{\sqrt{n!}} |n\rangle \ . \tag{2.58}$$

This is the result expected for a classical light wave, since the impinging intensity is divided between the two output beams, e.g. half the incident average photon number, $|\alpha|^2/2$, emerges in each beam. The output state is *separable* in the two output modes, since it is given by the tensor product of two coherent beams. There are no quantum optical

linear operations that can transform a classical-like state as the product of two coherent states in a non-classical state like the one in (2.27), which is entangled. Indeed, usually optical non-linearities are used to achieve this goal, as in the SPDC process described in Section 2.3.1.

However, to which extend the product of two weak-coherent beams in two different modes can be a good approximation for a single photon in a superposition of two modes, that is, a qubit? Let's take the coherent state in two modes A and B given by

$$|\Psi\rangle = |\alpha\rangle_A |\alpha\rangle_B \ . \tag{2.59}$$

By expanding $|\alpha\rangle$ as

$$|\alpha\rangle \approx e^{-\frac{|\alpha|^2}{2}} \left[|0\rangle + \alpha |1\rangle + \frac{\alpha^2}{\sqrt{2}} |2\rangle + \mathcal{O}(\alpha^3) \right] , \tag{2.60}$$

we obtain, up to $\mathcal{O}(\alpha^3)$, the expansion:

$$\begin{aligned} |\Psi\rangle \approx & \left(1 - |\alpha|^2\right) |0\rangle_A |0\rangle_B \\ & + \alpha \left(|1\rangle_A |0\rangle_B + |0\rangle_A |1\rangle_B \right) \\ & + \alpha^2 |1\rangle_A |1\rangle_B + \frac{\alpha^2}{\sqrt{2}} \left(|2\rangle_A |0\rangle_B + |0\rangle_A |2\rangle_B \right) \ . \end{aligned} \tag{2.61}$$

As discussed before, the single-photon contribution may trigger a detection with probability $\mu = |\alpha|^2$, while for the two-photon contribution the same probability is only of the order $\sim \mu^2 = |\alpha|^4$. Hence, a *post-selected* weak coherent state in two different modes provides a good approximation for a single-photon in a two-mode qubit-superposition, since the (renormalized) one-photon part of the state is dominant with respect to the two-photon one. The renormalized 1-photon part of the state $|\Psi\rangle$ is given by

$$|\Psi_1\rangle \approx \frac{1}{\sqrt{2}} \left(|1\rangle_A |0\rangle_B + |0\rangle_A |1\rangle_B \right) \ . \tag{2.62}$$

It is worth noticing that the above approximation is valid only if we are interested in using post-selected weak-coherent state for experiments based on the first degree of coherence [12], as the ones presented in the following.

2.2.2 Polarization encoding and Jones calculus

A natural degree of freedom to encoding quantum information into photons is given by *polarization*. The electromagnetic field is specified by a polarization vector $\mathbf{e}_{\mathbf{k},\lambda}$ laying in a plane orthogonal to the direction axis. We will assume that the $X - Y$ axes of this

plane are aligned with the horizontal and vertical directions, respectively. Hence, a linearly polarized single photon state in the horizontal or vertical directions will be indicated with

$$|H\rangle \equiv \begin{pmatrix} 1 \\ 0 \end{pmatrix}, \quad |V\rangle \equiv \begin{pmatrix} 0 \\ 1 \end{pmatrix}, \tag{2.63}$$

which correspond to the $|0\rangle$ and $|1\rangle$ states of the computational basis respectively. A general polarization-based qubit in a pure state will be described by

$$|\psi\rangle = \cos\left(\frac{\theta}{2}\right)|H\rangle + e^{i\varphi}\sin\left(\frac{\theta}{2}\right)|V\rangle \equiv \begin{pmatrix} \cos\frac{\theta}{2} \\ e^{i\varphi}\sin\frac{\theta}{2} \end{pmatrix}, \tag{2.64}$$

lying on the surface of the so-called Bloch, or Poincaré, sphere, as shown in Figure 2.3. The commonly used states in quantum optics implementations of quantum information protocols are defined by

$$|D\rangle := \frac{1}{\sqrt{2}}(|H\rangle + |V\rangle) \tag{2.65}$$

$$|A\rangle := \frac{1}{\sqrt{2}}(|H\rangle - |V\rangle) \tag{2.66}$$

$$|R\rangle := \frac{1}{\sqrt{2}}(|H\rangle + i\,|V\rangle) \tag{2.67}$$

$$|L\rangle := \frac{1}{\sqrt{2}}(|H\rangle - i\,|V\rangle) \tag{2.68}$$

where $|D\rangle$ ($|A\rangle$) represents a photon linearly polarized at $+45°$ ($-45°$) with respect to the horizontal direction, diagonally and anti-diagonally respectively, while $|R\rangle$ ($|L\rangle$) represents a right (left) circularly polarized photon.

It is useful to relate the component of the Bloch vector of a generic polarization-based encoded qubit to projective measurements onto the states defined above. Indeed, by observing that the Pauli matrices can be re-written as

$$\hat{\sigma}_0 = \mathbb{1}_2 \equiv \hat{P}_{|H\rangle} + \hat{P}_{|V\rangle} = |H\rangle\langle H| + |V\rangle\langle V|\,, \tag{2.69}$$

$$\hat{\sigma}_1 \equiv \hat{P}_{|D\rangle} - \hat{P}_{|A\rangle} = |D\rangle\langle D| - |A\rangle\langle A|\,, \tag{2.70}$$

$$\hat{\sigma}_2 \equiv \hat{P}_{|R\rangle} - \hat{P}_{|L\rangle} = |R\rangle\langle R| - |L\rangle\langle L|\,, \tag{2.71}$$

$$\hat{\sigma}_3 \equiv \hat{P}_{|H\rangle} - \hat{P}_{|V\rangle} = |H\rangle\langle H| - |V\rangle\langle V|\,, \tag{2.72}$$

we have that the Stokes parameters for the general mixed state $\hat{\rho}$ defined in (1.28) are given

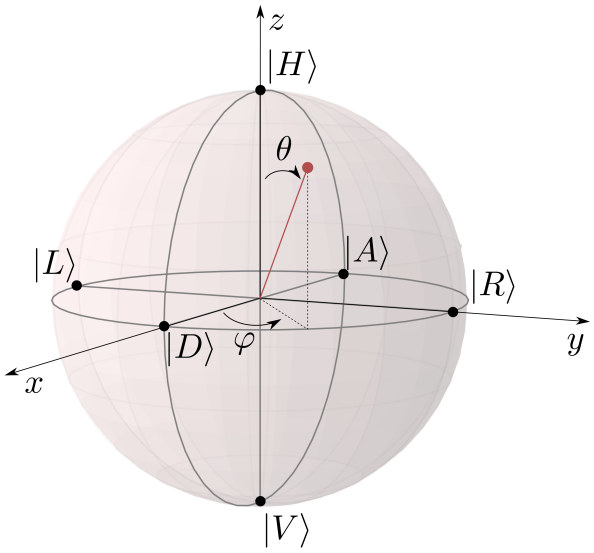

Figure 2.3: *Bloch sphere representation of a polarization encoded qubit* $|\psi\rangle = \cos(\theta/2)|H\rangle + e^{i\varphi}\sin(\theta/2)|V\rangle$.

by the expectation values

$$S_0 = \langle \hat{P}_{|H\rangle} + \hat{P}_{|V\rangle} \rangle_\rho \,, \tag{2.73}$$

$$S_1 \equiv r_1 = \langle \hat{P}_{|D\rangle} - \hat{P}_{|A\rangle} \rangle_\rho \,, \tag{2.74}$$

$$S_2 \equiv r_2 = \langle \hat{P}_{|R\rangle} - \hat{P}_{|L\rangle} \rangle_\rho \,, \tag{2.75}$$

$$S_3 \equiv r_3 = \langle \hat{P}_{|H\rangle} - \hat{P}_{|V\rangle} \rangle_\rho \,. \tag{2.76}$$

To implement such projective measurements it is sufficient to use a quarter-waveplate followed by a half-waveplate then followed by a polarizing beam splitter, as described in the following.

Jones calculus.—In polarization-based quantum optics experiments linear optical devices transforming polarization without (ideally) introducing losses are commonly used, as polarizing beam splitter, half-wave and quarter-wave retarders, polarizers and so on. Each of these devices can be described as a linear multiport, with the modes labelled by the polarizations H and V. In this case, the scattering matrix or *Jones matrix* S^J is a 2×2 acting as

$$\begin{pmatrix} \hat{b}_H \\ \hat{b}_V \end{pmatrix} = S^J \begin{pmatrix} \hat{a}_H \\ \hat{a}_V \end{pmatrix} , \tag{2.77}$$

and for the creation operators we have that $\hat{a}_H^\dagger|\text{vac}\rangle \equiv \hat{b}_H^\dagger|\text{vac}\rangle \equiv |H\rangle$ and $\hat{a}_V^\dagger|\text{vac}\rangle \equiv \hat{b}_V^\dagger|\text{vac}\rangle \equiv |V\rangle$. Hence, the mode transformation is given by

$$\hat{a}_H^\dagger \to S^J_{11}\hat{b}_H^\dagger + S^J_{21}\hat{b}_V^\dagger \,, \quad \hat{a}_V^\dagger \to S^J_{12}\hat{b}_H^\dagger + S^J_{22}\hat{b}_V^\dagger \,, \tag{2.78}$$

according to (2.24). Actually, the description via the mode transformation in (2.78) is equivalent to the *Jones calculus* [14]. Indeed, Jones calculus provides that the general polarized state in the vector representation

$$|\psi\rangle = \alpha\,|H\rangle + \beta\,|V\rangle \equiv \begin{pmatrix} \alpha \\ \beta \end{pmatrix}, \tag{2.79}$$

is transformed into the state $|\psi'\rangle$ according to

$$|\psi'\rangle := \alpha'\,|H\rangle + \beta'\,|V\rangle \equiv \begin{pmatrix} \alpha' \\ \beta' \end{pmatrix} = S^J\,|\psi\rangle = S^J \begin{pmatrix} \alpha \\ \beta \end{pmatrix}. \tag{2.80}$$

Hence, we have that

$$\alpha' = S^J_{11}\alpha + S^J_{12}\beta, \quad \beta' = S^J_{21}\alpha + S^J_{22}\beta\,, \tag{2.81}$$

which is equivalent to the mode transformation given in (2.78). In the Jones representation, the scattering matrix S^J is the unitary matrix giving the evolution of the quantum state passing through the optical device described by S^J. We now present some examples of common optical devices used in the experiments explained in the following chapters.

Wave-retarders.—Wave-plates o wave-retarders are optical devices made of a birefringent material, characterized by a different refractive index for two orthogonal axes. The material used in most wave-plates is quartz, which is a positive uniaxial crystal with $n_e - n_o := \delta_n > 0$ [14]. The axis characterized by the lower refraction index is called the *fast* optical axis while the other is called *slow*, since $v = c/n$ is the propagation velocity of light into the material. Hence, $n_{\text{fast}} = n_o$ and $n_{\text{slow}} = n_e$ and $\delta_n = n_{\text{slow}} - n_{\text{fast}}$, assuming the fast optical axis aligned along the horizontal direction, a wave retarder can be modelled by the Jones matrix

$$S^\Gamma = e^{i\frac{2\pi}{\lambda}d\,n_{\text{fast}}} \begin{pmatrix} 1 & 0 \\ 0 & e^{i\frac{2\pi}{\lambda}d\,\delta_n} \end{pmatrix} \equiv \begin{pmatrix} 1 & 0 \\ 0 & e^{i\Gamma} \end{pmatrix}. \tag{2.82}$$

where λ is the wavelength of the photon, d is the thickness of the ratarder and $\Gamma = \frac{2\pi}{\lambda}d\,\delta_n$ is the retardance introduced by the waveplate. Two examples of wave retarders commonly implemented in quantum optics experiments are the *half-waveplate* (HWP, or $\lambda/2$) with $d\,\delta_n = \lambda/2$ and so $\Gamma = \pi$ and the *quarter-waveplate* (QWP, or $\lambda/4$) with $d\,\delta_n = \lambda/4$ and so $\Gamma = \pi/2$, characterized by

$$S^{\text{HWP}} = \begin{pmatrix} 1 & 0 \\ 0 & -1 \end{pmatrix} \equiv \hat{\sigma}_z \equiv e^{-i\frac{\pi}{2}\hat{\sigma}_z} \equiv \hat{R}_z(\pi)\,, \tag{2.83}$$

$$S^{\text{QWP}} = \begin{pmatrix} 1 & 0 \\ 0 & i \end{pmatrix} \equiv e^{-i\frac{\pi}{4}\hat{\sigma}_z} \equiv \hat{R}_z(\pi/2)\,. \tag{2.84}$$

However, typically these devices are placed with their fast optical axis making an angle ϕ with the horizontal polarization, assumed to be aligned with the X-axis in the polarization plane. Hence, the new reference frame in the $X-Y$ plane is rotated by the rotation matrix $\mathscr{R}(\phi)$

$$\mathscr{R}(\phi)=\begin{pmatrix}\cos\phi & -\sin\phi\\ \sin\phi & \cos\phi\end{pmatrix}\equiv\hat{R}_y(2\phi)\,, \tag{2.85}$$

which has the same form of the exponentiation of a $\hat{\sigma}_y$ matrix, and so the rotated version of the Jones matrix S^J is

$$S^J_\phi := \mathscr{R}(\phi)S^J\mathscr{R}(-\phi)\equiv\hat{R}_y(2\phi)S^J\hat{R}_y(-2\phi)\ . \tag{2.86}$$

As an example, the wave retarders presented above, when rotated by an angle ϕ with respect to the horizontal axes, are given by

$$S^\Gamma_\phi=\begin{pmatrix}\cos^2\phi+\sin^2\phi e^{i\Gamma} & \cos\phi\sin\phi(1-e^{i\Gamma})\\ \cos\phi\sin\phi(1-e^{i\Gamma}) & \sin^2\phi+\cos^2\phi e^{i\Gamma}\end{pmatrix}, \tag{2.87}$$

$$S^{\mathrm{HWP}}_\phi=\left[\hat{R}_y(2\phi)\right]^2\hat{\sigma}_z\equiv\hat{R}_y(4\phi)\hat{\sigma}_z=\begin{pmatrix}\cos 2\phi & \sin 2\phi\\ \sin 2\phi & -\cos 2\phi\end{pmatrix}\equiv\hat{R}_y(4\phi)\hat{R}_z(\pi)\,, \tag{2.88}$$

$$S^{\mathrm{QWP}}_\phi=\begin{pmatrix}\cos^2\phi+i\sin^2\phi & \cos\phi\sin\phi(1-i)\\ \cos\phi\sin\phi(1-i) & \sin^2\phi+i\cos^2\phi\end{pmatrix}\equiv\hat{R}_z(\pi/2)\hat{R}_x(2\phi)\hat{R}_y(-2\phi)\,, \tag{2.89}$$

where we used the general properties of the rotation operators

$$\hat{R}_y(\phi)\hat{\sigma}_z=\hat{\sigma}_z\hat{R}_y(-\phi)\,, \tag{2.90}$$

$$\hat{R}_i(\alpha+\beta)=\hat{R}_i(\alpha)\hat{R}_i(\beta)\,, \tag{2.91}$$

$$\hat{R}_z(-\pi/2)\hat{R}_y(\alpha)\hat{R}_z(\pi/2)=\hat{R}_x(\alpha) \tag{2.92}$$

and the fact that the Jones matrices are equivalent ("$\equiv$") up to a global phase factor. It is easy to show that:

$$S^{\mathrm{HWP}}_{\phi+\pi/2}=\left(S^{\mathrm{HWP}}_\phi\right)^\dagger=S^{\mathrm{HWP}}_\phi\,, \tag{2.93}$$

$$S^{\mathrm{QWP}}_{\phi+\pi/2}=\left(S^{\mathrm{QWP}}_\phi\right)^\dagger\,. \tag{2.94}$$

In particular, the inverse of a QWP rotated by ϕ is a QWP with orthogonal fast optical axis.

The transformation written above are cast in a way which allows to relate the physical transformation occurring when you physically rotate the waveplates on your optical table and what occurs on the qubit state in the Bloch sphere. As a example, the action of the

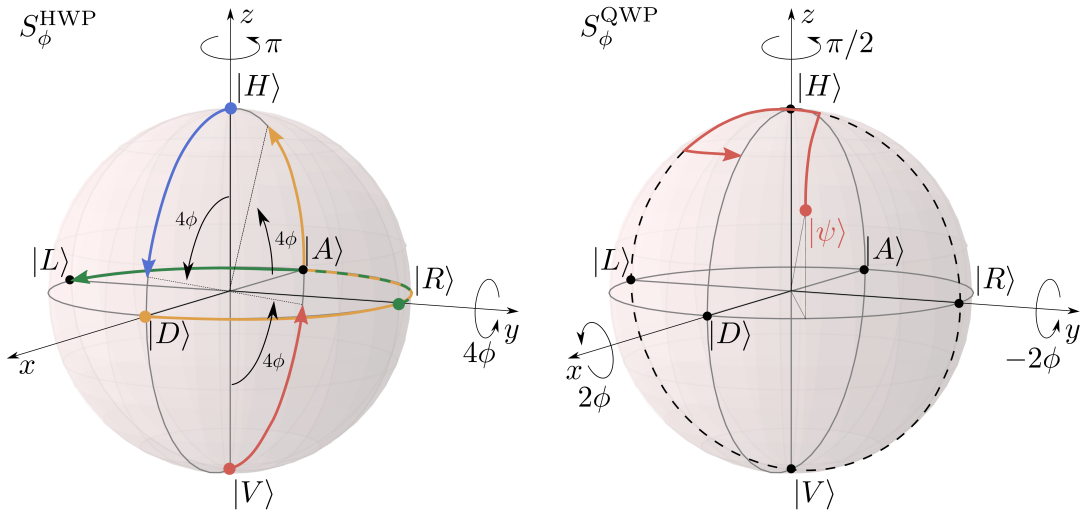

Figure 2.4: (**left panel**) Action of a HWP rotated by ϕ on the Bloch sphere. For example, when $\phi = 0$ we have that $|H\rangle \to |H\rangle, |V\rangle \to -|V\rangle$, and so $|D\rangle \leftrightarrow |A\rangle$ and $|R\rangle \leftrightarrow |L\rangle$. (**right panel**) With a QWP it is alway possible to turn a polarized qubit into a linearly polarized one.

HWP is given first by a rotation by π around the z-axis followed by a rotation of angle 4ϕ around the y-axis of the Bloch sphere, as represented in the left panel of Figure 2.4. Essentially, a HWP at ϕ performs the transformation $|D\rangle \leftrightarrow |A\rangle$ and $|R\rangle \leftrightarrow |L\rangle$ and then rotates the equator of the linear polarizations $\{H, D, V, A\}$ in the Bloch sphere by an angle 4ϕ. Physically, the HWP at ϕ reflects a light linearly polarized along the direction δ with respect the fast optical axis, causing a polarization rotation ending in the direction $\delta' = 2\phi - \delta$, e.g. a physical rotation of an angle 2ϕ for horizontal polarized light.

The action of a QWP on the Boch sphere is a rotation of an angle -2ϕ around the y-axis, followed by a rotation of 2ϕ around the x-axis and then by a rotation of $\pi/2$ around the z-axis. A single QWP is sufficient to transform any polarized (pure) state into a linearly polarized one, as shown in the right panel of Figure 2.4. Indeed, the rotation around the y-axis can bring any pure state $|\psi\rangle$ into the equator $\{H, R, V, L\}$ containing the circular polarizations $|R\rangle$ and $|L\rangle$, then the rotation around the x-axis moves the state along such equator and finally the rotation of $\pi/2$ around the z-axis brings the state to the equator $\{H, D, V, A\}$ of the linear polarizations.

Essentially, a QWP is used to transform circular polarized light into linearly polarized light and viceversa. Typically in the lab the QWP is placed with the fast optical axis at $0°$ or $45°$, and it acts on the Bloch sphere as represented in Figure 2.5.

It is worth noticing that, by using a triplet "QHQ" made by a QWP rotated by an angle α, a HWP rotated by β, and another QWP rotated by γ it is possible to implement any unitary transformation. Indeed, the induced unitary transformation on a generic

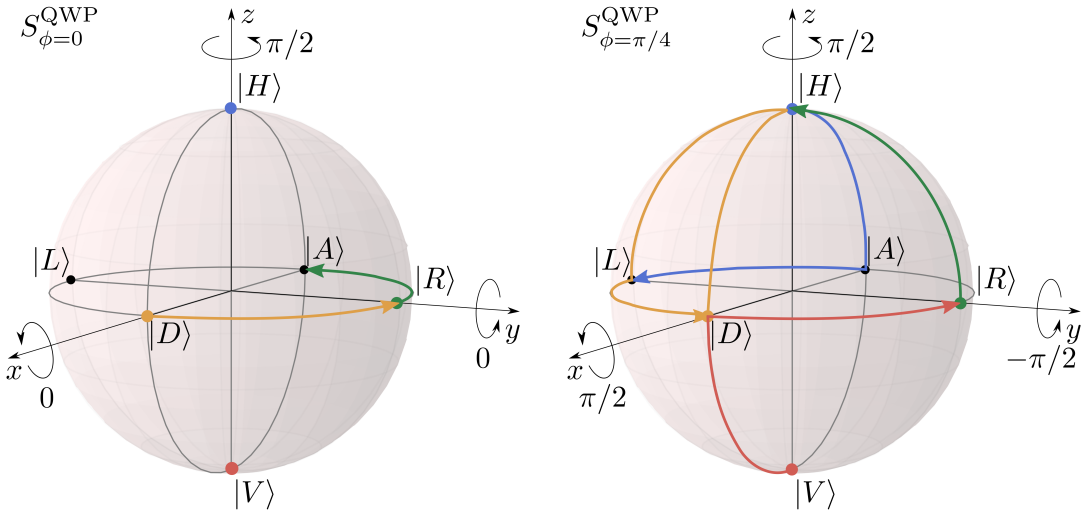

Figure 2.5: (**left panel**) Action of a QWP at $\phi = 0$ on the Bloch sphere: $|H\rangle \to |H\rangle$, $|V\rangle \to i\,|V\rangle$, and so $|D\rangle \to |R\rangle$, $|A\rangle \to |L\rangle$, $|R\rangle \to |A\rangle$, $|L\rangle \to |D\rangle$. (**right panel**) Action of a QWP at $\phi = \pi/4 = 45°$ on the Bloch sphere: $|H\rangle \to |L\rangle$, $|V\rangle \to -i\,|R\rangle$, and so $|D\rangle \to -i\,|D\rangle$, $|A\rangle \to |A\rangle$, $|R\rangle \to |H\rangle$, $|L\rangle \to -i\,|V\rangle$.

polarization-bases qubit is (neglecting the global phase)

$$\begin{aligned}\hat{U}_{\mathrm{QHQ}}(\alpha,\beta,\gamma) &:= S^{\mathrm{QWP}}_{\gamma} S^{\mathrm{HWP}}_{\beta} S^{\mathrm{QWP}}_{\alpha} \\ &= \hat{R}_z(\pi/2)\hat{R}_x(2\gamma)\hat{R}_y(-2\gamma)\,\hat{R}_y(4\beta)\hat{R}_z(\pi)\,\hat{R}_z(\pi/2)\hat{R}_x(2\alpha)\hat{R}_y(-2\alpha) \\ &= \hat{R}_z(\pi/2)\hat{R}_x(2\gamma)\hat{R}_z(\pi)\,\hat{R}_y(2\gamma-4\beta)\hat{R}_z(\pi/2)\hat{R}_x(2\alpha)\hat{R}_y(-2\alpha) \\ &= \hat{R}_y(2\gamma)\hat{R}_x(2\gamma-4\beta+2\alpha)\hat{R}_y(-2\alpha)\,, \end{aligned} \tag{2.95}$$

Hence, $\hat{U}_{\mathrm{QHQ}}$, being the composition of two rotations around the y-axis and one around the x-axis, can implement any unitary transformation according to (1.33).

Finally, it is worth noticing that a generic wave retarder with $\Gamma = \frac{2\pi}{\lambda} d\,\delta_n$ can implement a rotation around the z-axis of the Bloch sphere when *tilted* by an angle ϵ. Indeed, it introduces a factor $1/\cos\epsilon$ into the path length, since $d = d'\cos\epsilon$, where d' is the actual path inside the retarder. Hence, a tilted retarder (with horizontal fast axis, i.e. $\phi = 0$) can be written as

$$S^{\Gamma}_{\phi=0,\epsilon} = \begin{pmatrix} 1 & 0 \\ 0 & e^{i\frac{\Gamma}{\cos\epsilon}} \end{pmatrix} = e^{i\frac{\Gamma}{2\cos\epsilon}} \begin{pmatrix} e^{-i\frac{\Gamma}{2\cos\epsilon}} & 0 \\ 0 & e^{i\frac{\Gamma}{2\cos\epsilon}} \end{pmatrix} \equiv \hat{R}_z\left(\frac{\Gamma}{\cos\epsilon}\right), \tag{2.96}$$

which implements, in general, a rotation around the z-axis on the Bloch sphere, allowing for example the swapping $|D\rangle \leftrightarrow |A\rangle$ and $|R\rangle \leftrightarrow |L\rangle$. Also the triplet "QHR" made by a QWP rotated by α, a HWP rotated by β and a retarder tilted by ϵ can implement any unitary operation in the Bloch sphere, since

$$\hat{U}_{\mathrm{QHR}}(\alpha,\beta,\epsilon) := \hat{R}_z\left(\frac{\Gamma}{\cos\epsilon}\right) S^{\mathrm{HWP}}_{\beta} S^{\mathrm{QWP}}_{\alpha} = \hat{R}_z\left(\frac{\Gamma}{\cos\epsilon} - \frac{\pi}{2}\right)\hat{R}_x(2\alpha-4\beta)\hat{R}_y(-2\alpha) \tag{2.97}$$

is a composition of three rotations around three different axes of the Bloch sphere.

The polarizing beam-splitter.—Another commoly used polarization-based device is the *polarizing beam splitter* (PBS), which transmits an horizontal polarized impinging photon and reflects a vertical polarized one. Hence, a PBS allows to split horizontal and vertical polarizations in two spatially separated modes, as represented in Figure 2.6 according to the mode transformation

$$\hat{a}^\dagger_{1,H} \to \hat{b}^\dagger_{1,H} \,, \tag{2.98}$$
$$\hat{a}^\dagger_{1,V} \to \hat{b}^\dagger_{2,V} \,, \tag{2.99}$$
$$\hat{a}^\dagger_{2,H} \to \hat{b}^\dagger_{2,H} \,, \tag{2.100}$$
$$\hat{a}^\dagger_{2,V} \to \hat{b}^\dagger_{1,V} \,. \tag{2.101}$$

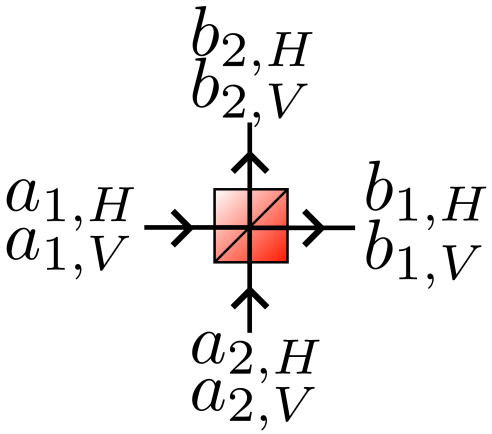

Figure 2.6: Input-Output modes for the PBS.

The PBS is used to implement projective measurements in a given polarization basis. For example, by using a single input port (the one labelled 1 Figure 2.6 for example), we have that the two spatially separated output modes are orthogonally polarized and in each path can be implemented a mean photon number measurement, by placing a single photon detector in the path. Indeed, the mode transformation is

$$\hat{a}^\dagger_{1,H} \to \hat{b}^\dagger_{1,H} \,, \quad \hat{a}^\dagger_{1,V} \to \hat{b}^\dagger_{2,V} \tag{2.102}$$

and the expectation values of the operators $\hat{n}_{b_i}$ with spatial index $i = 1,2$, when the state is $|\psi\rangle = \alpha\,|H\rangle_{a_1} + \beta\,|V\rangle_{a_1} \to \alpha\,|H\rangle_{b_1} + \beta\,|V\rangle_{b_2}$ is

$$\langle \hat{n}_{b_1} \rangle = |\alpha|^2 \,, \quad \langle \hat{n}_{b_2} \rangle = |\beta|^2 \,. \tag{2.103}$$

For this reason, a PBS by itself performs a projective measurement in the $\{|H\rangle, |V\rangle\}$ basis. However, by adding a QWP or a HWP (or both) in front of the PBS it is possible to

implement a projective measurement in any basis. Let's write the generic input state (in the a_1 mode) as

$$\begin{aligned}|\psi\rangle &= \alpha|H\rangle + \beta|V\rangle \\ &= \frac{1}{\sqrt{2}}(\alpha+\beta)|D\rangle + \frac{1}{\sqrt{2}}(\alpha-\beta)|A\rangle \\ &= \frac{1}{\sqrt{2}}(\alpha-i\beta)|R\rangle + \frac{1}{\sqrt{2}}(\alpha+i\beta)|L\rangle \ .\end{aligned} \tag{2.104}$$

For example, a HWP rotated by $\phi = 22.5 = \pi/8$ in front of the PBS implements the projective measurement onto the $\{|D\rangle, |A\rangle\}$ basis since the action of the HWP produces

$$|\psi\rangle = \alpha|H\rangle + \beta|V\rangle \xrightarrow{S^{\text{HWP}}_{22.5^\circ}} |\psi'\rangle = \alpha|D\rangle + \beta|A\rangle = \frac{1}{\sqrt{2}}(\alpha+\beta)|H\rangle + \frac{1}{\sqrt{2}}(\alpha-\beta)|V\rangle \tag{2.105}$$

and we have after the PBS that

$$\langle \hat{n}_{b_1}\rangle = \frac{1}{2}|\alpha+\beta|^2 \ , \quad \langle \hat{n}_{b_2}\rangle = \frac{1}{2}|\alpha-\beta|^2 \ , \tag{2.106}$$

as expected in a measurement of $|\psi\rangle$ in the $\{|D\rangle, |A\rangle\}$ basis.

On the other hand, a QWP rotated by $\phi = 45 = \pi/4$ in front of the PBS implements the projective measurement onto the $\{|R\rangle, |L\rangle\}$ basis since the action of the QWP produces

$$|\psi\rangle = \alpha|H\rangle + \beta|V\rangle \xrightarrow{S^{\text{QWP}}_{45^\circ}} |\psi'\rangle = \alpha|L\rangle - i\beta|R\rangle = \frac{1}{\sqrt{2}}(\alpha-i\beta)|H\rangle - i\frac{1}{\sqrt{2}}(\alpha+i\beta)|V\rangle \tag{2.107}$$

and we have after the PBS that

$$\langle \hat{n}_{b_1}\rangle = \frac{1}{2}|\alpha-i\beta|^2 \ , \quad \langle \hat{n}_{b_2}\rangle = \frac{1}{2}|\alpha+i\beta|^2 \ , \tag{2.108}$$

as expected in a measurement of $|\psi\rangle$ in the $\{|R\rangle, |L\rangle\}$ basis.

2.2.3 Time-bin encoding

With the formalism introduced in Section 2.1.3 it is possible to describe the *time-bin* encoding, that we will exploit in single-photon interferometry along Space channels in Chapter 5.

Let's suppose that a 1-photon pulse centered at t_0 enters the unbalanced Mach-Zehnder interferometer of Figure 2.7 in the mode a_1, that is,

$$\left|1_{a_1,\xi_{t_0}}\right\rangle = \hat{a}^\dagger_{1,\xi_{t_0}}|\text{vac}\rangle \ . \tag{2.109}$$

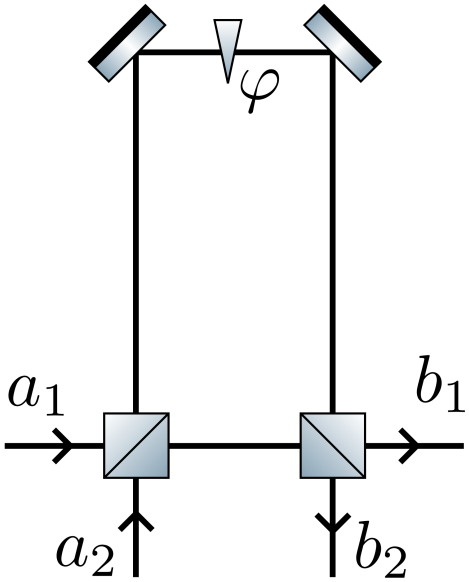

Figure 2.7: Input-Output modes an unbalanced Mach-Zender interferometer with the additional phase-shift φ.

We can describe the interferometer as a linear filter consisting of a delay element and a phase modulator of value φ sandwiched between two 50:50 beam splitters. The two arms — short "S" and long "L" — are unbalanced, i.e. the *path difference* $\Delta l := c\Delta t = L - S$ is not zero, and it is set to avoid single photon interference. This can be achieved taking the temporal imbalance Δt much greater than the coherence time of the pulse

$$\Delta t \gg \tau_c \,. \tag{2.110}$$

The scattering matrix of the unbalanced interferometer can be written as a function of the frequency ω given the imbalance Δt, that is, the *delay* introduced by the long arm relative to the short one, and the value of the possible additional phase shift φ

$$S(\omega;\Delta t,\varphi) := \frac{1}{2}\begin{pmatrix} 1-e^{i(\omega-\omega_0)\Delta t}e^{i\varphi} & i(e^{i(\omega-\omega_0)\Delta t}e^{i\varphi}+1) \\ i(e^{i(\omega-\omega_0)\Delta t}e^{i\varphi}+1) & e^{i(\omega-\omega_0)\Delta t}e^{i\varphi}-1 \end{pmatrix}. \tag{2.111}$$

We can rewrite the input operators as a function of the output ones by using (2.52) to

obtain

$$\begin{aligned}\hat{a}^{\dagger}_{1,\xi_{t_0}} &= \sum_{j=1}^{2}\int d\omega \xi_{t_0}(\omega) S_{j1}(\omega;\Delta t,\varphi)\hat{b}^{\dagger}_{j}(\omega)\\ &= \int d\omega\ \xi_{t_0}(\omega)\frac{1}{2}(1-e^{i(\omega-\omega_0)\Delta t}e^{i\varphi})\hat{b}^{\dagger}_{1}(\omega)+\int d\omega\ \xi_{t_0}(\omega)\frac{i}{2}(e^{i(\omega-\omega_0)\Delta t}e^{i\varphi}+1)\hat{b}^{\dagger}_{2}(\omega)\\ &= \int \frac{d\omega}{2}\left[\xi_{t_0}(\omega)-\xi_{t_0+\Delta t}(\omega)e^{i\varphi}\right]\hat{b}^{\dagger}_{1}(\omega)+\int \frac{d\omega}{2}\left[i\xi_{t_0+\Delta t}(\omega)e^{i\varphi}+i\xi_{t_0}(\omega)\right]\hat{b}^{\dagger}_{2}(\omega)\\ &= \frac{1}{2}\left(\hat{b}^{\dagger}_{1,\xi_{t_0}}-e^{i\varphi}\hat{b}^{\dagger}_{1,\xi_{t_0+\Delta t}}+ie^{i\varphi}\hat{b}^{\dagger}_{2,\xi_{t_0+\Delta t}}+i\hat{b}^{\dagger}_{2,\xi_{t_0}}\right), \end{aligned} \tag{2.112}$$

where we observed that

$$\xi_{t_0}(\omega)e^{i(\omega-\omega_0)\Delta t}\equiv\xi_{t_0+\Delta t}(\omega) \tag{2.113}$$

by using (2.42).

If we focused only on the output port b_1, the re-normalized state exiting the interferometer is

$$\frac{1}{\sqrt{2}}\left(\hat{b}^{\dagger}_{1,\xi_{t_0}}-e^{i\varphi}\hat{b}^{\dagger}_{1,\xi_{t_0+\Delta t}}\right)|\text{vac}\rangle\equiv\frac{1}{\sqrt{2}}\left(\left|1_{b_1,\xi_{t_0}}\right\rangle-e^{i\varphi}\left|1_{b_1,\xi_{t_0+\Delta t}}\right\rangle\right). \tag{2.114}$$

and the action of the interferometer in (2.114) can be re-written in terms of the wavepacket amplitude in the time-domain as

$$\xi_{t_0}(t)\to\frac{1}{\sqrt{2}}\left(\xi_{t_0}(t)-\xi_{t_0+\Delta t}(t)\right)=\frac{1}{\sqrt{2}}\left(\xi_{t_0}(t)-e^{i(\varphi-\omega_0\Delta t)}\xi_{t_0}(t-\Delta t)\right). \tag{2.115}$$

The state in (2.114) is a superposition of two temporal time-bins, delayed by Δt one with respect to the other. The two states are orthonormal and can be written as a basis for $\mathbb{C}^2$, hence giving a qubit. The two basis states are usually rewritten as $|S\rangle:=\left|1_{\xi_{b_1,t_0}}\right\rangle$ and $|L\rangle:=\left|1_{b_1,\xi_{t_0+\Delta t}}\right\rangle$ referring to the path took in the interferometer, and the superposition (2.114)

$$|\psi\rangle_{\text{TB}}=\frac{1}{\sqrt{2}}\left(|S\rangle-e^{i\varphi}|L\rangle\right) \tag{2.116}$$

is called *time-bin* (TB) qubit. It is worth noticing that, by properly choosing the additional relative phase-shift φ between the two arms of the interferometer is it possible to obtain any phase relation between the two basis states. We will often exploit time-bin encoding and time-bin qubits in the following chapters.

We notice that, if the 1-photon pulse entering the interferometer is replaced by a coherent-state pulse, the output state is a coherent-state pulse in two temporal modes delayed by Δt or, in other word, two coherent-state pulses delayed by Δt. Indeed, following

the discussion of Section 2.2.1, using the displacement operator for the coherent-state pulse in mode a_1

$$\hat{D}_{a_1,\xi_{t_0}}(\alpha) = e^{-|\alpha|^2/2} e^{\alpha \hat{a}^\dagger_{1,\xi_{t_0}}} e^{-\alpha^* \hat{a}_{1,\xi_{t_0}}} \ , \tag{2.117}$$

replacing (2.56) with

$$\hat{a}^\dagger_{1,\xi_{t_0}} \to \frac{1}{\sqrt{2}} \left(\hat{b}^\dagger_{1,\xi_{t_0}} - e^{i\varphi} \hat{b}^\dagger_{1,\xi_{t_0+\Delta t}} \right) \tag{2.118}$$

according to (2.114), we have that

$$|\alpha\rangle_{a_1,\xi_{t_0}} := \hat{D}_{a_1,\xi_{t_0}}(\alpha)|\text{vac}\rangle \to \left| \frac{\alpha}{\sqrt{2}} \right\rangle_{b_1,\xi_{t_0}} \left| \frac{e^{i(\pi+\varphi)}\alpha}{\sqrt{2}} \right\rangle_{b_1,\xi_{t_0+\Delta t}} . \tag{2.119}$$

In the following chapters we will usually indicate a 1-photon state and a coherent-state pulse in a given spatial mode according to:

$$|1\rangle_{t_0} \equiv \left|1_{\xi_{t_0}}\right\rangle \equiv |S\rangle \tag{2.120}$$

$$|1\rangle_{t_0+\Delta t} \equiv \left|1_{\xi_{t_0+\Delta t}}\right\rangle \equiv |L\rangle \tag{2.121}$$

$$|\alpha\rangle_{t_0} \equiv |\alpha\rangle_{\xi_{t_0}} \tag{2.122}$$

$$|\alpha\rangle_{t_0+\Delta t} \equiv |\alpha\rangle_{\xi_{t_0+\Delta t}} \ . \tag{2.123}$$

In this way, the action of an unbalanced Mach-Zehnder interferometer (uMZI) on a 1-photon pulse and on a weak-coherent-state pulse, according to the discussion in Section 2.2.1, and equation (2.62) in particular, allows to obtain true time-bin qubits and its weak-coherent approximation via:

$$|1\rangle_{t_0} \xrightarrow{\text{uMZI}} \frac{1}{\sqrt{2}} \left(|1\rangle_{t_0} - e^{i\varphi} |1\rangle_{t_0+\Delta t} \right) \equiv |\psi\rangle_{\text{TB}} \ , \tag{2.124}$$

$$|\alpha\rangle_{t_0} \xrightarrow{\text{uMZI}} \left| \frac{\alpha}{\sqrt{2}} \right\rangle_{t_0} \left| \frac{e^{i(\pi+\varphi)}\alpha}{\sqrt{2}} \right\rangle_{t_0+\Delta t} \xrightarrow{|\alpha|^2 \ll 1} \frac{1}{\sqrt{2}} \left(|1\rangle_{t_0} - e^{i\varphi} |1\rangle_{t_0+\Delta t} \right) \equiv |\psi\rangle_{\text{TB}} \ . \tag{2.125}$$

2.3 How to generate entangled photons

As discussed above, weak-coherent sources are not suitable to perform two-photon experiments. Furthermore, true entanglement cannot be obtained by exploiting two independent weak coherent sources. Indeed, most of experiments exploiting entanglement (e.g., polarization or energy-time entanglement) is based on a non-linear process called Spontaneous Parametric Down Conversion. Let's describe this effect and the typical setups used in Quantum Optics experiments involving photon entanglement.

2.3.1 Spontaneous Parametric Down Conversion

Entangled photons are commonly produces by exploiting Spontaneous Parametric Down Conversion (SPDC) sources [12, 14, 17, 18]. SPDC is due to a non-linear effect occurring in the interaction between a strong radiation, called *pump*, with a media in which the induced polarization is strongly affected by the pump radiation itself beyond the usual linear response. In this section, we will focus on non-linear media, i.e. crystals, in which the polarization can be expanded in a power series of the applied pump field

$$\hat{P}_i = \chi^{(1)}_{ij}\hat{E}_j + \chi^{(2)}_{ijk}\hat{E}_j\hat{E}_k + \chi^{(3)}_{ijkl}\hat{E}_j\hat{E}_k\hat{E}_l + \cdots , \tag{2.126}$$

where $\chi^{(m)}$ is the m-th order electric susceptibility tensor and we adopted the Einstein's convention in which repeated indexes are added. In SPDC crystals, the key ingredient is the 2-nd order electric susceptibility coefficient, which allow to write down the 2-nd order contribution to the Hamiltonian of the system as

$$\hat{H}^{(2)} = \epsilon_0 \int_V d^3\mathbf{r}\, \chi^{(2)}_{ijk}\hat{E}_i\hat{E}_j\hat{E}_k , \tag{2.127}$$

since the energy density is $\epsilon_0\hat{E}_i\hat{P}_i$.

We will not discuss the details of the generation process, which can be found in many references, as [18] and therein, and we will limit ourself to present the conceptual steps allowing to describe the quantum state of the two entangled photons generated by SPDC. By expanding the electrical fields $\hat{E}_i$ in Fourier components, as done in Section 2.1.1 for the potential vector, it is possible to write the *interaction Hamiltonian* $\hat{H}_{\mathrm{I}}(t)$ for the system

$$\hat{H}_{\mathrm{I}}(t) = \epsilon_0 \int_V d^3\mathbf{r} \int d^3\mathbf{k}_{\mathrm{s}} d^3\mathbf{k}_{\mathrm{i}} \chi^{(2)}_{ijk} \hat{E}^{(-)}_{\mathrm{p},i}(\mathbf{k}_{\mathrm{p}}) \hat{E}^{(+)}_{\mathrm{s},j}(\mathbf{k}_{\mathrm{s}}) \hat{E}^{(+)}_{\mathrm{i},k}(\mathbf{k}_{\mathrm{i}}) + \mathrm{H.c.} , \tag{2.128}$$

where the electrical field operators are labelled according to p = "pump", s = "signal" and i = "idler", and they are proportional to the creation and annihilation operators for the given mode specified by the wavevector $\mathbf{k}$ according to [12]:

$$\hat{E}^{(-)}(\mathbf{k}) := i\sqrt{\frac{2\pi\hbar\omega(\mathbf{k})}{V}}\hat{a}^\dagger(\mathbf{k},\omega(\mathbf{k})) , \quad \hat{E}^{(+)}(\mathbf{k}) := i\sqrt{\frac{2\pi\hbar\omega(\mathbf{k})}{V}}\hat{a}(\mathbf{k},\omega(\mathbf{k})) . \tag{2.129}$$

Signal and idler are the two labels given to the twin photons generated by the SPDC process.

The conversion rates for the process depend on the 2-nd order susceptibility $\chi^{(2)}$, which typically has extremely low efficiencies in the range 10^{-7} to 10^{-11}. Hence, in order to obtain significant output in the signal and idler beams it is necessary to pump the medium

with a very strong coherent field which is modelled as a classical field obtained from a strong laser.

The interaction Hamiltonian describes the fact that in the SDPC process a pump photon is destroyed by $\hat{E}_{\mathrm{p}}^{(-)}(\mathbf{k}_{\mathrm{p}})$, while two twin photons, the signal and the idler, are generated by $\hat{E}_{\mathrm{s}}^{(+)}(\mathbf{k}_{\mathrm{s}})$ and $\hat{E}_{\mathrm{i}}^{(+)}(\mathbf{k}_{\mathrm{i}})$. The interaction Hamiltonian allows to calculate the state of the system via the time-dependend perturbation theory [3, 5]

$$|\Psi\rangle := \frac{1}{i\hbar}\int dt\ \hat{H}_{\mathrm{I}}(t)\,|\mathrm{vac}\rangle\ , \tag{2.130}$$

which results proportional to [12]

$$|\Psi\rangle \propto \int d^3\mathbf{k}_{\mathrm{s}} d^3\mathbf{k}_{\mathrm{i}}\,\delta\left(\omega_{\mathrm{p}}-\omega_{\mathrm{s}}-\omega_{\mathrm{i}}\right)\delta\left(\mathbf{k}_{\mathrm{p}}-\mathbf{k}_{\mathrm{s}}-\mathbf{k}_{\mathrm{i}}\right)A_{\mathrm{p}}(\mathbf{k}_{\mathrm{p}},\omega_{\mathrm{p}})\,|\mathbf{k}_{\mathrm{s}},\omega_{\mathrm{s}}\rangle_{\mathrm{s}}\,|\mathbf{k}_{\mathrm{i}},\omega_{\mathrm{i}}\rangle_{\mathrm{i}}\ , \tag{2.131}$$

where $A_{\mathrm{p}}(\mathbf{k}_{\mathrm{p}},\omega_{\mathrm{p}})$ is the pump profile in the momentum space and

$$|\mathbf{k}_{\mathrm{s}},\omega_{\mathrm{s}}\rangle_{\mathrm{s}} := \hat{a}_{\mathrm{s}}^{\dagger}(\mathbf{k}_{\mathrm{s}},\omega_{\mathrm{s}})\,|0\rangle_{\mathrm{s}} \tag{2.132}$$

$$|\mathbf{k}_{\mathrm{i}},\omega_{\mathrm{i}}\rangle_{\mathrm{i}} := \hat{a}_{\mathrm{i}}^{\dagger}(\mathbf{k}_{\mathrm{i}},\omega_{\mathrm{i}})\,|0\rangle_{\mathrm{i}}\ . \tag{2.133}$$

The two delta functions in (2.131) provide the *phase-matching conditions*

$$\omega_{\mathrm{p}} = \omega_{\mathrm{s}} + \omega_{\mathrm{i}}\ , \tag{2.134}$$

$$\mathbf{k}_{\mathrm{p}} = \mathbf{k}_{\mathrm{s}} + \mathbf{k}_{\mathrm{i}}\ , \tag{2.135}$$

which express the conservation of energy and momentum. Actually, crystals are of finite size, and the efficiency of pair production depends on the length L of the crystal along the direction z of the pump propagation. More detailed calculations, as in [18], taking into account the finite region V of integration in $\hat{H}_{\mathrm{I}}(t)$, lead to quasi phase-matching conditions, in which a tolerable mismatch $\Delta k_z = k_{\mathrm{p},z} - k_{\mathrm{i},z} - k_{\mathrm{s},z} \neq 0$, and so $\Delta\omega = \omega_{\mathrm{p}} - \omega_{\mathrm{i}} - \omega_{\mathrm{s}} \neq 0$, is allowed. The phase-matching conditions can be achieved by using for example the BBO crystal (β-BaB_2O_4), as in the experiment explained in Chapter 3.

2.3.2 Polarization entanglement

Actually, two kinds of phase-matching conditions are usually adopted, depending on the extraordinary (e) or ordinary (o) polarization of the pump and of the SPDC photons [12, 14, 17]:

$$\text{Type-I: } \mathrm{e} \to \mathrm{o}+\mathrm{o}\ , \quad \text{Type-II: } \mathrm{e} \to \mathrm{e}+\mathrm{o}\ . \tag{2.136}$$

Assuming that the two photons are *degenerate*, i.e., they are generated with the same energy $\omega_{\mathrm{i}} = \omega_{\mathrm{s}} = \omega_{\mathrm{p}}/2$, in Type-I SPDC the phase-matching conditions constrain the photons to

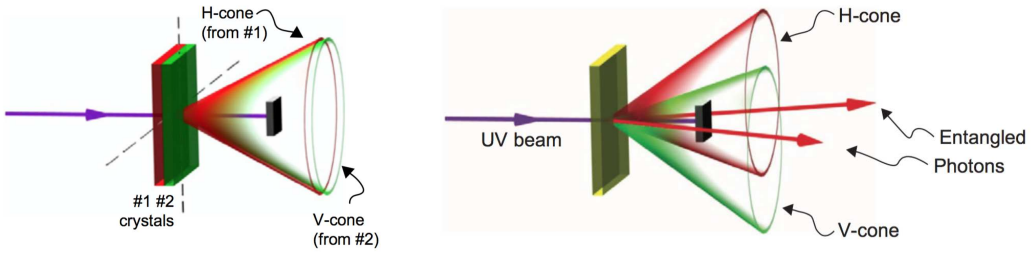

Figure 2.8: **(left panel)** Type-I polarization entanglement source [19]. **(right panel)** Type-II polarization entanglement source [20]. Pictures taken from [17].

being emitted on the opposite directions on the surface of a o-polarized cone, as in the left panel of Figure 2.8. On the other hand, with Type-II phase-matching, the two degenerate photons are emitted over two different mutually crossing emission cones, as in the right panel of Figure 2.8.

By exploiting the different phase-matching conditions, it is possible to obtained polarization entanglement. Let's see for example the polarization entanglement source proposed by Kwiat *et al.* [19], in which, by exploiting two paired Type-I crystals oriented orthogonally one respect the other, and pumping the pair with a diagonally polarized pump beam, it is possible to make the first crystal produce, let's say, a pair of photons $|H\rangle_i|H\rangle_s$, and thus the second will generate the pair $|V\rangle_i|V\rangle_s$. Since these two events are coherent within the coherence time of the pump, the Bell states

$$|\Phi^{\pm}\rangle = \frac{1}{\sqrt{2}}(|H\rangle_s|H\rangle_i \pm |V\rangle_s|V\rangle_i) \tag{2.137}$$

are easily generated.

On the other hand, Type-II SPDC is commonly adopted to generate the Bell states

$$|\Psi^{\pm}\rangle = \frac{1}{\sqrt{2}}(|H\rangle_s|V\rangle_i \pm |V\rangle_s|H\rangle_i) \ , \tag{2.138}$$

by taking the directions in which the two emitting cones intersect, as in [20].

During my PhD, my colleagues and I implemented both a continuous-wave (CW) pumped Type-I SPDC source that was used for didactic purposes, and a pulsed Type-II SPDC source, which was exploited in the time-bin experiment presented in Chapter 3. As an example, in Figure 2.9 is presented a picture of our setup for generating polarization entanglement via Type-II SPDC.

2.3.3 Energy-time entanglement

The two-photons generated via SPDC are not only entangled in polarization. Indeed, another available degree of freedom is given by the conjugate variables energy and time.

Figure 2.9: A picture of our pulsed Type-II polarization entanglement source.

Indeed, we can rewrite the SPDC state of equation (2.131) by selecting two directions $\mathbf{k}_s$, $\mathbf{k}_i$ and by using the fact that the frequency $\omega_\mathbf{k}$ as

$$|\Psi\rangle \propto \int d\omega_s d\omega_i \delta(\omega_p - \omega_i - \omega_s) A_p(\omega_p) |\omega_s\rangle_s |\omega_i\rangle_i \ , \tag{2.139}$$

where $A_p(\omega_p)$ is the pump profile (with coherence time τ_p) and $|\omega\rangle := \hat{a}^\dagger(\omega)|\text{vac}\rangle$ is the continuous-mode creator operator for the frequency ω. In the degenerate case when $\omega_i = \omega_s$ the re-normalized state in (2.139) can be written as

$$|\Psi\rangle_{ET} = \int d\omega \, |\omega\rangle_i |\omega\rangle_s \ , \tag{2.140}$$

which is know as the *energy-time* entangled state. By Fourier transforming the continuous mode operator $\hat{a}(\omega)$ according to (2.36), the energy-time entangled state can be written as

$$|\Psi\rangle_{ET} = \int dt \, |t\rangle_i |t\rangle_s . \tag{2.141}$$

The SPDC twin photons are emitted at the same time and emission events which occur within the coherence time τ_p of the pump are coherent. Energy-time entanglement is at the basis of time-bin entanglement, where a pulsed laser replaces the CW one, as we will see in Chapter 3.

Chapter 3

Realization of a *genuine* time-bin entanglement source

Twin entangled photons are an invaluable resource for fundamental tests of Quantum Mechanics and the implementation of Quantum Information protocols. In particular, *time-bin entanglement* is widely exploited to reach these purposes both via free-space or in fiber-based systems, due to the robustness and simplicity of its implementation. However, all time-bin entanglement implementations realized so far suffer from an intrinsic *post-selection loophole*, which undermines their usefulness. In this chapter we present the realization of a "genuine" time-bin entanglement source, which is free of such post-selection loophole. Using this setup we obtained a violation of the Bell-CHSH inequality by more than nine standard deviations. Some contents of this chapter are part of our work [21].

My friends and colleagues Marco Avesani, Costantino Agnesi and I during a summer school in Baiona (May 2018).

3.1 Franson's Bell test and the post-selection loophole

In 1989 Franson proposed an interferometric scheme to realize a Bell test via two-photon interferometry [22]. In his idea, a pair of entangled photons is sent to two unbalanced interferometers (as the one in Figure 2.7) acting as two measurement stations, that are called Alice and Bob respectively. By exploiting the local phase-shifts (φ_A, φ_B) introduced by the two interferometers as the two measurement choices (x, y) of a Bell test like the one described in Section 1.2.2, and labelling the output ports of the two interferometers as two dichotomous variables $a, b = \pm 1$, it is possible to rule out local realistic models by violating the CHSH inequality (1.48), as we will review in the following.

Franson's idea was first implemented by exploiting the *energy-time* entanglement, which can be easily created by pumping a non-linear crystal with a continuous-wave (CW) laser, as described in Section 2.3.3 and realized for example in [23, 24, 25]. In fact, the two emitted photons are generated at the same instant, but the emission time is uncertain within the coherence time of the source, thus leading to indistinguishability in the alternative paths the photons will take in the measurement stations. Extending Franson's idea, *time-bin entanglement* was introduced by Brendel *et al.* in 1999 [26]: the CW laser is replaced by a pulsed laser shining the non-linear crystal after passing through an unbalanced "pump" interferometer. Now, the pair of photons can be emitted at two possible times, depending on the path taken by the pump-pulse in the first interferometer (see Figure 3.1**a**). Both energy-time and time-bin entanglement have been widely used to distribute entan-

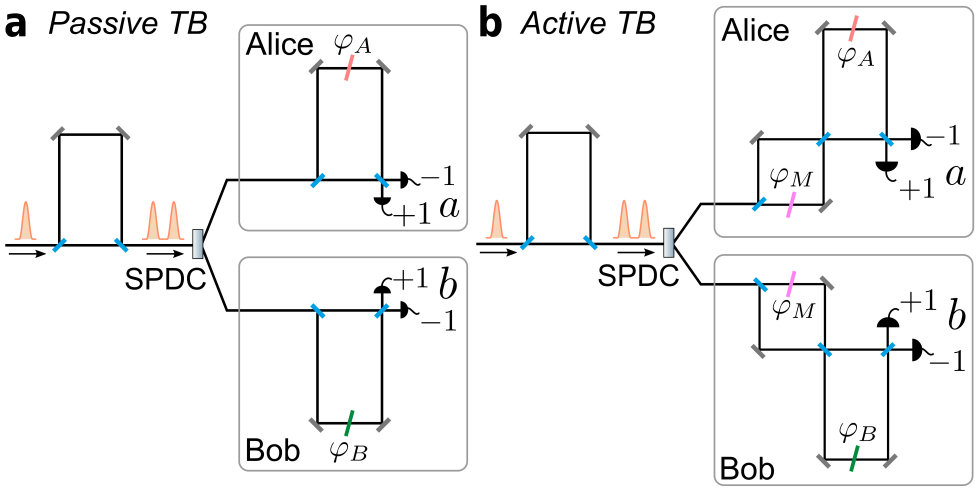

Figure 3.1: Time-bin schemes to realize a Bell-test *à la* Franson. **(a)** In the passive time-bin, by post-selecting the events detected in coincidence only in the central time-slot, Alice and Bob can violate the Bell-CHSH inequality, but such scheme is affected by an intrinsic PSL. **(b)** In the active time-bin, the passive beam splitter is replaced by a balanced MZI acting as an optical switch. By exploiting a fast phase modulator φ_M in one arm of the balanced interferometer, Alice and Bob can violate the Bell-CHSH inequality without discarding any data, i.e. this scheme is free of the post-selection loophole.

glement over long distances [27, 28, 29, 30, 31], and to realize fiber-based cryptographic systems [32, 33], due to the simplicity of their implementations.

However, Aerts *et al.* noted that Franson's Bell-test is intrinsically affected by the so-called *post-selection loophole* [38], which is present independently to the other common loopholes (eg., locality and detection) that could affect local-realistic tests [39]. In fact, in Franson's configuration, Alice and Bob should post-select only the indistinguishable events occurring within a coincidence window Δw centered around a certain time t_0, discarding those photons arriving at $t_0 - \Delta t$ and $t_0 + \Delta t$. When performing such post-selection, there exists a local-hidden-variable (LHV) model reproducing the quantum predictions [38, 40]. The reason for this is that a LHV model admits the local delays to depend on the local parameter (φ_A or φ_B), but Alice and Bob need to compare these delays to perform the post-selection. Therefore, even though the physical system is completely local, the measurement-process post-selection invalidates the locality assumption required to derive the Bell-CHSH inequality. The same loophole affects the *passive* time-bin entanglement scheme shown in Figure 3.1**a**, invalidating Bell's inequality as test of local realism and enabling the hacking of Franson' scheme when used with cryptographic purposes [41]. Indeed, the Bell-test gives false evidence, since the apparent violation would tell users the setup is secure, while it is in fact insecure because of the post-selection loophole.

Many modifications to Franson's original scheme have been proposed to address the post-selection loophole. The first one is due to Strekalov *et al.* [42], and exploited *hyper-entanglement* in polarization and energy-time to overcome the post-selection loophole by replacing the beam splitters of Alice's and Bob's interferometers with polarizing ones. This scheme was experimentally implemented [43] and recently realized in an intra-city free-space link [44]. However, requiring entanglement in both energy-time and polarization, this solution increases the experimental complexity.

Afterwards, the proposal in [45] by Cabello *et al.* modified the geometry of the interferometers by interlocking them in a *hug configuration*, and introduced a *local* post-selection, which does not require communication between Alice and Bob. In this way, *genuine* energy-time entanglement can be generated, i.e. a Bell's test exploiting energy-time entanglement which is not affected by the post-selection loophole. Soon after this proposal had been conceived, table-top experiments were realized [46, 47] and a few years later the distribution of genuine energy-time entanglement through 1 km of optical fibers [48] and its implementation in an optical fiber-network was reported [49]. However, the hug configuration requires to stabilize two long interferometers whose extension is determined by the distance between Alice and Bob. Hence, the larger the separation is, the more demanding the stabilization becomes.

In the case of time-bin entanglement, the original proposal already mentioned the use of *active* switches [26], such as movable mirrors synchronized with the source, instead of passive beam splitters, to prevent discarding any data. This solution can also be exploited to overcome the post-selection loophole, as discussed in details in [40], but no such scheme has been realized so far.

We implemented, for the first time, a genuine time-bin entanglement scheme allowing the violation of a Bell's inequality free of the post-selection loophole. In our scheme, the active switches are realized by replacing the first beam splitter, in each unbalanced interferometer of the measurement stations, with another balanced interferometer with a fast phase-shifter in one arm, as sketched in Figure 3.1**b** (*active time-bin*). By actively synchronizing the phase-shifter with the pump pulses, it is possible to use the full detection statistics, overcoming the post-selection-loophole. The independence between Alice' and Bob's terminals, the relaxed stabilization requirements, as well as the compliance with off-the-shelves components open the possibility to exploit such scheme over long distances, paving the way to a conclusive loophole-free Bell-test, as the ones reported in [34, 35, 36, 37], based on time-bin entanglement.

3.2 POVM analysis of time-bin entanglement schemes

In the *passive* time-bin (TB) scheme, a pump Mach-Zehnder interferometer (MZI) with a temporal imbalance equal to Δt is used to split a short coherent light pulse into two, as sketched in Figure 3.1**a**. This light is focused into a non-linear crystal producing photon pairs via SPDC, as discussed in Section 2.3.1. Each photon of the pump pulse is transformed according to the discussion in Section 2.2.3 by the pump interferometer into the time-bin superposition

$$|\gamma\rangle_p = \frac{1}{\sqrt{2}}\left(|S\rangle_p - e^{i\phi_p}|L\rangle_p\right), \tag{3.1}$$

where $|S\rangle$ and long $|L\rangle$ refer to the path the pump photon took in the pump interferometer, $\phi_p = 2\pi\Delta\lambda/\lambda_p$ with $\lambda_p = 2\pi c/\omega_p$ is the wavelength of the pump and $\Delta\lambda = \mathrm{mod}(c\Delta t, \lambda_p)$ measures how many λ_p are contained in the imbalance $c\Delta t$. The SPDC process transforms, with a certain probability, $|\gamma\rangle_p$ into the two-photon state

$$|2\gamma\rangle = \frac{1}{\sqrt{2}}\left(|S\rangle_A|S\rangle_B - e^{i\phi_p}|L\rangle_A|L\rangle_B\right), \tag{3.2}$$

where the indexes A and B represent the generated photons that are sent to Alice and Bob measurement stations. Since the pump is a pulsed laser, it is not monochromatic and thus

it has a finite coherent time τ_c and a spectral bandwidth Δ. Hence, contrary to energy-time entanglement, the instant of creation is localized within the temporal duration (2δ) of the pulse (centered around a certain $\tilde{t}$)

$$\int dt\,|t\rangle_A\,|t\rangle_B \to \int_{\tilde{t}-\delta}^{\tilde{t}+\delta} dt\,|t\rangle_A\,|t\rangle_B \equiv |\tilde{t}\rangle_A\,|\tilde{t}\rangle_B\ . \tag{3.3}$$

Since the pump photon is in a superposition of two possible times, also the photon pair can be generated at two discrete emission times. Hence, by optimizing the pump energy to suppress the generation of double photon-pairs and assuming $\phi_p = \pi$, the entangled Bell state

$$|\Phi^+\rangle = \frac{1}{\sqrt{2}}(|S\rangle_A\,|S\rangle_B + |L\rangle_A\,|L\rangle_B) \tag{3.4}$$

is obtained. We assumed $\phi_p = \pi$, a condition that is easily obtainable in the experiment, to simplify the next calculations.

Each measurement-station is composed by an unbalanced MZI that has the same imbalance Δt of the pump-interferometer and can introduce a further phase shift (φ_A, φ_B). The output ports of each interferometer are followed by two single-photon detectors, and the possible outcomes are labeled $a = \pm 1$ and $b = \pm 1$ for Alice and Bob respectively, depending on which detector clicks.

In the passive TB scheme, each photon of the pair can be detected only at three possible distinct times, indicated by $(t_0 - \Delta t, t_0, t_0 + \Delta t)$, due to the pump- and measurement-interferometers. By post-selecting the detection events that occur in the central time-slot only, Alice's measurement station realizes the projection $\{\hat{P}_{a|\varphi_A}\}$ defined by

$$\hat{P}_{a|\varphi_A} = |\psi_a^{\varphi_A}\rangle\langle\psi_a^{\varphi_A}| \tag{3.5}$$

where

$$|\psi_a^{\varphi_A}\rangle = \frac{1}{\sqrt{2}}\left(|S\rangle + a\ \mathrm{e}^{i\varphi_A}\,|L\rangle\right)\ . \tag{3.6}$$

In this way, for any (normalized) input state $|\phi\rangle = \alpha\,|S\rangle + \beta\,|L\rangle$, a click in the a-detector given the delay φ_A follows the probability distribution $p(a|\varphi_A) = \langle\phi|\,\hat{P}_{a|\varphi_A}\,|\phi\rangle = \frac{1}{2}|\alpha + ae^{-i\varphi_A}\beta|^2$. Similar relations hold for Bob's measurement station (with a replaced by b and A by B).

Since the delay is local, one could think that this should allow the violation of the Bell's inequality. There is simply no physical mechanism for the remote phase shift to influence the local delay. However, for a coincidence to occur, Bob's delay needs to coincide with Alice's one, and Bob's delay is controlled by Bob's phase shift, remotely from the point of view of Alice. This constitutes a coincidence loophole for the Bell inequality

[50], somewhat similar to a detection loophole with 50% detection efficiency, but much worse since it is present even when using loss-free equipment, therefore introducing an unavoidable intrinsic loophole in the setup.

Quantum Mechanics provides the probabilities $p(a,b|\varphi_A,\varphi_B)$ for photon detections that occur within a narrow coincidence window Δw around the central time-slot t_0 for each pair of detectors a,b. The probabilities $p(a,b|\varphi_A,\varphi_B)$ depend on the initial state $|\Phi^+\rangle$ and on the local phase shifts φ_A, φ_B introduced by the measurement stations and are given, according to (1.8), by

$$p(a,b|\varphi_A,\varphi_B) = \langle\Phi^+|\hat{P}_{a|\varphi_A}\otimes\hat{P}_{b|\varphi_B}|\Phi^+\rangle = \frac{1}{4}[1+ab\mathcal{V}\cos(\varphi_A+\varphi_B)]\ , \tag{3.7}$$

where $\mathcal{V}$ is the visibility of the two-photon interference. Hence, in this case, the maximum value of the S-parameter introduced in (1.47) is equal to

$$S_{\max} = 2\sqrt{2}\mathcal{V} \tag{3.8}$$

if the local delays are $\varphi_A \in \{-\pi/4,\pi/4\}$ and $\varphi_B \in \{0,\pi/2\}$. Thus, the CHSH Bell-inequality *seems* to be violated if $\mathcal{V} > 1/\sqrt{2} \approx 0.71$. Actually, the post-selection introduces a serious loophole invalidating the expected violation of the Bell-CHSH inequality, as discussed above.

It is worth noticing that if *no* post-selection is applied in the passive time-bin scheme, for example by taking a wide coincidence window Δw comprising the three-peak profile, then the CHSH inequality does hold, and could in principle be violated. However, in this case Alice's measurement station implements the POVM given by $\{\hat{\Gamma}_{a|\varphi_A}\}$ where

$$\hat{\Gamma}_{a|\varphi_A} = \frac{1}{4}\mathbb{1} + \frac{1}{2}\hat{P}_{a|\varphi_A} \tag{3.9}$$

with the identity $\mathbb{1} = |S\rangle\langle S| + |L\rangle\langle L|$ (and similar relations hold for Bob). Thus, with no post-selection, the quantum probabilities $p(a,b|\varphi_A,\varphi_B)$ for photon detections at the two stations lead to a maximum value for the S-parameter that can be written as $S_{\max} = 2\sqrt{2}\mathcal{V}'$, with the overall three-peak visibility $\mathcal{V}' = \mathcal{V}/4$ and the CHSH inequality cannot be violated even with perfect two-photon (post-selected) visibility $\mathcal{V} = 1$.

On the other hand, a proper violation can be achieved with our source, that is an active time-bin scheme (see Figure 3.1**b**). We replaced the first passive beam-splitter of the measurement interferometer with an additional balanced interferometer, like the one in Figure 2.2, acting as a fast optical switch, which allows the measurement interferometer to recombine the $|S\rangle$ and $|L\rangle$ pulses, making them indistinguishable.

In this way, contrary to the passive time-bin scheme which recombines the two temporal modes in a probabilistic manner, our scheme deterministically compensates for the delay Δt and no detections are discarded. Indeed, by imposing the phases φ_S and $\varphi_L = \varphi_S - \pi$

on the $|S\rangle$ and $|L\rangle$ pulses respectively, the balanced interferometer determines the path they will take in the measurement one, as sketched in Figure 3.2**a**.

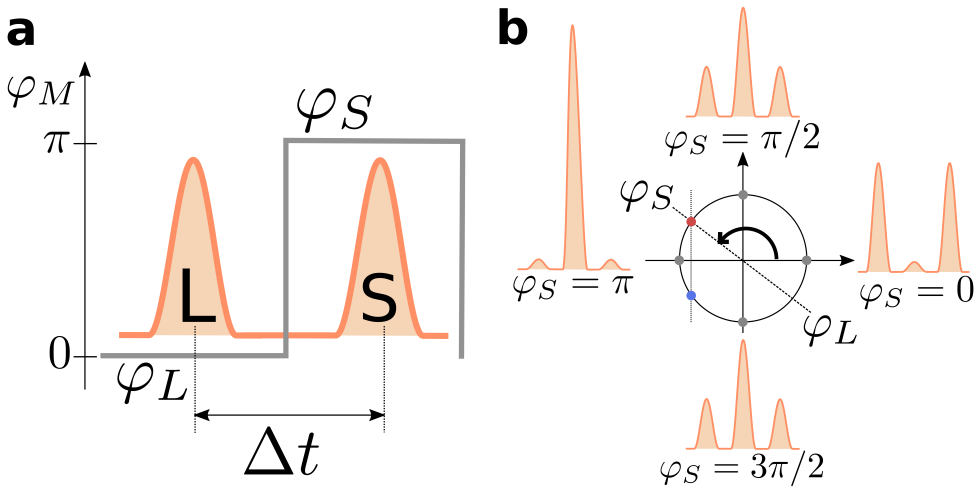

Figure 3.2: Functioning of the active time-bin scheme. **(a)** In a balanced Mach-Zehnder interferometer, the relative phase φ_M sensed by a travelling pulse determines the output port it will exit at with probabilities $\cos^2(\varphi_M/2)$ and $\sin^2(\varphi_M/2)$. By using a fast modulator, it is possible to impose the different phase-shifts φ_S and φ_L to the the $|S\rangle$ and $|L\rangle$ photons while they are travelling along the balanced MZI. By fixing $\varphi_S = \pi$ and $\varphi_L = 0$, it is possible to temporally recombine $|S\rangle$ and $|L\rangle$ pulses, making them indistinguishable. **(b)** The detection pattern at the output ports depends on the values φ_S and $\varphi_L = \varphi_S - \pi$. If $\varphi_S = \pi$, all detection events occur in the central time-slot, whereas if $\varphi_S = 0$ they are present only in the lateral time-slots. Any other detection histogram can be obtained with two different φ_S values, one with $\varphi_S < \pi$ (red dot) and the other with $\varphi_S > \pi$ (blue dot). For example, $\varphi_S = \pi/2$ and $\varphi_S = 3\pi/2$ have the same click distribution.

At each detector, we expect a detection pattern that depends on the value of φ_S, as shown in Figure 3.2**a**. From a formal point of view, in the active scheme Alice's measurement station implements the POVM $\{\hat{\Pi}_{a|\varphi_A}\}$, where

$$\hat{\Pi}_{a|\varphi_A} = \frac{1}{2}\left(\cos^2\frac{\varphi_S}{2}|S\rangle\langle S| + \sin^2\frac{\varphi_L}{2}|L\rangle\langle L|\right) + |\chi_a^{\varphi_A}\rangle\langle\chi_a^{\varphi_A}| \tag{3.10}$$

with

$$|\chi_a^{\varphi_A}\rangle = \frac{1}{\sqrt{2}}\left(ie^{-i\frac{\varphi_S}{2}}\sin\frac{\varphi_S}{2}|S\rangle + ae^{i(\varphi_A-\frac{\varphi_L}{2})}\cos\frac{\varphi_L}{2}|L\rangle\right), \tag{3.11}$$

assuming that the phase difference between the transmitted and reflected mode by a beam splitter is $e^{i\pi/2} = i$ as usual. If $\varphi_L = \varphi_S - \pi$, the POVM in (3.10) reduces to

$$\hat{\Pi}_{a|\varphi_A} = \frac{1}{2}\cos^2\left(\frac{\varphi_S}{2}\right)\mathbb{1} + \sin^2\left(\frac{\varphi_S}{2}\right)\hat{P}_{a|\varphi_A}. \tag{3.12}$$

Then, if Alice sets the phase $\varphi_S = \pi$ (and thus $\varphi_L = 0$), $\hat{\Pi}_{a|\varphi_A}$ results formally equal to $\hat{P}_{a|\varphi_A}$, that is

$$\hat{\Pi}_{a|\varphi_A} \xrightarrow{\varphi_S=\pi} \hat{P}_{a|\varphi_A}, \tag{3.13}$$

and her station actually projects onto the state $|\psi_a^{\varphi_A}\rangle$, with no post-selection procedure. Indeed, in the detection pattern the lateral peaks "disappear", as shown in Figure 3.2**b**

and it is not necessary to discard any data. Hence, the violation of Bell-CHSH inequality expected from our scheme is free of the post-selection loophole.

3.3 Implementation of the source

3.3.1 The optical setup

We implemented our active time-bin scheme by using the experimental setup sketched in Figure 3.3. A mode-locking laser (MIRA by Coherent) produced a pulse train with wavelength centered around 808 nm, 76 MHz of repetition rate and ∼150 fs of pulse duration. This beam is used to pump a second-harmonic-generation (SHG) [14] crystal which generates coherent pulses of light up-converted to $\lambda_p = 404$ nm. Each of the obtained pulses passes through a free-space unbalanced Michelson interferometer (that is the pump-interferometer in the actual implementation) which produces a coherent state in two temporal modes. The imbalance $\Delta l = L - S$ between the two arms is about 90 cm, corresponding to a temporal imbalance $\Delta t = \Delta l / c \approx 3$ ns (with c the speed of light in vacuum), much greater than the coherence time of the pulses. Then, the pulses pump a 2-mm long BBO crystal to produce the (degenerate) entangled photon state via Type-II SPDC at wavelength $2\lambda_p = 808$ nm, as discussed in Section 2.3.1.

The two photons are sent to Alice' and Bob's terminals after being spectrally filtered (3 nm bandwidth) and collected by two single-mode optical fibers. Each station is composed

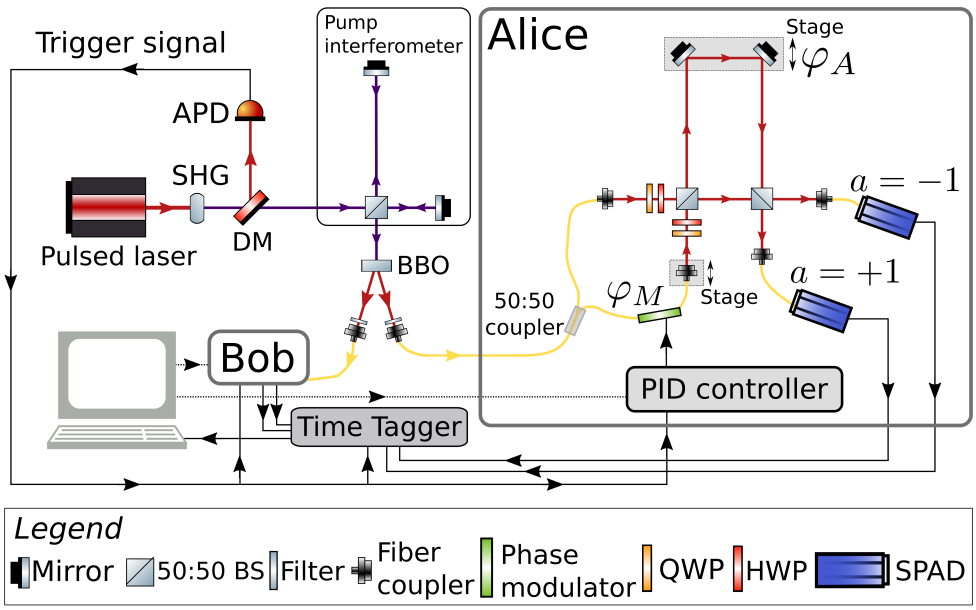

Figure 3.3: Experimental setup to implement the active time-bin source. Bob's measurement station is analogue to Alice's one. APD: analog-photo-detector; DM: dichroic mirror.

of two Mach-Zehnder interferometers (MZI), a balanced one and an unbalanced one. The balanced MZI is composed by a 50:50 fiber coupler which defines the two arms of the interferometer. To guarantee the zero imbalance of this MZI, a nanometric stage is placed in one of the two arms.

The balanced MZI works as a fast optical switch, since there is a fast (∼GHz bandwidth) phase-modulator in one of its arms. The modulation voltage is set to V_π such that $\varphi_S - \varphi_L = \pi$, while the DC bias of the phase-modulator is driven by an external *proportional-integral-derivative* (PID) controller, that is responsible of locking the phase φ_S to π. The complete operating principle of the PID controller is detailed in the following.

The two arms of the balanced MZI are recombined at a 50:50 free-space beam splitter (BS) after been optimized for polarization rotations. This BS begins the unbalanced MZI whose imbalance is equal to that of the pump-interferometer (within the coherence time ∼200 μs of the photons). The two mirrors of the long arm of the unbalanced MZI are placed on a nanometric piezoelectric stage to both guarantee the required imbalance Δt and introduce the local phase shift φ_A and φ_B to realize the Bell test. At the two output ports of the measurement stations we used two avalanche single photon detectors (SPADs, ∼50% detection efficiency), labelled as $a = \pm 1$ and $b = \pm 1$. The detection events are then time-tagged by a time-to-digital converter (quTau time tagger from quTools) with 81 ps resolution and the data are stored in a computer.

3.3.2 Functioning of the PID controller

In our experiment we have to drive the phase φ_M introduced by the phase-modulator (PM) in the balanced MZI to make the photons take a precise path in the subsequent MZI. To realize this, we implemented the PID controller that is sketched in Figure 3.4.

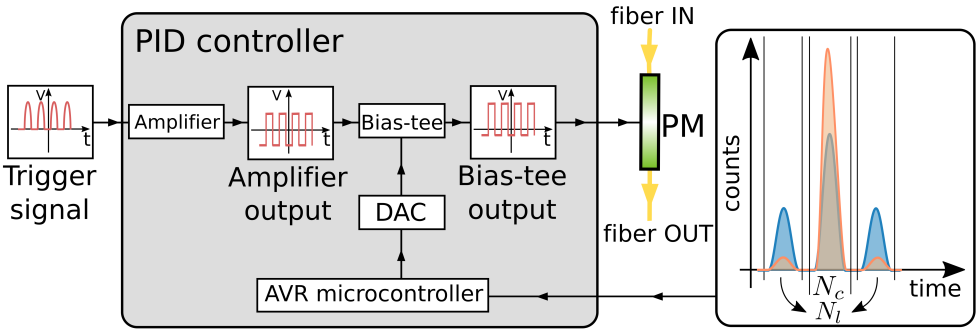

Figure 3.4: Detailed scheme of the PID controller.

First, we synchronized the phase transition with the pump-pulses that produce the

photon pair. This was performed by a fast analog-photo-diode (APD) that collected the 808 nm pulsed beam (after being separated with a dichroic mirror (DM) from the 404 nm pulse train produced by the SHG stage, see Figure 3.3) and produced an electric signal synchronized with the optical pulses. This signal was split in two: one was then collected by the time-tagger for timing purposes and the other one was sent to the PID controller.

The first stage of the PID controller was an amplifier (iXblue) which produces a square wave with fixed amplitude centered around 0 V. The amplitude V_π of this wave set the strength $\Delta\varphi = \varphi_S - \varphi_L = \pi$ of the transition introduced by the phase-modulator. The raise time of the square wave was less than 2.5 ns to guarantee that the π-transition occured within the short-long temporal separation Δt.

The absolute value of the phase φ_S of the balanced MZI was perturbed by temperature fluctuations and vibrations due to the environment. In order to correctly implement our scheme, we had to compensate this phase fluctuation (which occured in the order of tens of seconds), by locking the value of φ_S to π.

To perform this locking, the second stage of the PID controller was given by a bias-tee (MiniCircuits) which compensated the intrinsic phase shift of the balanced MZI by changing the offset voltage V_{bias} of the square wave produced by the amplifier. This was obtained by the combined action of an AVR micro-controller (Arduino) and a digital-to-analog converter (DAC) by maximizing the extinction ratio R between the central and the lateral peaks

$$R = \frac{N_c - N_l}{N_c + N_l} \tag{3.14}$$

where N_c were the counts associated to the central peak and N_l were all the counts in the lateral ones recorded by one of the two detectors of the measurement station. All the counts in each detector were estimated in real-time by looking at the raw data collected by the time-tagger, and they produced the detection histogram sketched in the inset of Figure 3.4, which corresponds to the real detection histograms presented in Figure 3.6.

To successfully lock φ_S to π the PID controller had to first evaluate its real-time value by observing the detection histogram and computing R. Unfortunately, there is no one-to-one correspondence between the extinction ratio and the phase φ_S. Indeed, for each possible value of R there exist two possible values for φ_S that reproduce the observed histograms (with the exception of 0 and π), as shown in Figure 3.2**b**. Therefore, we included an additional information that allowed us to distinguish between the two possible phase values. This information was given by the derivative of the extinction ratio. If an increase of the phase value caused an increase of the ratio, we chose the phase $0 < \varphi_S < \pi$ (requiring further increase to reach π). Otherwise, we chose the phase $\pi < \varphi_S < 2\pi$ (requiring a

decrease to reach π). Since the PID required an error function that is equal to zero when the objective was reached, we chose the function

$$E_{\varphi_S} = \mathrm{sgn}\left(\frac{dR}{d\varphi_S}\right)\frac{N_l}{N_c}\,, \tag{3.15}$$

which guaranteed that the PID's objective is both to lock the value of φ_S to π and to identify correctly the value of the phase, since the symmetry between the two possible phase values was broken by the sign of the derivative of the extinction ratio.

We show in Figure 3.5 an example of the ratio R as a function of the acquisition time during the Bell data acquisition (see the next section presenting the results of the Bell test).

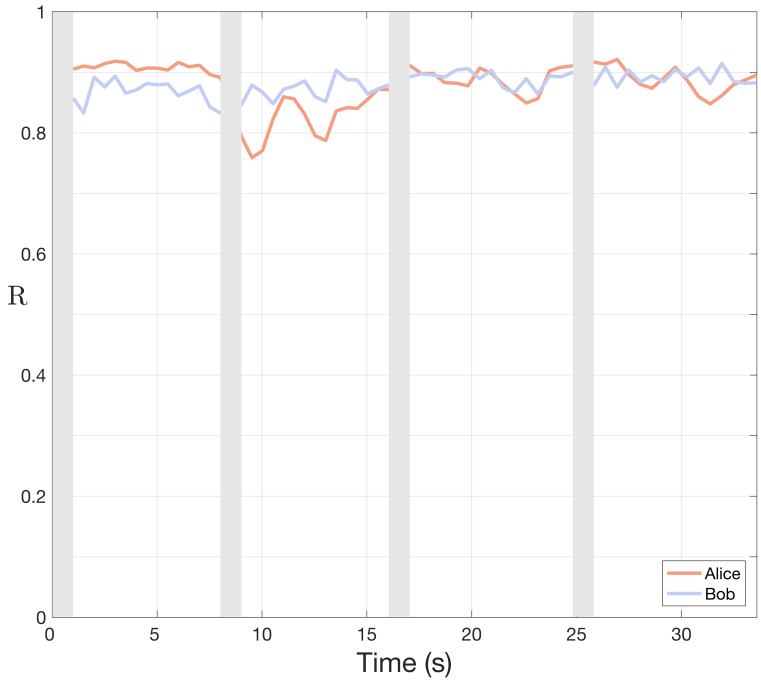

Figure 3.5: Extinction ratio R as a function of the acquisition time during the Bell data acquisition. We plot the detector pair $(a,b) = (+1,+1)$ for Alice and Bob.

3.4 Results of the Bell test

With the setup shown in Figure 3.3, we performed the time-bin Bell-test with three different schemes:

i) the *passive time-bin with post-selection*;

ii) the *passive time-bin with no post-selection*;

iii) the *active time-bin with no post-selection*.

To realize i), we bypassed the balanced MZI in each of the measurement stations, hence obtaining the passive time-bin configuration of Figure 3.1**a**. By choosing a coincidence window $\Delta w \approx 2.4$ ns and by post-selecting the coincident events that occurred only in the central time-slot, Alice (Bob) implemented the projective measurement given by $\hat{P}_{a|\varphi_A}$ ($\hat{P}_{b|\varphi_B}$) and the expected CHSH violation is affected by the post-selection loophole. To realize ii), we used the same configuration as in i), but we did not discard any data by choosing a coincidence window $\Delta w \approx 8.1$ ns, which corresponds to the total width of the three peak-profile in the detections (see Figure 3.6). In this case, Alice (Bob) implemented the POVM given by $\hat{\Gamma}_{a|\varphi_A}$ ($\hat{\Gamma}_{b|\varphi_B}$) and no Bell-CHSH violation is expected.

To implement iii), we exploited the balanced MZI in each station and we used the PID controller to lock the phase φ_S and φ_L to π and 0 respectively, independently at each terminal. We did not discard any data by choosing a large coincidence window as in ii), but, in this case, the Bell-CHSH inequality is directly applicable, since Alice (and Bob) implemented the POVM given in (3.12) with $\varphi_S = \pi$. The expected Bell-CHSH violation is now free of the post-selection loophole.

We show in Figure 3.6 a typical detection histogram obtained with one of the four detectors during the data acquisition (the results are similar for all the detectors). In the case of TB schemes i) and ii), since the balanced MZI is bypassed, we obtained the expected three-peak profile (blue histogram). On the other hand, in our active time-bin scheme iii), the PID controller makes the lateral peaks disappear, as shown by the orange detections histogram. This guarantees the correct functioning of the PID controller, whose details were described above. It is worth noticing that the whole three-peak profile is within the chosen coincidence window $\Delta w = 8.1$ ns, thus guaranteeing that no data is discarded.

To realize each of the Bell-tests described above, we first calibrated the shifts to be introduced by the nanometric stages in Alice' and Bob's unbalanced MZIs. This is obtained by scanning the coincidence rate for a pair of detector by moving Bob' stage while Alice's one is fixed. From the sinusoidal pattern obtained in such a way, we estimated the experimental visibility $\mathcal{V}_{\text{exp}}$ for each scheme. As an example, we show in Figure 3.7 the calibration fit obtained to realize the Bell test iii), which gives a visibility $\mathcal{V}_{\text{exp}} = 0.89 \pm 0.03$. Then, we imposed the shifts (φ_A, φ_B) needed to obtain the maximal violation of the Bell inequality (as described above) and acquired the data for sufficient time to achieve significant statistics.

The results obtained for each of the three schemes described above are represented in Table 3.1. As expected, violation of the Bell-CHSH inequality was obtained with the first and the third scheme with clear statistical evidence, but only the third one is not affected

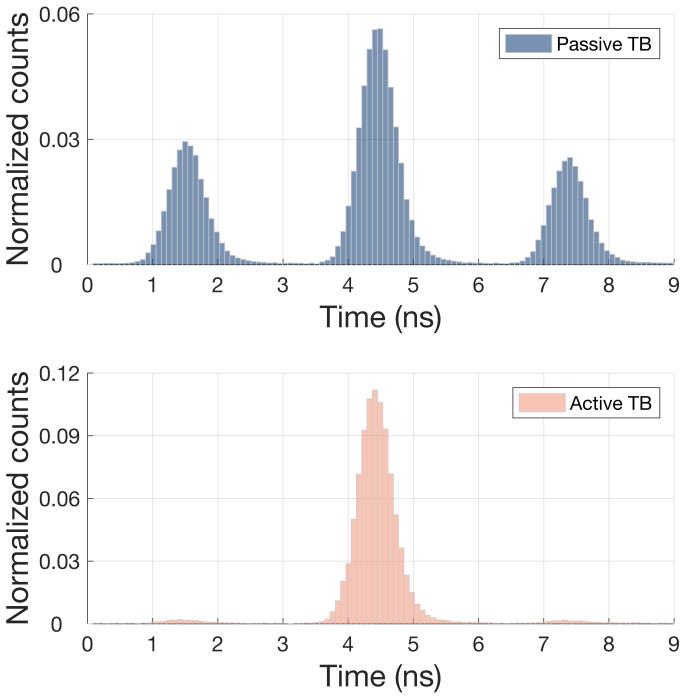

Figure 3.6: Typical detection histograms obtained during data acquisition. The two histograms represent all the raw detections collected by one of the four detectors during the data acquisition. The blue histogram shows a typical detection pattern obtained with the passive time-bin scheme, in which the three-peak profile is observed. The orange histogram shows the detection pattern obtained with the active time-bin scheme: the PID controller is able to lock φ_S to π and φ_L to 0, thus making the lateral peak disappear, allowing us to realize a time-bin Bell-test free of the post-selection loophole. The counts are normalized to fairly compare the two histograms.

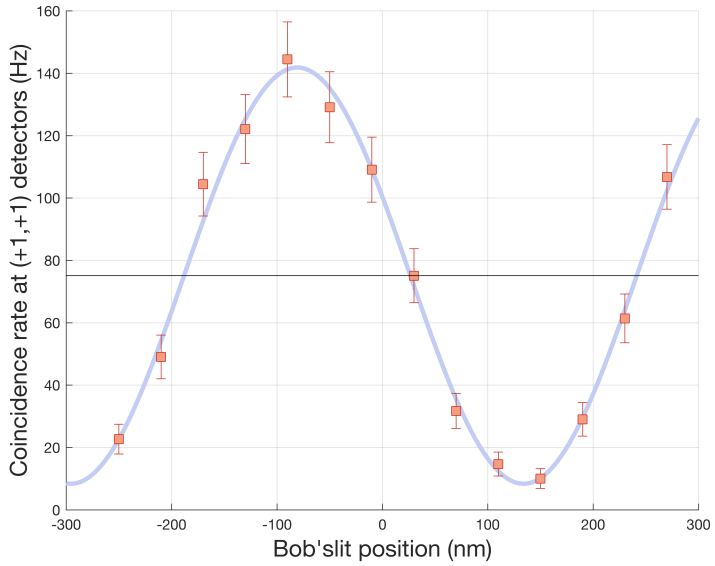

Figure 3.7: Calibration fit obtained to realize the Bell test iii). We plot the detector pair $(a, b) = (+1, +1)$.

by the post-selection loophole. The minor violation obtained in iii) is due to imperfection in the balanced MZI alignment and in the locking procedure occurring during data

acquisitions needed to experimentally estimate the S-parameter S_{exp}. It is worth stressing that any imperfection in the locking mechanism setting $\varphi_S = \pi$ corresponds to an effective lower visibility, but it does not introduce any loophole in the Bell inequality.

Time-bin scheme	Δw	Post-Selection Loophole	$\mathcal{V}_{exp}$	S_{exp}	SD
i) passive	2.4 ns	Yes	0.95 ± 0.05	2.58 ± 0.03	18.3
ii) passive	8.1 ns	No	0.23 ± 0.02	0.67 ± 0.02	—
iii) active	8.1 ns	No	0.89 ± 0.03	2.30 ± 0.03	9.3

Table 3.1: Main results. SD refers to Standard Deviation of the Bell-CHSH violation.

3.5 Discussion and future perspectives

Time-bin encoding is a valid resource for both performing fundamental tests of quantum mechanics [51] and distributing entanglement over long distances [31]. However, all the time-bin entanglement realizations performed so far were affected by the post-selection loophole, which makes this technique unsuitable for quantum information protocols. A possible way to overcome this problem requires to violate the so-called "chained" Bell-inequalities [52], but the needed two-photon visibility is considerably higher ($\gtrsim 0.94$ [41]) than the one of the Bell-CHSH inequality ($\gtrsim 0.71$). Even if such a high visibility is achievable with time-bin entanglement, as shown in [53], our scheme clearly relaxes this requirement, since the Bell-CHSH inequality is directly applicable.

Our work is the first implementation of a genuine time-bin entanglement source, and represents a crucial step towards its exploitation for fundamental tests of physics and the realization of the quantum internet [54]. In fact, our scheme can be realized using only commercial off-the-shelf fiber components and, since its stability does not depend on the distance between Alice and Bob, it is easier to be implemented with respect to the hug configuration [45]. Furthermore, as long as both the π-phase transition imposed by the modulator and the detectors jitter are shorter than the imbalance Δt, it is possible to shorten it, rendering it compatible with today's photonic integrated technologies [55, 56]. Finally, our work makes time-bin entanglement a viable technique to obtain a loophole-free Bell violation, that is the enabling ingredient of any device-independent protocol [57, 58, 59, 60].

Chapter 4

Space Quantum Communications at MLRO

The recent development of quantum communications, which could guarantee unconditional security for communications at the global scale in the next future, has stimulated a great progress in satellite quantum technologies. Nowadays, such technologies are mature enough to support the realization of experiments testing the foundations of quantum theory at unprecedented scales and in the unexplored Space scenario. Space-based Quantum Optics experiments could explore the boundaries and extend the validity limits of the quantum theory, as well as provide new insights to investigate phenomena where gravity affects quantum objects.

In this chapter we will present the motivations behind Space quantum communications and the state-of-the-art worldwide, then we will review our last experiments performed in collaboration with the Matera Laser Ranging Observatory of the Italian Space Agency. Some contents of this chapter are part of our works [61, 62, 63].

The MLRO telescope tracking SLR satellites (photo by Marco Tomasin).

4.1 Introduction

4.1.1 Why Space Quantum Communications?

Quantum Mechanics, the physical theory that has revolutionized our understanding of the universe since its conception in the early 20th century, is now fostering the development of new technologies that are inspired by and exploit its very own basic principles. The development of such new technologies can foster the implementation of fundamental tests of Quantum Mechanics in radically new scenarios. Such tests could not only corroborate the validity of quantum predictions at unprecedented scales, many of which are simply inaccessible in the laboratories on ground, but, most importantly, could explore the boundaries of the theory itself.

One of such scenarios is certainly given by Space. Driven by the increasing interest in quantum communications [33], that are the transfer of quantum states from one location to another distant one, the development of satellite quantum technologies could encourage the realization of many experiments aimed at testing the foundations of the quantum theory in the yet unexplored relativistic regimes, where gravitational effects might play a role [64, 65].

The goal of quantum communications is to outperform its classical counterpart in a number of communication primitives such as privacy, secrecy and authentication. Quantum Key Distribution (QKD) [33, 15], for example, allows two parties to distill a common key with provable unconditional security, a level of secrecy that is simply not achievable by classical communication, which must accept computational hardness assumptions, many of which might no longer be valid as quantum computers become more mature [66]. Furthermore, quantum communications are the backbone for quantum Internet [54], a network of new devices that will revolutionize the way we communicate and perform computational tasks.

Despite the many advances of fiber-based quantum communications, a real global-scale quantum communications network cannot be deployed using only fiber-optics links. In fact, the signal attenuation and the polarization-preservation issues render such links quite problematic and limit their lengths to few hundreds of kilometers [67]. A possible workaround could be represented by quantum repeaters [68], but the most promising solution to this problem is the use of Space technologies to develop satellite quantum links [69, 70]. Such channels could potentially lead to a global quantum communication network since they could connect any two points on Earth's surface with reduced propagation losses if compared with terrestrial channels, even in the presence of

noise [71]. The importance of such satellite quantum links is attested in several mission proposals [72, 73, 74, 75].

Recently, several experimental efforts have been realized, demonstrating not only the feasibility, but also the implementation of satellite-to-ground links for quantum communications. Among the others that will be reviewed in the following section, in August 2016 the Chinese Academy of Sciences launched *Micius*, a satellite dedicated to quantum communications, with which the Chinese collaboration implemented fundamental tests in space [76], quantum communication protocols [77], as well as demonstrations of secure communications by means of QKD [78, 79]. The development of such satellite quantum technologies fosters the implementation of fundamental-like tests in Space, as experimentally shown in [76] and in [80], which will be presented in details in Chapter 6. These tests can range from the verification of the validity of the postulates and predictions of Quantum Mechanics in micro-gravity environments to experiments that might confirm or give insights on the theories that could unify quantum theory with gravitation.

4.1.2 State-of-the-art

The interest in developing satellite quantum technologies is shared among several research groups all around the globe. In recent years, several experimental efforts have been made and important results have been obtained, highlighting the advantages and disadvantages of the different available encodings, as collected in the reviews [81, 82, 62].

The polarization encoding presented in Section 2.2.2 is a suitable way for exchanging quantum information through free-space, since the atmosphere does not significantly affect the polarization state of light, nor does the Faraday effect [14] due to the Earth's magnetic field [83]. Furthermore, since polarization encoding is the simplest physical implementation of the qubit, it is a natural candidate for satellite quantum communications over long distances. Working upon such bases, in 2015, our study by Vallone *et al.* in [84] experimentally demonstrated the preservation of single photon polarization over a satellite-to-ground channel exploiting the two-way scheme that we will present in the next section.

Such a result proved that the faithful transmission of different polarization qubits can be obtained in several conditions and satellite orbits. Furthermore, it demonstrated the feasibility of QKD via the BB84 protocol [85] along a satellite-to-ground channel. These results were then corroborated by the National Institute of Information and Communications Technology (NICT) in Japan, which launched a Low-Earth-Orbit satellite in 2014 carrying a lasercom terminal (SOTA), designed for in-orbit technological demonstra-

tions [86]. In 2017 Takenaka *et al.*, reported on a quantum-limited polarization encoded communication between SOTA and a ground station [87].

In 2017, as reported by Liao *et al.* [78], the decoy-state QKD protocol [88] was successfully implemented between the Micius satellite and a ground station in China with a kHz key-rate exploiting polarization encoding. Furthermore, still in 2017, Ren *et al.* reported on the successful implementation of a ground-to-satellite quantum teleportation protocol [77]. A polarization-encoded photon was generated at the ground station together with a polarization entangled photon pair. The polarization-encoded photon and one photon of the entangled pair were then projected into a Bell-state while the other photon from the entangled pair was directed towards Micius, where it was detected with a fidelity of 0.80, well above the classical limit of 2/3. Such experiments demonstrate that the technological advances in Quantum Optics and satellite technologies are mature enough for a global-scale quantum communication network that exploits the single photon polarization degree of freedom as encoding.

Furthermore, in September 2017 the Chinese group and the University of Vienna realized the first intercontinental video-call encrypted via satellite QKD [79]. The Micius satellite exchanged the cryptographic key with two ground stations, the first in Xinglong (near Beijing, China) and the second one in Graz (near Vienna, Austria), allowing the realization of such call at the intercontinental distance of 7 600 kilometers.

Then, Yin *et al.* reported on the long-distance distribution of entangled particles to two distinct locations separated by 1 203 kilometers via two satellite-to-ground downlinks [76]. An unprecedented Bell test was performed on these particles obtaining a S-parameter of 2.37 ± 0.09, violating the local-hidden variable bound (1.48) under strict locality conditions.

Another possible encoding for space quantum communications is given by the temporal degree of freedom of photons, i.e. the time-bin encoding described in Section 2.2.3. In 2016, we reported the observation of single-photon interference of photons that had traveled a path length of up to 5 000 km [89]. This experiment is described in details in Chapter 5. By combining polarization and time-bin we then implemented in 2017 a satellite version of the famous *Wheeler's delayed-choice experiment* [80], which is described in details in Chapter 6.

Efforts to extend the range available for discrete-variable, i.e. polarization and time-bin encoding, satellite quantum communications have also been made. Our group in 2016 reported in Dequal *et al.* [90] on the realization of a single-photon exchange from a Medium Earth orbit (MEO) satellite at more than 7 000 km of slant distance to the ground station. Then, in April 2018, the first experimental exchange of single photons

from a Global Navigation Satellite System (GNSS) terminal at a slant distance of 20 000 kilometers was reported in our study by Calderaro *et al.* [63]. This latter experiment is discussed in more details in Section 4.3.

Alternatives to the discrete-variables encodings are also under investigation. For example, encoding information in the quadratures of quantum states of light, i.e. continuous variables [12], can also be a possibility for satellite quantum communications. This type of encoding is promising specially due to the high transmission rates it could achieve. In 2017, Günther *et al.* reported on the quantum-limited coherent measurement of optical signals sent by a geostationary satellite to a ground station [91]. These results show that future technological developments could render homodyne-detection based quantum communication protocols feasible also from Space.

4.2 Quantum Optics experiments at MLRO

4.2.1 Simulating a single photon source in orbit

Even if there was no active source dedicated to Space quantum communications on a satellite until the launch of Micius satellite, the quantum transmission of single photons from satellite to ground was already experimentally investigated by our group by exploiting the *two-way scheme* sketched in Figure 4.1, that was originally proposed in [92] and then improved in [84]. Our scheme takes advantages on *Satellite Laser Ranging* (SLR) technique, which is typically used for geodynamical studies (crustal dynamics, polar motion, time-varying geopotential monitoring) [93] by means of a series of measurements of the *round trip time* (rtt) of optical laser pulses that propagate from a station on the Earth, are then retroreflected at the satellite and are finally detected at the ground station. From the measure of the flying time rtt of the pulse it is possible to measure the distance of the satellite with great resolution. Laser ranging activities are organized under the International Laser Ranging Service (ILRS) [94], which provides global satellite and lunar laser ranging data and their derived products.

We developed a technique to mimic a qubit source in Space by exploiting the *corner cube retroreflectors* (CCRs) mounted on the satellites exploited by ILRS. The common idea of our experiments is to send a bright laser pulse towards a satellite which then reflects it back to the ground station, when it is collected as a weak-coherent pulse. The ground station used in our experiments is the Matera Laser Ranging Observatory (MLRO) of the Italian Space Agency (ASI), which is a SLR station which can reach sub-millimeter accuracy in the estimation of the satellite distance. The MLRO telescope automatically

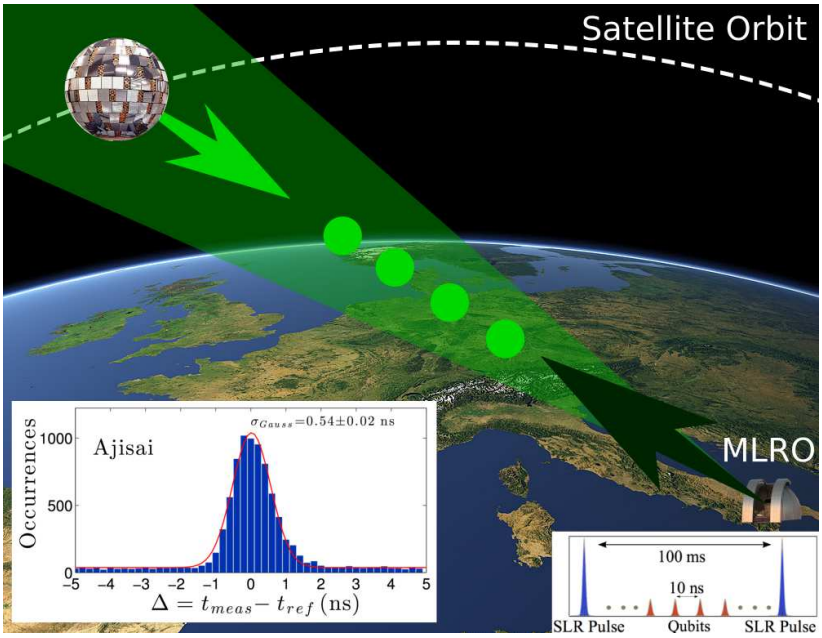

Figure 4.1: *General scheme of quantum satellite communication experiments realized at MLRO.* A 100-MHz train of qubit pulses is directed towards a satellite equipped with corner-cube retroreflectors, which reflect the beam back to the ground station. Such a scheme has allowed the study of polarization encoding [84] and time-bin encoding [89] for satellite quantum communications as well as the realization of the satellite version of Wheeler's delayed choice experiment [80] and the investigation of single-photon exchange with terminals in different orbits [90, 63]. In the left inset a typical detection histogram is observed where the quantum signal is well distinct from the background noise. In the right inset the timing and synchronization of the qubit train with respect to the the strong SLR pulses is observed. SLR pulses are required to determine the expected time of arrival of the retroreflected qubit pulses as well as the calculation of effects dependent on the satellite orbit.

track ILRS terminals, following a pre-set schedule, by using the predictions of the orbits provided by ILRS. Real-time corrections to the pre-set trajectory are imposed manually by the MLRO operators.

Due to the losses in the propagation, the intensity is reduced and we set up the energy of the upgoing pulse to have a mean photon number per pulse close to one when it is reflected back at the satellite. In this way, we are are able to simulate a weak-coherent photon source on the satellite. The retroreflected beam is finally collected at the MLRO ground station by using single-photon detectors with a temporal accuracy below one nanosecond.

This technique requires a great synchronization between the SLR pulses and the qubit ones, which have different repetition rate and energy. Our scheme allows to obtain the histogram of the single photon detections as a function of the difference between the measured time of arrival of the photons t_{meas} and the expected one t_{ref}, as you can see in the left inset of Figure 4.1. We applied this general idea to satellites in different orbits (LEO, Low Earth Orbit [84, 89] and MEO, Medium Earth Orbit [90, 63]) and we exploited different degrees of freedom for quantum information encoding, as polarization [84] and temporal modes of single photons [89]. The passage time of the used satellites depend on the actual

orbit they follow, ranging from few minutes in the case of LEO terminals to quite an hour in the case of MEO.

At the heart of our experiments there is the simulation of the photon qubit source on the satellite. For this reason, we have to be sure about the mean photon number per pulse reflected at the satellite. We use a model coming from geo-dynamics studies due to Degnan [95], who addressed the uplink and downlink attenuations in terms of physical parameters like the satellite distance, the atmospheric transmittivity, and other parameters which depend on the specific satellite. By knowing the generation and detection photon rate at the ground station, we can infer the mean photon number at the satellite and the measured return frequencies agree very well with the frequencies predicted by the model and so we can claim that we are mimicking a single photon source on the satellite.

4.2.2 Generation and detection of the SLR pulses

The experiments presented in this thesis were performed at MLRO observatory by using the two optical tables sketched in Figure 4.2, the *TX Table*, and Figure 4.4, the *RX Table*.

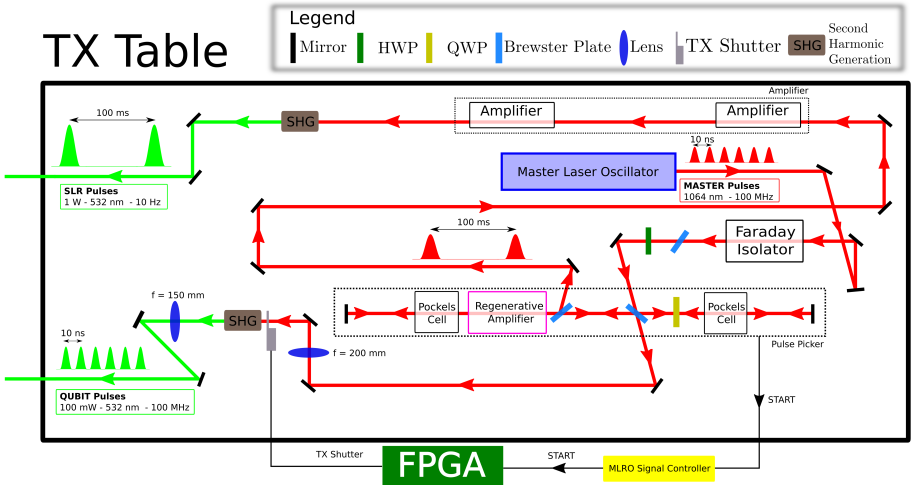

Figure 4.2: The TX Table at MLRO.

The TX Table is equipped with a mode-locking Nd:YVO_4 master laser oscillator, operating at 1064 nm with 100 MHz repetition rate and paced by an atomic clock. The SLR pulses (wavelenght, 532 nm; energy, ∼100 mJ; repetition rate, 10 Hz) are obtained by selecting one seed pulse every 10^7 with a pulse-picker, which is then amplified twice and up-converted via a second-harmonic-generation (SHG) stage.

The SLR pulses are sent to the targeted satellites equipped with CCRs by using the 1.5-m diffraction-limited Cassegrain telescope of MLRO after having passed the RX Table

and the Coudé path sketched in Figure 4.3.

Then, after the reflection by the orbiting terminals, the SLR pulses are collected by the same telescope and injected into the RX Table, where they are detected by a fast analog micro-channel plate detector (Hamamatsu R5916U-50). A dedicated time-tagger with picosecond accuracy recorded the start and stop signals generated by the pulse picker and the detector respectively. The single-shot measurement of the satellite distance is then estimated from the time-difference of these two signals, i.e. the round-trip-time rtt , with an error below 20 ps.

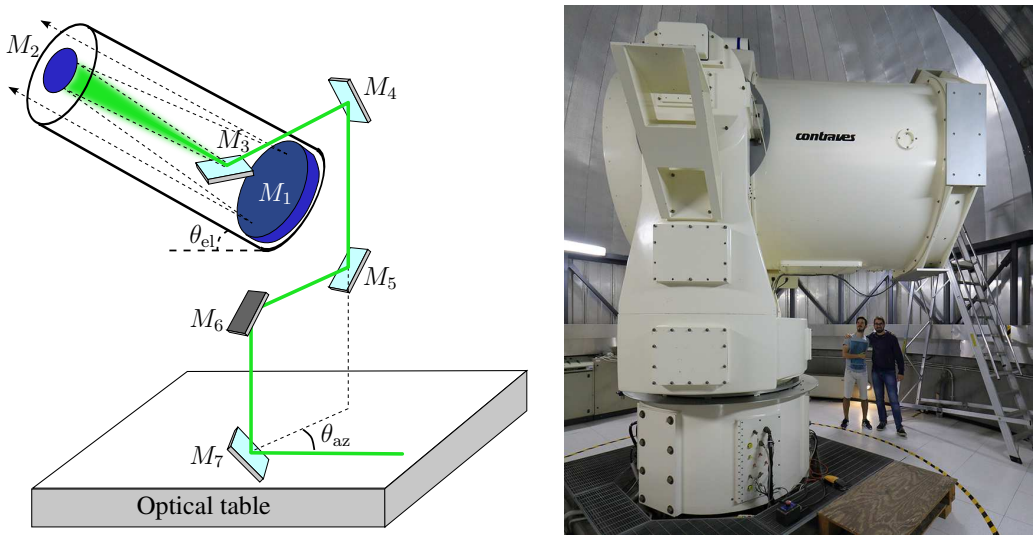

Figure 4.3: **(left panel)** The Coudé path of the MLRO telescope. **(right panel)** My colleague Luca Calderaro and I posing under the MLRO telescope.

4.2.3 Generation and detection of the qubit pulses

The setup dedicated to the realization of the Quantum Optics experiments in Space is implemented in parallel to the SLR system. The same laser oscillator is used to produce a 100-MHz pulse-train, the *qubit pulses*, with wavelength $\lambda = 532$ nm, $\sim$1 nJ of energy and $\sim$100 ps of pulse duration at full-width-half-maximum (FWHM), by exploiting a SHG process in a 50 mm long periodically poled lithium niobate (PPLN) non linear crystal from HC Photonics. The qubit pulses passes through a mechanical shutter, TX Shutter in the figure, which is used for timing purposes.

The qubit pulses now go to the RX Table, where they pass through a *Quantum Optics setup*, sketched by the gray box in Figure 4.4, which depends on the actual experiment to perform.

Afther this "black box" the qubit pulses, synchronized with the SLR pulse-train, are

combined with the outgoing SLR pulses by using a 50:50 beam splitter (BS) and the two light beams are sent together to the targeted satellites.

After the satellite retroreflection, the qubit pulses pass again through the Quantum Optics setup, from which they emerge to be detected. The receiving apparatus of the 100-MHz beam is usually comprised of a beam splitter to separate the outgoing and ingoing beam. The emerging beam, after passing the RX shutter, is directed to a free-space detection system, which depends on the experiment and it is usually comprised of a 3-nm FWHM spectral filter with transmission band centered at 532 nm, a focusing lens and one (or more) single photon detector (DET). We used single-photon photomultiplier tubes (PMT) with $\sim$ 10% of detection efficiency, 22 mm of active diameter by Hamamatsu Photonics (model: H7360-02) in [84, 80] and single photon avalanche diode (SPAD) with $\sim$ 50% of detection efficiency, 200 micron of active diameter by Micro-Photon-Devices (MPD) in [63].

The time-tag of arrival of the returning photons is recorded with ps resolution by a time-to-digital converter (time-tagger) which provides t_{meas}. In [89, 80] we used the quTau time-tagger, with 81 ps of resolution, and in [63] we used the quTag time-tagger, with 1 ps of resolution, both from quTools.

4.2.4 Timing and synchronization

We implemented a two-phase communication protocol to separate the transmitting and receiving phases by using two mechanical shutters, one on the TX Table and the other on the RX Table. We separated each 100-ms cycle between two subsequent SLR pulses in

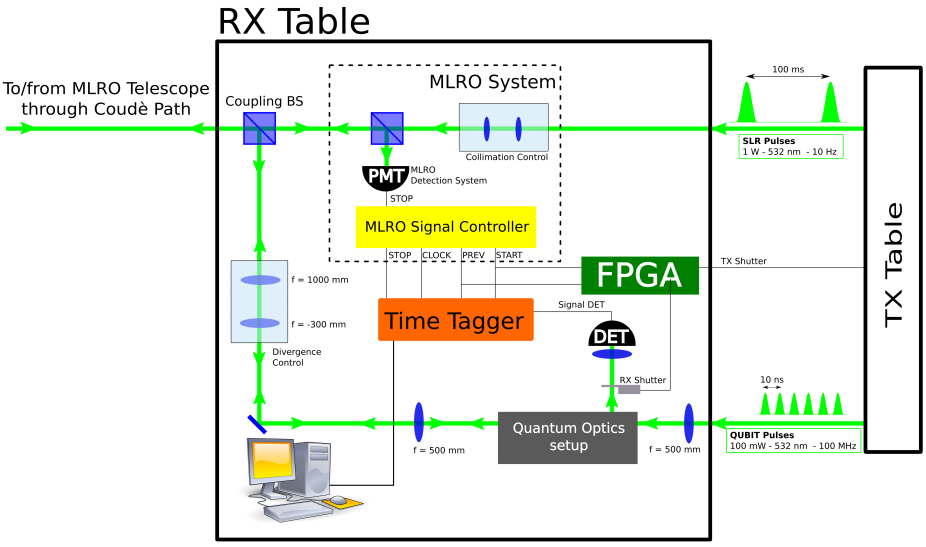

Figure 4.4: The RX Table at MLRO.

two periods by using such shutters, as sketched in Figure 4.5 In the first half of the 100-ms period, only the transmitting shutter (TX shutter) is open, while the receiving one (RX shutter) is closed. In the second half of the time slot, the TX shutter is closed while the RX shutter is open and the detectors can receive the photons coming from the satellite. Furthermore, since the shutters require a certain time to open and close completely, the effective detection time period is limited by the shutters transition time ($t_{\text{trans}} \sim 5$ ms). Hence, there exists a precise temporal window $\tau = \text{rtt} - t_{\text{trans}}$ where we expect to receive photons from the satellite. The value of τ depends on the actual rtt which is continuously changing along the satellite orbit.

Between two subsequent SLR pulses extracted by the pulse picker every $\Delta T = 100$ ms there are 10^7 qubit pulses separated by 10 ns. Hence, by dividing the time interval interval between two consecutive SLR pulses at the detection $\Delta T'$ in 10^7 equidistant subintervals, it is possible to estimate the expected arrival time of the qubit pulses t_{ref}, which has to be compared with the measured one t_{meas}. This technique automatically compensates for the variation of the round trip time duration due to the satellite motion (essentially Doppler effect, as described in the following chapter) and air refraction. With this technique, it is possible to obtain the histogram of the returns in the temporal window of 10 ns between two consecutive qubit pulses as a function of the temporal difference $\Delta = t_{\text{meas}} - t_{\text{ref}}$, as in the inset of Figure 4.1.

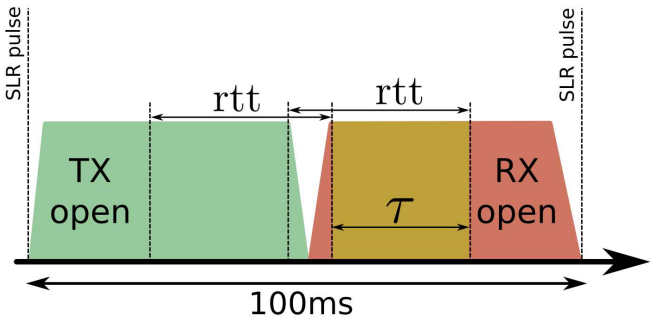

Figure 4.5: Two-phase communication protocol.

The first experiment in which the two-way scheme was exploited as described above was the one by Vallone *et al.* [84], in which, by exploiting orbiting satellites equipped with polarization-maintaining metallic CCRs, was possible to demonstrate that polarization encoding is a good choice for satellite Quantum Communications. By taking data from several satellites (namely Jason-2, Larets, Starlette, Stella), an average Quantum Bit Error Rate (QBER) of $4.6 \pm 0.8\%$ was obtained, demonstrating the feasibility of satellite QKD with polarization encoding.

4.2.5 Estimating the mean photon number per pulse at the satellite

A crucial parameter to be estimated in our experiments emulating a single photon source on a satellite is the mean photon number per pulse at the satellite reflection μ_{sat}, that we want to be of the order of one. μ_{sat} is estimated by dividing the the average number of photons per pulse detected at the receiver μ_{rx}, by the transmittivity of the channel knowing the mean number of photons per pulse transmitted from the ground μ_{tx}.

To predict the detected number of photons per pulse we use the *Degnan link-budget radar equation* [95]

$$\mu_{rx} = \mu_{tx}\eta_{tx}G_t\Sigma\left(\frac{1}{4\pi R^2}\right)^2 T_{atm}^2 A_{tel}\eta_{rx}\eta_{det}\,, \tag{4.1}$$

where μ_{tx} is the source mean photon per pulse, η_{tx} is the optical transmission efficiency, G_t is the transmission gain, Σ and R are the satellite cross-section and slant distance, T_{atm} is the atmospheric transmittivity, A_{tel} is the telescope area, η_{rx} is the optical receiving efficiency and η_{det} is the single photon detector efficiency. It is possible to factorize (4.1) into uplink and downlink contributions as

$$\text{uplink: } \mu_{sat} = \mu_{tx}\eta_{tx}G_t\rho A_{eff}\left(\frac{1}{4\pi R^2}\right)T_{atm}\,, \tag{4.2}$$

$$\text{downlink: } \mu_{rx} = \mu_{sat}G_{down}\left(\frac{1}{4\pi R^2}\right)T_{atm}A_{tel}\eta_{rx}\eta_{det}\,, \tag{4.3}$$

where we split the satellite cross-section according to $\Sigma = \rho A_{eff}G_{down}$ where ρ and A_{eff} correspond to the CCR reflectivity and to the effective satellite retroreflective area and they contribute to the uplink, while G_{down} expresses the effective downlink gain and so it contributes to the downlink term. Using these expressions it is possible to extrapolate the transmitter gain G_t and use it to predict the number of received photons to compare it with the measured one. Vallone *el al.* showed in [84] that the Degnan radar equation and equations (4.2)-(4.3) provide a precise fit for the measured counts, giving an accurate estimation for μ_{sat}.

4.3 Exchanging photons with GNSS satellites

In this section, we present the preliminary results of an experiment testing the feasibility of quantum communications between a GNSS terminal and a ground station, over a channel length of about 20 000 km by using current technology. We realized the first exchange of few photons per pulse between a satellite of GLONASS constellation and

MLRO, by exploiting two-way scheme presented above. This experiment extends the limit of long-distance free-space single-photon exchange, which was demonstrated so far with a channel length of about 7 000 km by exploiting the MEO satellite Lageos [90].

4.3.1 The goal of the experiment

Satellite-based technologies are the enabling tools for a wide range of civil, military and scientific applications [96, 97, 98, 99], like communications, navigation and timing, remote sensing, meteorology, reconnaissance, search and rescue, space exploration and astronomy. In particular, Global Navigation Satellite Systems (GNSS) were developed in the second half of XX century to provide autonomous geo-localization by exploiting a network of satellite exchanging position- and time-information with different locations on Earth [100]. The strategic importance of such infrastructure led different countries to deploy their own GNSS constellations, e.g. the American Global Positioning System (GPS), the Russian GLONASS, the European Galileo, the Chinese BeiDou, the Japanese QZSS and the Indian INRSS/NAVIC. The very core of these navigation systems is the capability of safely transmitting information and data from orbiting satellites to several ground stations on Earth by exploiting radio [97] or optical communications [101]. In fact, the protection of such infrastructure from a malicious adversary is of crucial importance for both civil and military operations, representing a critical issue that is continuously and extensively under development.

At the same time, Space quantum communications represent a promising resource to guarantee unconditional security for satellite-to-ground optical links, as discussed above, and also for inter-satellite optical links [102, 103], by QKD. Due to optical losses, most of the demonstrations of satellite quantum communications were limited, so far, to LEO satellites. However, the high orbital velocity of LEO satellites limits their visibility periods from the ground station, and subsequently the time available for quantum communications to just few minutes per passage.

Conversely, the use of satellites at higher orbits can greatly extend the communication time, reaching few hours in the case of GNSS. Furthermore, quantum communications could offer interesting solutions for GNSS security for both satellite-to-ground and inter-satellite links, which could provide novel and unconditionally secure protocols for the authentication, integrity and confidentiality of exchanged signals. For example, a GNSS inter-satellite network for QC has already been proposed to strengthen the security of the Galileo architecture [104]. This would allow the generation of cryptographic keys and the construction of a secure satellite QKD-network, thus preventing the catastrophic

consequences of malicious hijacking of GNSS satellites.

4.3.2 Description of the experiment

The experimental setup.—The feasibility of quantum communications from GNSS orbits was experimentally investigated by exploiting Glonass-134 of the GLONASS constellation, which is equipped with an array of CCRs. We used the two-way scheme presented above and the experimental setup sketched in Figure 4.6.

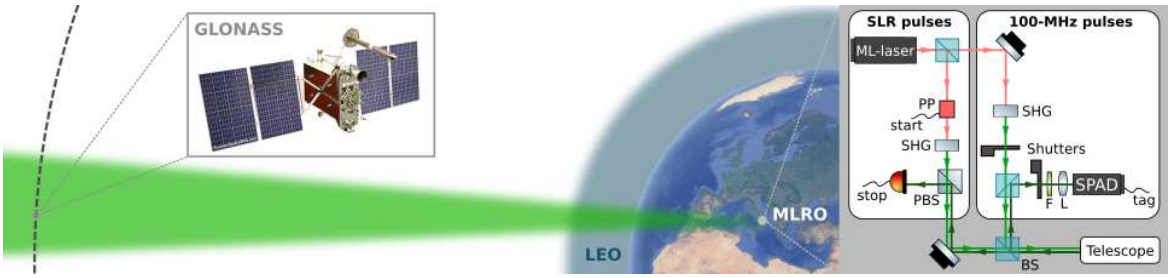

Figure 4.6: *Illustration (to scale) of the photon exchange between GLONASS and MLRO.* GNSS satellites orbit around 20 000 km away from Earth surface, well above the LEO satellites, whose maximum altitude is about 2 000 km. The right inset shows the optical setup. The mode-locked laser (ML-laser) at 1064 nm produces the 100-MHz pulsed train and the 10-Hz SLR signal, which are then up-converted at 532 nm (light green). The two beams are combined and sent to the satellite, where they are retro-reflected back to MLRO telescope (dark green). The 100-MHz train is then collected by a single-photon avalanche detector (SPAD), while the SLR pulses are received with an analog detector for synchronization purposes. Two mechanical shutters separate the transmission from the reception of the 100-MHz beam. Image of Glonass satellite taken from Russian SpaceWeb. PP: pulse-picker, SHG: second harmonic generation stage, BS: beam splitter, PBS: polarizing BS, F: spectral filter, L: focusing lens.

A setup dedicated to study the feasibility of quantum communications from GNSS was implemented in parallel to the SLR system of MLRO. The same ML-laser is used to produce the 100-MHz pulse-train and the SLR one, as described above. These two beams are combined by using a 50:50 beam splitter (BS) and the two light beams are sent to the targeted GNSS satellites.

The receiving apparatus of the 100-MHz beam is comprised of a 50:50 BS to separate the outgoing and ingoing beam, a 3 nm FWHM spectral filter (F) with transmission band centered at 532 nm, a focusing lens (L) and a silicon single photon avalanche detector (SPAD) from MPD, with ≈50% quantum efficiency, ≈400 Hz dark count rate and 40 ps of jitter. The time of arrival of the returning photons (tag) is recorded with 1 ps resolution by the time-to-digital converter quTag.

We implemented a communication protocol to separate the transmitting and receiving phases which is slightly different to the one described in Section 4.2.4. Since the round trip time of photons reflected by GNSS satellites is around 130 ms, the total period of the communication protocol is extended up to 200 ms. In the first half, the transmitting (receiving) shutter is open (close) and the 100-MHz pulses are transmitted. Viceversa,

in the second half the the receiving (transmitting) shutter is open (close) and the 100-MHz pulses coming from the satellite can be detected. In particular, the communication protocol starts with the SLR start signal at $t = 0$ ms. The 100-MHz pulses are sent to the satellite from $t = 0$ ms to $t = 100$ ms, opening the shutter placed in the transmission path. At $t = 100$ ms a second SLR pulse is sent to the satellite and after 5 ms the receiving shutter opens the receiving path till $t = 180$ ms.

Modelling the channel losses.—Due to optical diffraction, atmospheric absorption, and the finite sizes of the cross-section and active area of the CCR-array, the beam is attenuated by several orders of magnitude after being retro-reflected. As a result, the reflected pulses have a low mean number of photons μ_{sat} at the satellite, thus emulating a weak source placed on a GNSS terminal orbiting 20 000 km away from MLRO. The mean photon number per pulse μ_{sat} emitted by the simulated source is not known *a priori* , but it can be estimated *a posteriori* as

$$\mu_{\text{sat}} = \frac{R_{\text{det}}}{\nu_{\text{tx}} t_{\text{down}} t_{\text{rx}}} , \tag{4.4}$$

by experimentally evaluating the detection rate R_{det}, the transmittance of the receiving apparatus t_{rx}, the repetition rate $\nu_{\text{tx}} = 100$ MHz of the source and by modeling the down-link transmittance t_{down}. We will express the losses l in dB as $l = -10 \log_{10} t$, where t is the transmittance. The receiver losses are promptly estimated taking into account the reflection and transmission losses through all the optical elements (8.8 dB) and the quantum efficiency of the detector (3 dB).

The down-link channel losses can be evaluated as the product of the atmospheric transmission t_{a} and the geometrical transmission due to diffraction t_{diff}, that is $t_{\text{down}} = t_{\text{a}} t_{\text{diff}}$. We follow two independent approaches for estimating the transmission due to diffraction and compares the results for the validation of the model.

The targeted GNSS satellite is part of the generation GLONSS-K1, which is equipped with a planar array of CCRs, with circular and rectangular shape respectively [105]. The CCRs are characterized by the absence of coating on the reflecting faces, such that the light is back reflected by total internal reflection (TIR). This implies a far field diffraction pattern (FFDP) which is quite different from the simple Airy disk given by a circular aperture [106]. The FFDP of a TIR corner cube has a central Airy-like disk, with 26.4% reduced central intensity peak from the circular aperture with equivalent area, surrounded by six lobes placed on the vertices of a hexagon. The lobes are displaced from the center of the FFDP by $\theta_d \approx 1.4\lambda/D_{\text{CCR}}$, with $D_{\text{CCR}} = 26$ mm the CCR diameter (as described at this link), corresponding to a displacement $\theta_d \approx 29$ μrad.

Since the velocity aberration of GNSS satellites is around 26 μrad [95], the MLRO

telescope is receiving the lateral lobes of the FFDP. In particular, the lateral lobes have an intensity which is $\approx 30\%$ of the central peak. Since the central intensity peak I_0 of a circular aperture of area A depends on the power P_0 incident on it via $I_0 = P_0 A/(\lambda^2 R^2)$, with R the distance from the aperture, the transmission due to diffraction can be evaluated by

$$t_{\text{diff}} = 0.264 \cdot 0.3 \frac{A_{\text{CCR}} A_{\text{tel}}}{\lambda^2 R^2} , \tag{4.5}$$

where A_{CCR} and A_{tel} are the areas of the CCR and the ground telescope, respectively [106].

An alternative approach is given in [90] in which the FFDP is approximated as a top-hat pattern with solid angle Ω, so that the diffraction transmittance is evaluated as $A_{\text{tel}}/(\Omega R^2)$. Since the solid angle can be estimated by the array cross-section Σ [95, 107], we have that

$$t_{\text{diff}} = \frac{\Sigma}{4\pi\rho A_{\text{RRA}}} \frac{A_{\text{tel}}}{R^2} , \tag{4.6}$$

being $\rho = 0.93$ the reflectivity of the uncoated CCR and A_{RRA} the array effective area.

In clear sky conditions, the losses due to atmospheric transmission for the used $\lambda = 532$ nm is $l_a \approx 0.4$ dB [95] and considering a satellite slant distance $R \approx 20\,000$ km, the predicted down-link channel losses are $l_{\text{down}} \approx 62$ dB, from both models given by equations (4.5) and (4.6) to estimate the diffraction losses. This assessment of the channel losses allow us to experimentally estimate μ_{sat} by measuring the detection rate, as presented in the following section.

4.3.3 Experimental results

Detecting single photons from Glonass.—We provide here a detailed analysis of the data obtained from Glonass-134. In a single passage of Glonass-134, we had two distinct acquisitions separated by almost one hour corresponding to the maximum and minimum distance of the satellite from MLRO. In particular, the first acquisition lasted about 2 minutes, with mean slant distance of about 20 200 km, whereas the second one lasted about 5 minutes, with mean slant distance of 19 500 km.

In Figure 4.7 we show the signal detection rate from Glonass-134 for the second acquisition (the results for the first acquisition are analogue). The detection rate was estimated in the following way. We divided the whole acquisition in time intervals I_k of duration $\tau = 5$ s. For each interval we made the histogram (see Figure 4.8) of the time difference between the tagged detection t_{meas} and the expected time of arrival of the photon t_{ref}, with the technique presented above. Then, we chose a time window $w = 400$ ps centered around t_{ref}, much larger than the detector jitter (≈ 40 ps) since the retroreflected pulses are temporally spread by the CCR array, and estimated the number of photon detections N_{det} as the

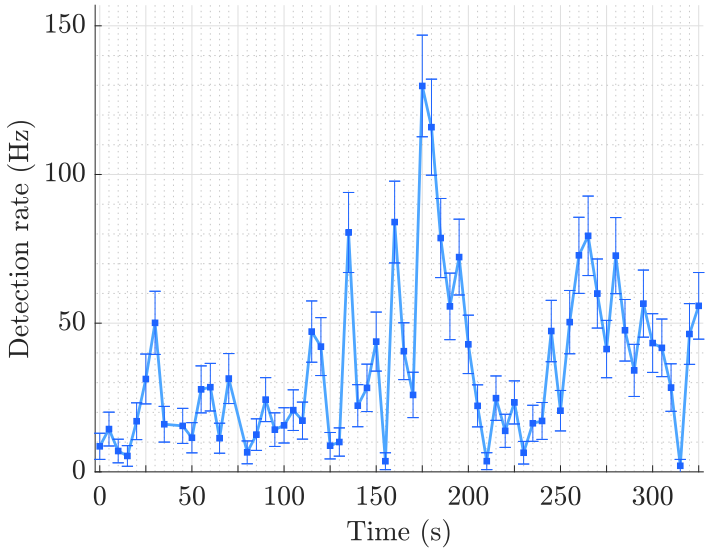

Figure 4.7: Detection rate from Glonass-134 at 19 500 km slant distance. Each point is calculated integrating over an acquisition time window I_k of $\tau = 5$ s.

difference of the total and background counts within the window. The background was uniformly distributed within the 10 ns period between two sent pulses (see Figure 4.8), therefore we estimated its rate counting the detections over a time window which is at least 1 ns away from t_{ref}. Finally, the signal detection rate was obtained via $R_{\text{det}} = N_{\text{det}}/(\tau\delta)$ where $\delta = 0.3$ is the duty cycle of the communication protocol. Then, we discarded the time windows I_k with $R_{\text{det}} < 30$ Hz, to filter out acquisition with low signal-to-noise ratio (SNR). Such selected time windows gave the integrated histogram shown in Figure 4.8.

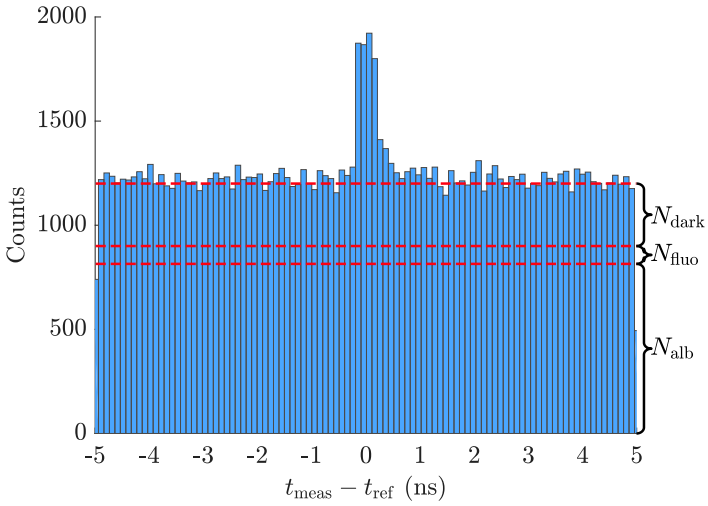

Figure 4.8: Histogram of residuals between the measured and the expected time of arrival of the photons, from Glonass-134 at a slant distance of 19 500 km. Here, we consider acquisition time windows I_k with detection rate $R_{\text{det}} > 30$ Hz. Each bin is 100 ps wide. Dashed lines show how the background is distributed among the field of view and satellite albedo (N_{alb}), fluorescence (N_{fluo}) and dark count rate of the detector (N_{dark}).

At the end of such analysis, we obtained a mean detection frequency $\overline{R}_{\text{det}} \approx 58$ Hz,

a SNR of 0.53 and mean number of photons at the satellite $\mu_{sat} \approx 14.5$ for the second acquisition of Glonass-134. In the same way we analyzed the first acquisition of the same passage, obtaining a mean detection frequency $\overline{R}_{det} \approx 59$ Hz, a SNR of 0.41 and a mean number of photons at the satellite $\mu_{sat} \approx 16.1$. In this case we used a signal time window w of 600 ps due to the larger temporal spread.

A large part of the counts reported in Figure 4.8 is due to noise. The intrinsic dark count rate of the detector amounts to $N_{dark} \approx 700$ Hz. They are estimated in the first 100 ms of the period, when the receiving shutter is closed. Another source of noise is the fluorescence that occurs when the upgoing SLR pulse passes through the optical elements in common with our optical path. The intensity of the fluorescence light reduces exponentially in time with half-life that depends on the material. The remaining tail is included in the counts and amounts to $N_{fluo} \approx 195$ Hz. The remaining, and predominant, detections are due to satellite albedo and background of the field of view. This noise is uniformly distributed in time and amounts at $N_{alb} \approx 1.9$ kHz.

Observing the "signature" of Glonass.—We were also able to resolve the temporal distribution of the returning pulse given by the particular design of the CCR array, hence revealing the "signature" of Glonass-134 that is equipped with a holed circular CCR array, sketched in the left panel of Figure 4.9. If the incident angle θ_i with respect to the normal tothe array is not zero (see the right panel of Figure 4.9), the pulses reflected by the CCRs closer to the ground station have a smaller round trip time with respect to the further CCRs, resulting in a temporal spread with a characteristic "dip" of the pulse.

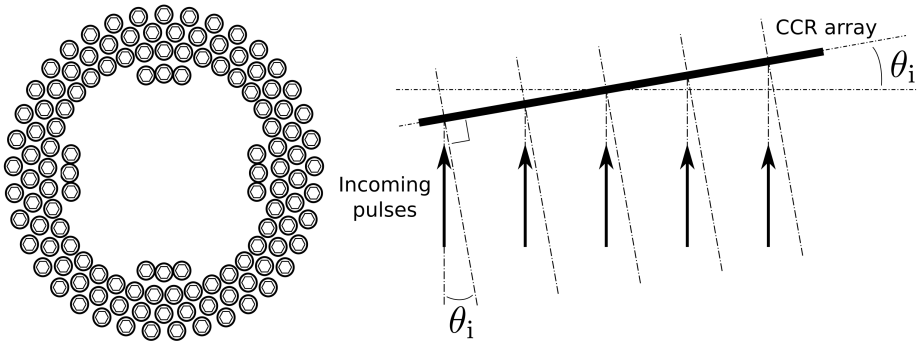

Figure 4.9: **(left panel)** Sketch of the holed circular CCR array of Glonass-134. **(right panel)** The incoming pulses impinge on the CCR array with a non-zero angle θ_i with respect to the array normal. The central hole in the array causes a characteristic "dip" in the temporal profile of the detected pulses.

We simulated the temporal shape of the pulse for incident angles 5 deg and 9 deg, corresponding to the incident angles of the two acquisitions, and compare them with the actual data in Figure 4.10. From the simulation, the corresponding temporal peak-to-peak distance is 250 ps and 430 ps for the two acquisitions respectively, in agreement with the

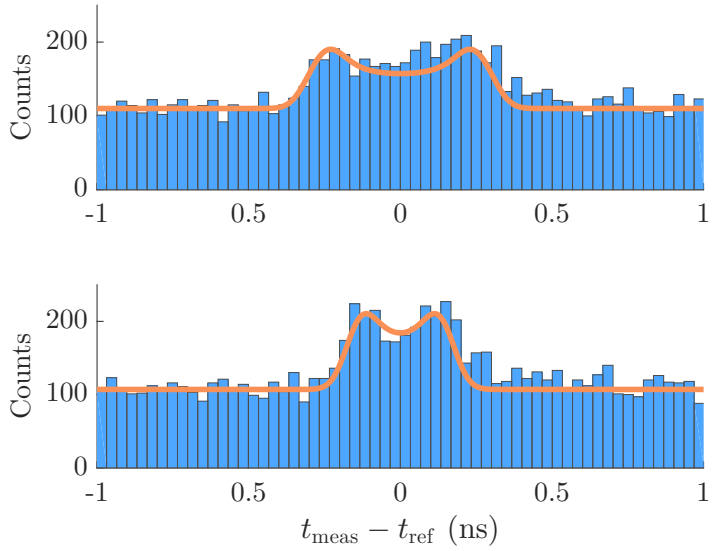

Figure 4.10: Histogram of residuals between measured and expected time of arrival of the photons for Glonass-134 at 20 200 km (**top**) and 19 500 km (**bottom**).

experimental estimation. The simulation is performed supposing that the single CCR does not change the temporal shape of the pulse, it but introduces a temporal offset depending on its position in the array and on the incident angle of the beam. Using a pulse with 100 ps of FWHM, as in the actual experiment, and summing up the contributions of all CCRs, we obtained the shapes depicted in the figure. Note that the continuous lines shown in Figure 4.10 are obtained by such a-priori model (adding the measured background) and not by fitting the data.

As shown in the work by Otsubo *et al.* [108], GLONASS flat CCRs array exhibits particular temporal distribution determining higher error in the laser ranging measurement, in which the mean number of photons at the receiver is usually much greater than one. The authors of [108] observed the "signature" of the GLONASS satellites by integrating one year of data acquisition. On the contrary, our result shows that using single photons detectors and high repetition source the temporal distribution of the pulse can be measured, even with low mean number of photon at the satellite and short data integration time. A more accurate measurement could be done using a mean number of photons of about one at the receiver, however this is beyond the scope of our experiment. We note that this measurement could even be used to determine the orientation of the array and hence the attitude of the satellite, which is of critical importance for the processing of GNSS data [94, 109, 110].

4.4 Towards QKD between Micius and MLRO

4.4.1 Satellite-based Quantum Key Distribution

A typical free-space QKD system.—The most effective way to perform QKD via free-space channels is by implementing the BB84 *decoy-state* protocol [111, 112], as demonstrated in many experimental works [113, 114, 115, 116, 78, 79]. This protocol is an improvement of the original BB84 protocol [118], which allows to use weak-coherent pulses instead of true single photon states while remaining secure even against the photon-number-splitting (PNS) attack.

Typical free-space systems used to implement the BB84 decoy-state share the logical structure sketched in Figure 4.11. The key ingredients are the *QKD source* and the *QKD detection* units, which are in charged, respectively, of preparing and measuring the states exchanged in the protocol. Alice randomly prepares four different state in two mutually unbiased bases, like the polarization states $\{|H\rangle, |V\rangle\}$ and $\{|D\rangle, |A\rangle\}$, by setting three different intensities (or mean photon number per pulse), which are called vacuum $\mu_0 = 0$, weak-decoy μ_d and signal μ_s. Bob, on the other side, measures the incoming pulses in the H/V or D/A basis with fixed probability (*biased basis choice* [117]). By associating the "0" or "1" bit to each prepared and measured state and by comparing the two bit strings they obtained after many runs of the protocol, Alice and Bob can finally share a random bit *key K* which is unconditionally secure and that can be used with the *one-time-pad* (OTP) for secure communication purposes [33, 15]. The security is guarantee by the laws of Quantum Mechanics: each attempt to get the key by intercepting or cloning the sent state without disturbing the key generation process is actually forbidden by the Heisenberg's principle and the no-cloning theorem, which allow Alice and Bob to reveal such malicious attempt and to abort the protocol.

The other logic units necessary to implement the BB84 decoy-state protocol in a free-space channels are a *Pointing, Acquisition and Tracking* (PAT) system, a *Synchronization* (Synchro) unit and a *Telecom* interface between Alice and Bob.

The PAT unit is in charge of allowing Alice and Bob to send and receive the quantum signals over the free-space channel, and it is usually comprised of a transmitting and a receiving telescope and a close-feedback coarse and fine pointing system to keep the two telescope aligned one with respect to the other.

The Synchro unit is in charge of the real-time timing of the protocol, e.g., driving the lasers and tagging the detections, and of the technique which allows Alice and Bob to compare their raw bit strings *a posteriori*. In order to reach this purposes, a pulsed laser

paced by a GPS clock is usually implemented. It is worth noticing that the pulsed laser used for synchronization purposes can be used also as a beacon of the PAT system.

The Telecom unit is in charged of the (authenticated) *classical* communication between the two terminals, which allows the correct implementation of the protocol, from the raw-key exchange to the other post-processing phases, e.g. *basis-reconciliation* (or *sifting*), *error-correction* and *privacy-amplification* [33, 15].

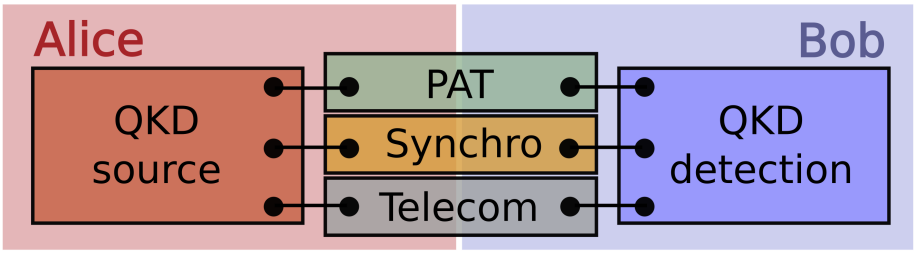

Figure 4.11: Logical structure of a typical free-space QKD system.

Satellite-relayed QKD at the global scale.— In satellite QKD, Alice is the orbiting satellite. Exploiting the satellite as a relay can guarantee the security of communications all over the world. Indeed, two distant ground stations A and B may share a secure key in the following way. Suppose the satellite is orbiting over the ground station A, with which the satellite implements a QKD protocol generating the secure key K_A. Then, when the satellite gets over the ground station B, it generates and shares another secure key K_B. At this point, the satellite has both keys K_A and K_B, and it calculates the key K_{AB} by XORing K_A and K_B, that is $K_{AB} = K_A \oplus K_B$, where $\oplus$ is the binary XOR operation. Finally the satellite sends K_{AB} to ground station B using a classical public channel, so that ground station B can reconstruct K_A. The two ground stations now store the key K_A to be used whenever they have to share a secret message via OTP. The use of a satellite as a trusted node has been demonstrated in [79] to secure an intercontinental video call between Austria and China.

4.4.2 The preliminary test performed at MLRO

We performed in July 2018 a preliminary test to implement a QKD link between Micius satellite and MLRO in Matera, which is the object of this section. Shangkai Liao and Jigang Ren of the Chinese Academy of Sciences supervised the test al MLRO.

More details on Micius satellite.—One payload of Micius satellite is a space-qualified QKD transmitter, whose details can be found in [78, 79]. Essentially, Micius has eight tunable pulsed-lasers centered at 850 nm with a repetition rate of 100 MHz. These lasers

are used to generate the states $|H\rangle, |V\rangle, |D\rangle, |A\rangle$ needed to implement the BB84 decoy-state protocol described above.

For PAT and synchronization purposes, Micius mounted a pulsed beacon laser at 532 nm, which is sent towards the receiving ground-station. To operate properly, a continuous-wave (CW) strong (3 W of mean power) red beacon at 671 nm must be sent to the satellite from the ground. The 671 nm beacon laser is acquired by two cameras on the satellite, to implement a close-feedback PAT loop based on movable mirrors. The red beacon was installed on the MLRO telescope tube and aligned by using the SLR beam.

The receiving setup at MLRO.—For the preliminary test performed on 11th July 2018, from 22:21 to 22:28 (UTC time), Micius sent down the green beacon and a horizontally polarized CW laser at 850 nm, which is the signal beam of the test. The expected photon flux for the signal at the primary mirror of MLRO was about $6.5 \cdot 10^8$ photons/m^2/s with Micius at 1 000 km of slant distance.

The receiving setup we implemented at MLRO has two roles. Firstly, it must realize Bob's part of the PAT system to acquire the green beacon at 532 nm for pointing and synchronization purposes. Secondly, it has to implement the 850 nm BB84 polarization-based detection unit.

The setup used was assembled at the RX Table of MLRO as sketched in Figure 4.12. On the MLRO telescope tube it is installed a wide-angle-camera searching for the beacon sent from Micius (coarse pointing).

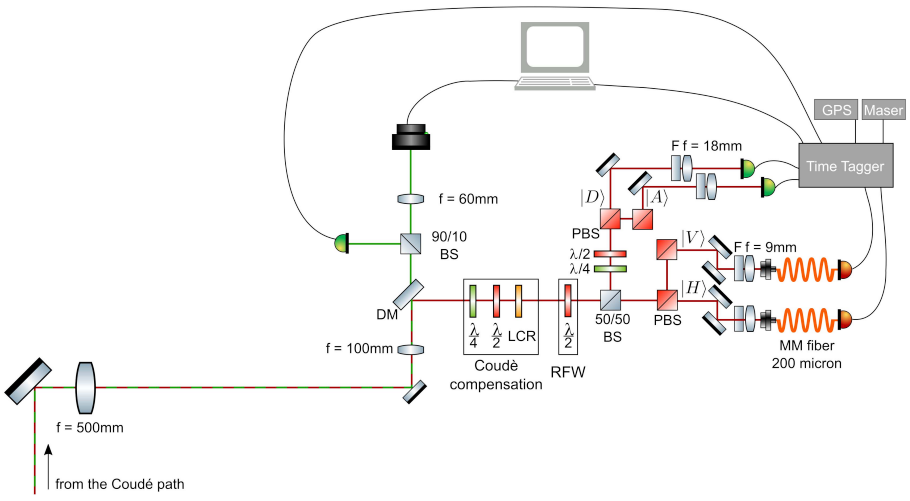

Figure 4.12: Setup used for the preliminary test of QKD between Micius and MLRO.

The two beam reached the RX Table after have been collected by the MLRO 1.5 m telescope and have passed the Coudé path. The first pair of lenses implemented a 5× beam reducer to collimate the incoming beam from the telescope to a beam of about 1 cm of

diameter. The two beams are then separated by a dichroic mirror (DM).

The green one passed through an unbalanced beam-splitter for being coupled to both a SPAD detector for synchronization (after being tagged by the quTau time-tagger) and to a CMOS camera, the output of which was used by the MLRO operator in real-time as fine pointing.

The 850 nm signal beam was then corrected for the polarization rotation introduced by the Coudé path. Indeed, the mirrors of the Coudé path, even if not introducing depolarization, induced a rotation of the polarization state sent by Micius, which depends on the actual pointing of the MLRO telescope (azimuth and elevation angles) and has to be corrected in real-time. To correct this polarization transformation, we implemented a motorized triplet made by a QWP, a HWP and a liquid crystal retarded (LCR), which can implement any unitary transformation (as described in Section 2.2.2). Indeed, the LCR acts as a wave-retarder in which the retardance Γ depends on the applied voltage. Furthermore, the satellite motion introduced a polarization rotation in the sent horizontal polarized state. To correct this rotation we introduced an additional HWP, called reference-frame-waveplate (RFW), in order to align the reference system of the satellite to the one of the optical table.

The 850 nm signal beam then passed through the QKD detection unit, which was made by a 50:50 beam-splitter (BS) and four polarizing beam-splitter (PBS) to perform the measurement in the $\{|H\rangle, |V\rangle\}$ and $\{|D\rangle, |A\rangle\}$ bases. Experimentally, it is better to use an additional PBS on the reflected output of the PBS to improve the polarization contrast. In the D/A arm, a pair of waveplates was introduced to perform the measurement, as described in Section 2.2.2.

At the output of the detection unit the beam was coupled to two different detection systems, one for each measurement basis, to compare their performances and choose the one to be implemented in the real QKD experiment. The H/V basis was measured by a fiber-based SPADs (55% of detection efficienty) after being coupled to multi-mode (MM) fibers with 200 μm of core and spectrally filtered (F, 20 nm band). The D/A basis was measured by using two free-space SPADs with 10% of detection efficiency.

The four signals of the SPADs are then tagged by the time-tagger, which is also paced by the clock signal of a GPS and by the atomic clock of MLRO (Maser).

Preliminary results.—The goals of this preliminary test were:

i) verify that the green beacon from Micius is correctly detected for both pointing and synchronization purposes;

ii) verify that the polarization compensation system implemented by us worked correctly.

For what regards i), the MLRO telescope correctly tracked Micius using the 2D line elements provided by the Chinese Academy of Sciences, which are essentially the prediction of the satellite trajectory. Further corrections in real-time were made by hand by the MLRO operator by looking firstly at the wide-angle-camera and than at the output of the CMOS one which is more precise. The detectors had a field-of-view (FOV) of about 30 μrad, hence the operator had to keep the image of the beacon acquired by the CMOS camera inside the red circle shown in Figure 4.13 during the Micius passage. Figure 4.13 shows the centroids of the spot recorded by the camera during the whole passage, showing that the pointing was good enough to allow the test. Furthermore, the histogram of the time difference between two consecutive tags of the synchronization SPAD show the peaks every 91 μs, as expected from the fact that the beacon repetition rate was about 11 kHz.

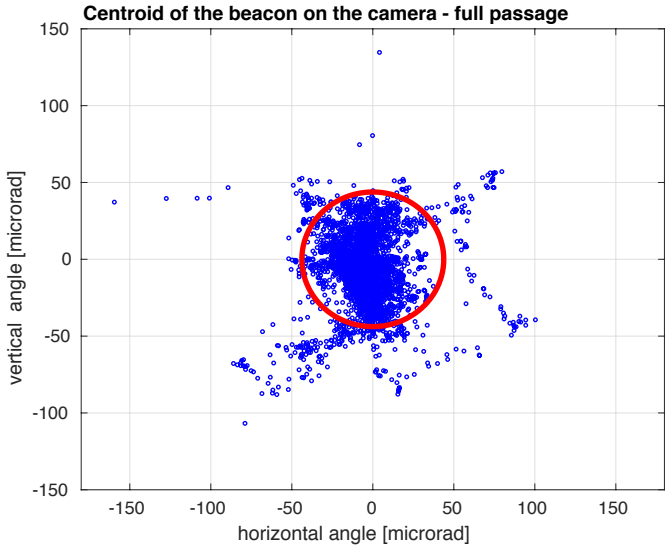

Figure 4.13: Centroids of the beacon acquired by the CMOS camera during the passage of Micius.

For what regards ii), we calibrated the Coudé compensation system by taking five points along the predicted trajectory of Micius and using a CW laser at 850 nm mounted in front of the primary mirror of MLRO. The measured contrast of such calibration was about 200:1 ($< 0.5\%$) for both bases, good enough to correctly discriminate between the four polarization states generated by Micius. The actual angles of the motorized waveplates and the voltage to be applied to the LCR was obtained by fitting the values of the calibration points. The triplet was set in real-time during the satellite passage, as well as the rotation angle of the RFW. We measured the degree of polarization (DOP, see Section1.1.3) of the signal beam once detected in our optical table by using r_3 from the detections in the H/V basis and r_1 from the D/A one (see Section 2.2.2), which results

$\sqrt{r_1^2 + r_3^2} = 0.96 \pm 0.04$ (estimated over all the passage), attesting the linearity of the incoming polarization. It is worth noticing that we changed the offset of the RFW during the passage three times, to project also onto the D/A basis.

Concluding, the preliminary results obtained in July 2018 made us confident to manage to implement an actual QKD link between Micius and MLRO, confirming the role of MLRO as a state-of-the-art receiver for Space quantum communications. Two nice pictures taken during the experimental campaign are in Figure 4.14.

Figure 4.14: **(left panel)** The red beacon laser mounted on the MLRO telescope. **(right panel)** Micius satellite during the passage.

Chapter 5

Observing single-photon interference along satellite channels

Quantum interference arising from the superposition of states is a striking evidence of the validity of Quantum Mechanics, which was confirmed in many experiments and that is also exploited in applications. However, Quantum Mechanics, as every scientific theory, is valid within the limits in which it has been experimentally verified. With the spirit of extending such limits, we experimentally demonstrated single-photon interference at a ground station due to the coherent superposition of two photon time-bins reflected by a rapidly moving satellite orbiting thousands of kilometers away.

This chapter is dedicated to this Quantum Optics experiment exploiting a Space interferometer, the first I was involved in during my master and PhD activities. Some contents of this chapter are part of our work [89].

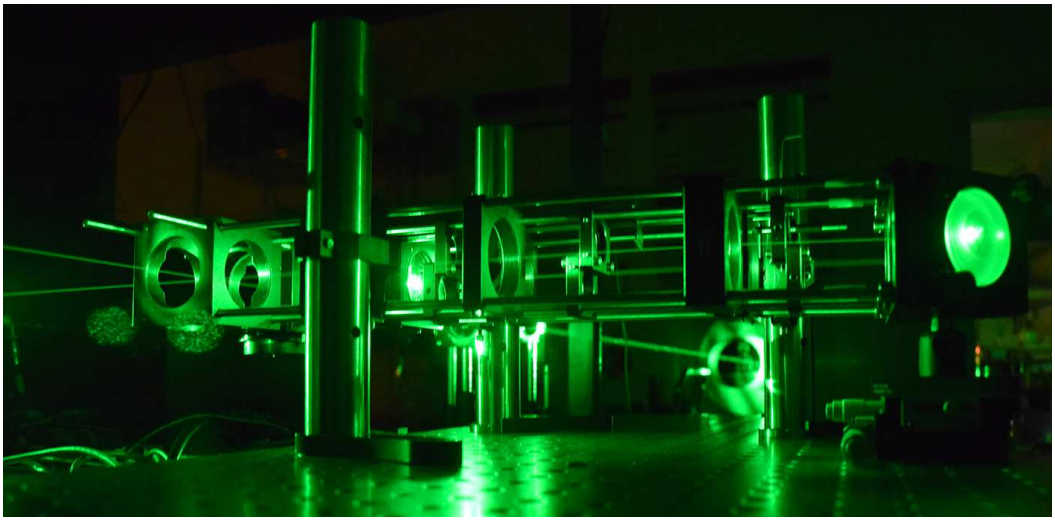

The interferometer used in the experiment.

5.1 Introduction: quantum interference

Quantum interference has played a crucial role to highlight the essence of Quantum Mechanics since the Einstein-Bohr dialogues at the end of the Twenties [119]. It originates when *alternative possibilities* in a quantum process are indistinguishable, like in the case of individual particles that may be simultaneously in more than one place as in the well-known Young's double-slit experiment [2, 11, 12].

Interference phenomena occur in Quantum Mechanics whenever the probability amplitudes for reaching a given final state for a system from a given initial state is the sum of two or more partial amplitudes with well defined phase relations one with respect to each other. Each partial amplitude represents an alternative way in which the system can evolve from the initial state to the final one. For example, we may consider a single-photon state incident on the slits. The final state of the field will be the vacuum state $|\text{vac}\rangle$, where the photon has been absorbed. The total amplitude for reaching this final state is the sum of two amplitudes, each associated with the passage of the photon through one of the two slits. The existence of the interference fringes is related to our inability to determine which of the possible paths the photon actually takes: any attempt to define which of the two paths the photon followed actually cancels the interference fringes, as imposed by the *Heisenberg principle* [2]. Hence, the different amplitude related to the different paths by which a system may evolve contribute to the total amplitude with a well-defined phase relationship. Another example of quantum interference is the balanced Mach Zehnder interferometer described in Section 2.1.2.

Quantum interference was already observed with photons [120, 121], electrons [122], neutrons [123] and even with large molecules with masses exceeding 10 000 amu [124]. One of the main challenges in Quantum Physics is establishing if fundamental bounds to interference exist: for instance, can quantum interference be measured by observers in relative motion and at arbitrary large distance one between the other? Our work presented in this chapter moved from this question. We demonstrated interference at the single photon level along satellite-ground channels by exploiting temporal modes of single photons, i.e. the time-bin encoding of Section 2.2.3. We obtained a coherent superposition between two single-photon wavepackets on ground and observed their interference after a *Space trip* involving the reflection by a rapidly moving satellite at very large distance, with a total path length up to 5 000 km. The varying relative velocity of the satellite with respect to the ground station introduces a modulation in the interference pattern which can be predicted by special relativistic calculations, as explained below.

5.2 Description of the experiment

5.2.1 Time-bin encoding for Space interferometry

In this experiment the Quantum Optics setup of Figure 4.4 is comprised of an unbalanced Mach-Zehnder interferometer (MZI), as sketched Figure 5.1. With such interferometer, for each qubit pulse, a coherent state $|\Psi_{\text{out}}\rangle$ in two temporal modes is generated at MLRO. The temporal imbalance $\Delta t \approx 3.4$ ns between the two arms corresponds to a length difference between the two arms of $\Delta t = c\Delta t \approx 1$ m, which is much longer than the coherence time $\tau_c \approx 80$ ps of the qubits pulses.

Using the MLRO telescope, the state $|\Psi_{\text{out}}\rangle$ is directed to a retroreflector placed on a satellite in orbit. The satellite retroreflectors redirect the beam back to the ground station, where it is collected and injected into the same MZI used in the uplink. After the reflection by the satellite and the downlink attenuation, the state collected by the telescope can be well approximated by

$$|\Psi_r\rangle = \frac{1}{\sqrt{2}}\left(|S\rangle - e^{i\varphi(t)}|L\rangle\right), \tag{5.1}$$

that is a time-bin superposition of two single-photon wavepackets $|S\rangle$ and $|L\rangle$.

The relative phase $\varphi(t)$ is determined by the satellite instantaneous radial velocity with respect to ground, $v_r(t)$. Indeed, at a given instant t, the satellite motion determines a shift $\delta r(t)$ of the reflector radial position, during the separation Δt between the two wavepackets, as shown in Figure 5.2. This shift can be estimated at the first order as

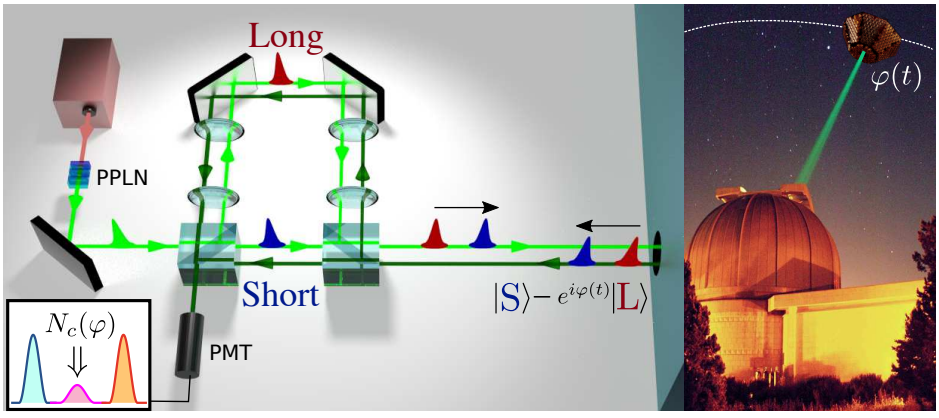

Figure 5.1: *Scheme of the experiment.* We show the unbalanced MZI with the two $4f$-systems used for the generation of the coherent state in two temporal modes and the measurement of the interference. Light and dark green lines respectively represent the beams outgoing to and ingoing from the telescope. In the inset, we show the expected detection pattern: the number of counts N_c in the central peak varies according to the kinematic phase φ imposed by the satellite. Right photo shows MLRO with the laser ranging beam and the Beacon-C satellite (not to scale). The phase $\varphi(t)$ depends on the satellite radial velocity as described in the text.

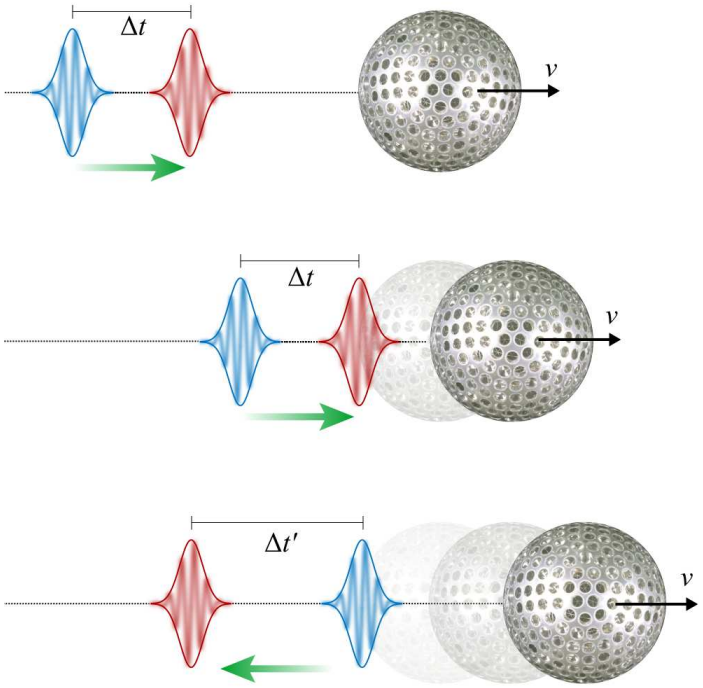

Figure 5.2: *Kinematic Phase Shift introduced by the satellite imotion.* The relative phase $\varphi(t)$ is determined by the satellite instantaneous radial velocity with respect to the ground, $v_r(t)$. Intuitively, the satellite motion determine a shift $\delta r(t) \approx v_r(t)\Delta t$ of the reflector's radial position during the separation Δt between the two temporal modes of the wave packet.

$\delta r(t) \approx v_r(t)\Delta t$, and its value may reach a few tens of micrometers for the satellites here used.

For instance, in Figure 5.3 we show the value of $v_r(t)$, that ranges from -6 to 6 km/s for the selected passage of the Beacon-C satellite. The shift in the radial position introduced an optical path difference travelled by the two wavepacket which is equal to $2\delta r(t)$. Therefore, the satellite motion imposes during reflection the additional *kinematic phase*

$$\varphi(t) \approx 2\delta r(t)\frac{2\pi}{\lambda} \approx \frac{4\pi}{\lambda} v_r(t)\Delta t \tag{5.2}$$

between the wavepackets $|L\rangle$ and $|S\rangle$, where $\lambda = 532$ nm is the pulse wavelength in vacuum. The typical values of the satellite-induced phase-shift for the Ajisai satellite during a passage are in Figure 5.4.

A single MZI for state generation and detection intrinsically ensures the same unbalance of the arms and avoids active stabilization, necessary otherwise with two independent interferometers. As detailed below, two $4f$-systems realizing an optical relay equal to the arm length difference were placed in the long arm of the MZI. The relay is required to match the interfering beam wavefronts that are distorted by the passage through atmospheric turbulence: otherwise, the latter may cause distinguishability between the two paths, washing out the interference. The MZI at the receiver is able to reveal the interference between the two returning wavepackets. At the MZI outputs we expect detection

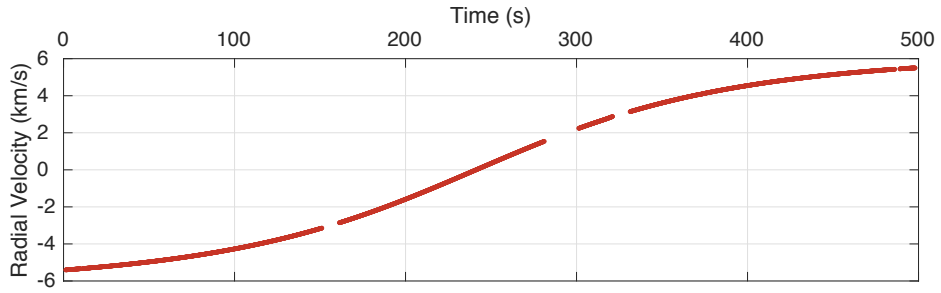

Figure 5.3: Measured radial velocity of the Beacon-C satellite ranging from −6 km/s to +6 km/s as a function of time during a single passage.

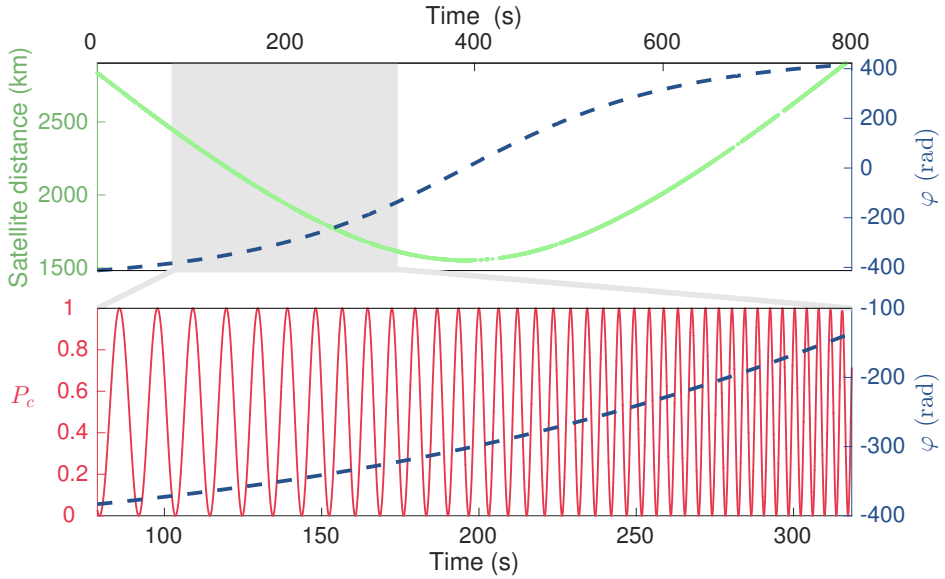

Figure 5.4: *Kinematic phase and interference pattern*. **(top panel)** We show the measured satellite distance and the predicted kinematic phase $\varphi(t)$ estimated by (5.5) as a function of time for a passage of the Ajisai satellite. Shaded area represents the temporal window of data acquisition. **(bottom panel)** Kinematic phase $\varphi(t)$ and theoretical probability $P_c(t)$ in the shaded area. The interference pattern is modulated according to the value of $\varphi(t)$ determined by the satellite velocity.

times that follow the well known three-peak profile (see Figure 5.1): the first peak represents the pulse $|S\rangle$ taking again the short arm, while the third represents the delayed pulse $|L\rangle$ taking again the long arm. In the central peak we expect indistinguishability between two *alternative possibilities*: the $|S\rangle$ pulse taking the long arm and the $|L\rangle$ pulse taking the short arm in the path along the MZI toward the detector. The signature of interference at the single photon level is then obtained when the counts in the central peak differ from the sum of the counts registered in the lateral peaks.

To measure the interference we used a single photon detector (photomultiplier, PMT) placed at the available port of the MZI, as shown in Figure 5.1. For a moving retroreflector, as detailed below, special relativistic calculations show that the probability P_c of detecting

the photon in the central peak, as a function of the passage time, is given by

$$P_c(t) = \frac{1}{2}\left[1 - \mathcal{V}(t)\cos\varphi(t)\right], \tag{5.3}$$

with

$$\mathcal{V}(t) = e^{-\frac{\lambda^2\varphi^2(t)}{8\pi c^2\tau_c^2}} \approx 1, \tag{5.4}$$

and

$$\varphi(t) = \frac{2\beta(t)}{1+\beta(t)}\frac{2\pi c}{\lambda}\Delta t\,. \tag{5.5}$$

We note that for a retroreflector at rest we expect $P_c = 0$. The parameter $\beta(t)$ is defined as

$$\beta(t) := \frac{v_r(t)}{c} \tag{5.6}$$

The above relation is obtained by time-of-flight calculations together with the Doppler effect that changes the angular frequency of the reflected pulses from $\omega_0 = (2\pi c)/\lambda$ to

$$\omega_0' = \frac{1-\beta}{1+\beta}\omega_0 \tag{5.7}$$

We note that the first order approximation of (5.5) gives the approximated phase phase $\varphi(t) \approx 4\pi v_r(t)\Delta t/\lambda$ of (5.2). The theoretical visibility $\mathcal{V}(t)$ is approximately 1 since the β factor is upper bounded by $3\cdot 10^{-5}$ in all the experimental studied cases, while the ratio $\Delta t/\tau_c$ is of the order of 10^2.

5.2.2 Further details of the interferometer

We give a detailed description of the unbalanced Mach-Zehnder interferometer (MZI) used for the generation and measurement of the interference. The interferometer, realized by two beam splitters (BSs), is schematically shown in Fig. 5.5**A**. The difference between the short (S) and long (L) arm is approximately 1 m.

In order to observe interference it is necessary to perfectly match the wavefronts of the wave packets traveling through the short or the long arm. This matching is particularly necessary for the photon beams reflected by the satellite that are subjected to the atmosphere distortion. To this purpose, we exploited two $4f$-systems that realize an optical relay of length equal to the path difference between the long and short arm of the MZI. Each $4f$-system is composed by two lenses with focal length $f = 125$ mm, as shown in Figure 5.5**A**. It is worth noticing that the ABCD matrix of a single $4f$-system is $-\mathbb{1}_2$ [14]: while realizing an optical relay of length $4f = 500$ mm, it realizes also a spatial inversion on the wavefront which must be compensated by a second $4f$-system.

In Figure 5.5**B** we show the performance of the two $4f$-systems. At the output of the MZI we imaged the primary mirror while the telescope was pointing at a bright star. The two images in Figure 5.5**B** are obtained by blocking the long and short arm respectively. The two images are comparable, showing that the wavefronts traveling the short or long arm are well matched at the output of the interferometer.

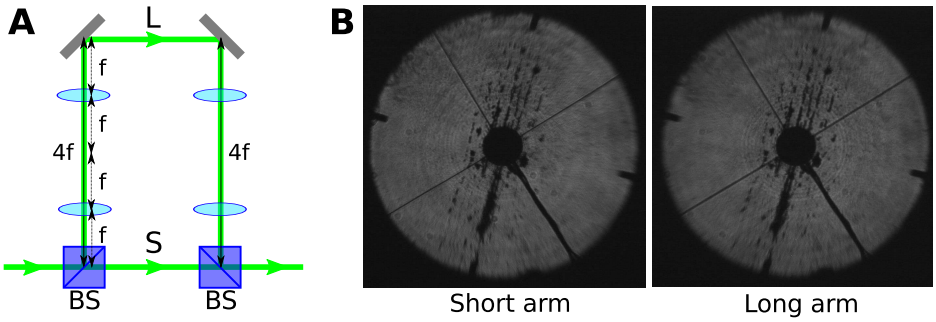

Figure 5.5: **(A)** Scheme of the unbalanced Mach-Zehnder interferometer used in the experiment. **(B)** Images of the primary mirror with only the short or long arm opened. We exploited the secondary mirror spider and the condensation spots on the primary mirror surface for checking the alignment of the interferometer.

5.2.3 Special relativistic calculations for the detection probability

In this section we will derive the effect of the reflection by a mirror moving at constant velocity on the superposition between two photon temporal modes, which leads to equations (5.3), (5.4) and (5.5). The most effective way to obtain such relations is to use Einstein' special relativity [125, 126] to correctly describe relations between objects moving at constant velocity one respect the other.

Let's consider a single photon wavepacket whose peak passes at $r = 0$ for $t = 0$. Its wavepacket is given by

$$\psi_0(\tau_-) = \sqrt[4]{\frac{2}{\tau_c^2}} e^{-\pi \frac{\tau_-^2}{\tau_c^2}} e^{i\omega_0 \tau_-} \tag{5.8}$$

where we have defined the quantities

$$\tau_\pm := \frac{r}{c} \pm t\,, \tag{5.9}$$

ω_0 is the central angular frequency and r is the direction of propagation.

After such the pulse passed the MZI, the output is given by

$$\psi_1(\tau_-) = \frac{1}{\sqrt{2}}[\psi_0(\tau_-) - e^{-i\omega_0 \Delta t} \psi_0(\tau_- - \Delta t)], \tag{5.10}$$

where Δt is the MZI imbalance.

We now consider a mirror on a satellite moving at constant velocity with respect to the interferometer that at time $t = 0$ is located at $r = r_{\text{sat}}$. We may change reference frame by setting the origin at the location of the satellite. The corresponding Lorentz transformation [125] are given by

$$\begin{cases} r' = \gamma(r - r_{\text{sat}} - \beta c t) \\ t' = \gamma(t - \beta \dfrac{r - r_{\text{sat}}}{c}) \end{cases} \qquad \begin{cases} r = r_{\text{sat}} + \gamma(r' + \beta c t') \\ t = \gamma(t' + \beta \dfrac{r'}{c}) \end{cases} . \tag{5.11}$$

The state in (5.10) is directed toward the mirror and the wave function in the mirror reference frame can be derived by the transformations of the $\tau_\pm$ parameters:

$$\tau_\pm = \gamma(1 \pm \beta)\tau'_\pm + \frac{r_{\text{sat}}}{c} = \sqrt{\frac{1 \pm \beta}{1 \mp \beta}}\tau'_\pm + \frac{r_{\text{sat}}}{c} . \tag{5.12}$$

In the mirror reference frame, the mirror reflection can be simply described by the transformation $\tau'_- \to -\tau'_+$. We now use (5.12), namely $\tau'_+ = \frac{1}{\gamma(1+\beta)}(\tau_+ - \frac{r_{\text{sat}}}{c})$ to go back to the interferometer reference frame. If we define $t_{\text{rtt}} := \frac{2}{1-\beta}\frac{r_{\text{sat}}}{c}$, the total transformation can be summarized by

$$\begin{aligned} \tau_- &\xrightarrow{\text{boost to mirror ref. frame}} \gamma(1-\beta)\tau'_- + \frac{r_{\text{sat}}}{c} \xrightarrow{\text{reflection}} -\gamma(1-\beta)\tau'_+ + \frac{r_{\text{sat}}}{c} \\ &\xrightarrow{\text{boost back to ground ref. frame}} -f_\beta(\tau_+ - t_{\text{rtt}}), \end{aligned} \tag{5.13}$$

where

$$f_\beta := \gamma^2(1-\beta(t))^2 = \frac{1-\beta(t)}{1+\beta(t)} . \tag{5.14}$$

Note that $f_\beta = f_{\beta(t)}$ is actually a function of the passage time t, since it varies with the motion of the satellite. It is worth noticing that also normalization should be changed in order to preserve normalization of the wavepacket.

Hence, the beam coming back from the satellite is

$$\begin{aligned} \psi_2(\tau_+) &= \sqrt{f_\beta}\psi_1(-f_\beta(\tau_+ - t_{\text{rtt}})) \\ &= \frac{\gamma(1-\beta)}{\sqrt{2}}[\psi_0(-f_\beta(\tau_+ - t_{\text{rtt}})) - e^{-i\omega_0\Delta t}\psi_0(-f_\beta(\tau_+ - t_{\text{rtt}}) - \Delta t)] . \end{aligned} \tag{5.15}$$

We now comment the two contributions to the wavepacket. The first term is

$$\psi_0(-f_\beta(\tau_+ - t_{\text{rtt}})) = \sqrt[4]{\frac{2}{\tau_c^2}} e^{-\pi \frac{f_\beta^2(\tau_+ - t_{\text{rtt}})^2}{\tau_c^2}} e^{-i f_\beta \omega_0 (\tau_+ - t_{\text{rtt}})} , \tag{5.16}$$

representing a pulse with a coherence time stretched (or compressed) by the doppler effect: its coherence time is indeed

$$\tau'_c = \frac{\tau_c}{f_\beta} = \frac{1+\beta}{1-\beta}\tau_c . \tag{5.17}$$

We also note that the parameter t_{rtt} represents the time that the pulse peak takes to come back to the origin (namely the round trip time). The second term in (5.15) represents the pulse of (5.16) delayed by $\Delta t' = \frac{\Delta t}{f_\beta}$. The same relation applies also to the strong SLR pulses at 10 Hz, that are separated in time by $\Delta T = 100$ ms. As detailed in the following, by measuring the temporal separation $\Delta T'$ of the SLR pulses at the receiver, it is possible to determine the satellite radial velocity. Spacetime diagrams for the pulses going upward to and downward from the satellite are shown in Figure 5.6 for different parts of the satellite orbit.

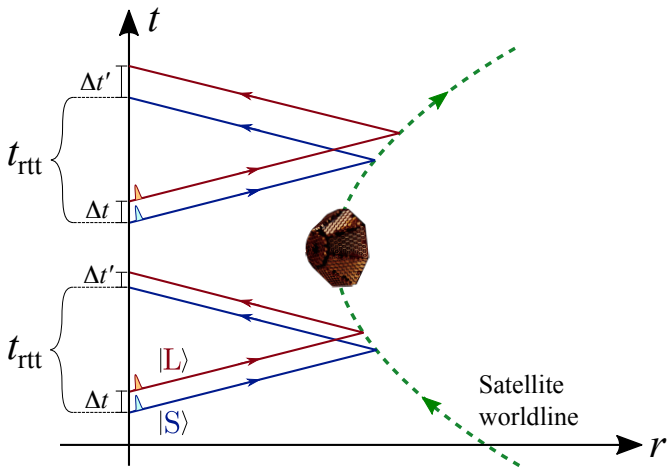

Figure 5.6: *Spacetimes diagrams of light propagation.* Short and Long arm pulses are represented by blue and red color respectively. Dashed green line represents the satellite trajectory. As explained in the text, pulses separated on ground by a delay Δt are received with a delay $\Delta t' = \Delta t / f_\beta$ due to the motion of the satellite. The round trip time is t_{rtt}. Satellite distance r and time t are not to scale.

After passing again in the interferometer, we get at the available detection port of the MZI (see Figure 5.1) the following state:

$$\begin{aligned}\psi_3(\tau_+ + t_{\text{rtt}}) &= \frac{i}{\sqrt{2}}\left[\psi_2(\tau_+ + t_{\text{rtt}}) + e^{-i\omega_0\Delta t}\psi_2(\tau_+ + t_{\text{rtt}} + \Delta t)\right] \\ &= \frac{i\sqrt{f_\beta}}{2}\Big\{\left[\psi_0(-f_\beta\tau_+) + e^{-i\omega_0\Delta t}\psi_0(-f_\beta(\tau_+ + \Delta t))\right] \\ &\quad - e^{-i\omega_0\Delta t}\left[\psi_0(-f_\beta\tau_+ - \Delta t) + e^{-i\omega_0\Delta t}\psi_0(-f_\beta(\tau_+ + \Delta t) - \Delta t)\right]\Big\}. \quad (5.18)\end{aligned}$$

We now have three pulses at the detector: the probability of getting the photon in the

central pulse at $r = 0$ is given by

$$\begin{aligned} P_c(t) &= \frac{f_\beta}{4}\int \mathrm{d}t' |\psi_0(-f_\beta(t'+\Delta t)) - \psi_0(-f_\beta t' - \Delta t)|^2 \\ &= \frac{1}{2}\left\{1 - \sqrt{\frac{2}{\tau_c^2}}\int \mathrm{d}t' \mathrm{Re}\left[e^{-\pi\frac{(t'+f_\beta\Delta t)^2}{\tau_c^2}} e^{-\pi\frac{(t'+\Delta t)^2}{\tau_c^2}} e^{i\omega_0(1-f_\beta)\Delta t}\right]\right\} \\ &= \frac{1}{2}\left\{1 - \left(\sqrt{\frac{2}{\tau_c^2}}\int \mathrm{d}t' e^{-\pi\frac{(t'+f_\beta\Delta t)^2}{\tau_c^2}} e^{-\pi\frac{(t'+\Delta t)^2}{\tau_c^2}}\right)\mathrm{Re}\left[e^{i\omega_0(1-f_\beta)\Delta t}\right]\right\} . \end{aligned} \tag{5.19}$$

We used the fact that, since the three Gaussian pulses are well-separatd by Δt, the temporal integration to obtain the probability of detection in the central peak can be extended up to the whole axis, by taking only the central wavepacket contribution.

By defining

$$\mathcal{V}(t) := \sqrt{\frac{2}{\tau_c^2}}\int \mathrm{d}t' e^{-\pi\frac{(t'+f_\beta\Delta t))^2}{\tau_c^2}} e^{-\pi\frac{(t'+\Delta t)^2}{\tau_c^2}} = e^{-2\pi\left[\frac{\Delta t}{\tau_c}\frac{\beta(t)}{1+\beta(t)}\right]^2}, \tag{5.20}$$

and

$$\varphi(t) := \omega_0(1-f_\beta)\Delta t = \frac{2\beta(t)}{1+\beta(t)}\omega_0\Delta t\,, \tag{5.21}$$

the probability $P_c(t)$ can be written as in (5.3), while (5.20) and (5.21) yield (5.4) and (5.5) respectively.

5.3 Results

Estimating the kinematic phase.—The value of $\varphi(t)$ originating from the satellite motion can be precisely predicted on the base of the sequence of measurements of the instantaneous distance of the satellite, or *range* r, which is realized in parallel via SLR, as described in Section 4.2.4. The range is measured by the strong SLR pulses at 10 Hz. Thanks to the atomic clock of MLRO, the SLR pulses are separated precisely by $\Delta T = 100$ ms and synchronized with the 100 MHz qubit pulses. By measuring the temporal separation $\Delta T'$ of the SLR pulses at the receiver after the satellite retroreflection, it is possible to determine the instantaneous satellite velocity relative to the ground station $v_r(t)$. Indeed, since by the Doppler effect we have that

$$\Delta T' = \frac{\Delta T}{f_\beta}\,, \tag{5.22}$$

the velocity $v_r(t)$ can be estimated as

$$v_r(t) = c\frac{\Delta T' - \Delta T}{\Delta T' + \Delta T}\,. \tag{5.23}$$

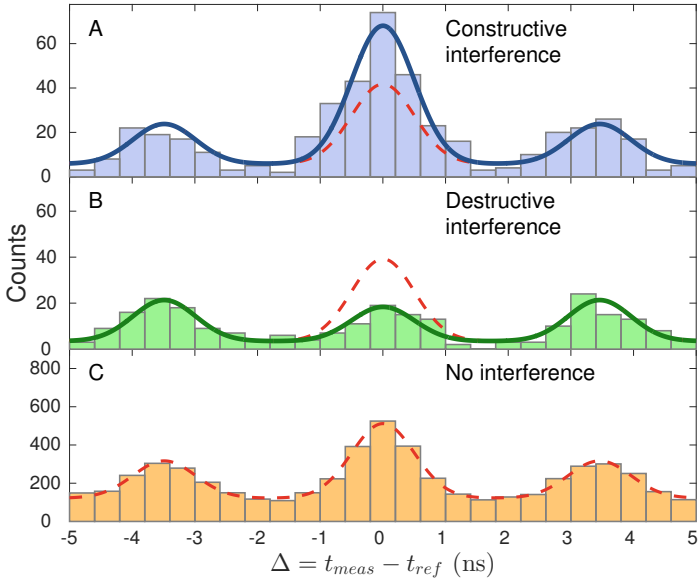

Figure 5.7: *Constructive and destructive single-photon interference* (Beacon-C satellite, 11.07.2015 h 1.33 CEST). **(A)** Histogram of single photon detections as a function of time $\Delta = t_{\text{meas}} - t_{\text{ref}}$ realized by selecting only the returns characterized by $\varphi \mod 2\pi \in [9\pi/10, 11\pi/10]$ that lead to constructive interference. Solid line shows the tri-Gaussian fit. By evaluating the Gaussian integrals we obtained the counts $N_\ell = 112 \pm 11$ for the sum of lateral peaks and $N_c = 196 \pm 14$ for the central one. **(B)** Histogram of single photon detections realized by selecting only the returns characterized by $\varphi \mod 2\pi \in [-\pi/10, \pi/10]$. Here $N_\ell = 112 \pm 11$ and $N_c = 46 \pm 7$. **(C)** Histogram of single photon detections without any selection on the phase. As expected, interference is completed washed out and we measured $N_c = 1245 \pm 35$ and $N_\ell = 1306 \pm 36$, fully compatible with $P_c = 1/2$. In all panels, dotted red lines represent the expected counts in case of no interference.

The separation $\Delta T'$ is related to the range r by $\Delta T' = \Delta T + \Delta r/c$, where Δr is the variation of the satellite distance between two subsequent SLR pulses. Then, by measuring the range every 100 ms, the instantaneous satellite velocity relative to the ground station $v_r(t)$ can be estimated, from which $\varphi(t)$ can be derived by (5.5). In the top panel of Figure 5.4, for a given passage of the Ajisai satellite, we show the measured satellite distance and the estimated $\varphi(t)$ as a function of time from the beginning to the end of the satellite tracking. Since $v_r(t)$ is continuously changing along the orbit, the value of $\varphi(t)$ is varying accordingly. In the bottom panel of Figure 5.4 we show the variation of the theoretical output probability $P_c(t)$ along the Ajisai orbit as predicted by (5.3).

Highlighting the single-photon interference.— We selected three satellites in low-Earth-orbit (LEO) – Beacon-C, Stella and Ajisai – which are equipped with efficient cube-corner retroreflectors (CCRs). Thanks to the CCR properties, the state $|\Psi_{\text{out}}\rangle$ is automatically redirected toward the MLRO ground station, where it is injected into the same MZI used in the uplink. By the synchronization technique described iin Section 4.2.4, we determined of the expected (t_{ref}) and the measured (t_{meas}) instant of arrival of each photon. In this way, the histogram of the detections in the temporal window of 10 ns between two consecutive pulses as a function of the temporal difference $\Delta = t_{\text{meas}} - t_{\text{ref}}$ can be obtained. In Figure 5.7

we show such histograms corresponding to constructive and destructive interference in the case of satellite Beacon-C.

In particular, for the constructive interference, Figure 5.7(A), we selected the detections corresponding to $\varphi \pmod{2\pi} \in [9\pi/10, 11\pi/10]$. For the destructive interference, Figure 5.7(B), we selected a kinematic phase $\varphi \pmod{2\pi} \in [-\pi/10, \pi/10]$. The detections in the central peak are respectively higher or lower than the sum of the two lateral peaks in the two cases. We note that the peak width is determined by the detector timing jitter which has standard deviation $\sigma = 0.5$ ns. These two histograms clearly show the interference effect in the central peak. On the contrary, Figure 5.7(C) is obtained by taking all the data without any selection on φ. In this case, the interference is completely washed out. These results show that, in order to prove the interference effect, it is crucial to correctly predict the kinematic phase φ imposed by the satellite motion.

By using the data of Figure 5.7, we experimentally evaluate the probability $P_c^{(\mathrm{exp})}$ as the ratio of the detections associated the central peak N_c to twice the sum N_ℓ of the detections associated to the side peaks, namely

$$P_c^{(\mathrm{exp})} = \frac{N_c}{2N_\ell}\,. \tag{5.24}$$

The values $P_c^{(\mathrm{exp})} = 0.87 \pm 0.10$ and $P_c^{(\mathrm{exp})} = 0.20 \pm 0.03$ are obtained for constructive and destructive interference respectively. The values deviates with clear statistical evidence from 0.5, which is the expected value in the case of no interference.

A more clear evidence of the role of $\varphi(t)$ can be demonstrated by evaluating the experimental probabilities $P_c^{(\mathrm{exp})}$ as a function of φ. Figure 5.8 shows $P_c^{(\mathrm{exp})}$ for ten different values of the kinematic phase φ and for the three different satellites. By fitting the data by $P_c^{(\mathrm{exp})} = \frac{1}{2}(1 - \mathcal{V}_{\mathrm{exp}} \cos\varphi)$, we estimated the experimental visibilities $\mathcal{V}_{\mathrm{exp}} = 67 \pm 11\%$ for Beacon-C, $\mathcal{V}_{\mathrm{exp}} = 53 \pm 13\%$ for Stella and $\mathcal{V}_{\mathrm{exp}} = 38 \pm 4\%$ for Ajisai. The data were collected at the following satellite distance ranges: from 1 600 to 2 500 km for Ajisai, from 1 100 to 1 500 km for Stella and from 1 200 to 1 500 km for Beacon-C, giving two-way channel lengths ranging from 2 200 up to 5 000 km. The interference patterns in Figure 5.8 clearly demonstrate that the coherence between the two temporal modes is preserved along these thousand kilometer scale channels with rapidly moving retroreflectors.

We attribute the different visibilities to residual vibrations of the unbalanced MZI between the upgoing and downgoing pulses, since the intrinsic visibility of the interferometer was measured to be above 95%. To improve the visibility it would be necessary to redesign the full interferometric setup to further mitigate this effect. We note that, in the double-pass configuration, the interferometer is sensitive to vibrations with frequencies

higher than 1/rtt (rtt is the round trip time). Indeed, the lower visibility is obtained with Ajisai, the satellite with larger distance from the ground (from 1 600 to 2 000 km), with a rtt between 10.7 ms and 16.7 ms. For the other two satellites the rtt is typically lower than 10 ms.

Probing the interference is at the single-photon level.—The mean number of photon μ in the received pulses may be derived by measuring the detection rate and from the optical losses $\eta \approx 0.27$ in the receiving setup, as described in Section 4.2.5. At the primary mirror of the receiving telescope, the average μ during the data acquisition are given by $\mu \approx 7{\cdot}10^{-4}$ for Beacon-C, $\mu \approx 2 \cdot 10^{-3}$ for Ajisai and $\mu \approx 9 \cdot 10^{-4}$ for Stella. From these values we may conclude that interference was probed at the single photon level. Indeed, the probability of having more that one photon per pulse in the receiver MZI is $\sim \eta\mu^2$.

We estimated that that the mean number of photons μ_{sat} leaving from the satellites are $\mu_{\text{sat}}^{(\text{Stella})} < 20$ and $\mu_{\text{sat}}^{(\text{Ajisai})} < 60$ (the instantaneous values fluctuate due to pointing error and turbulence). The technique used for the estimation of the μ_{sat} is not applicable for the Beacon-C satellite, due to the lack of data (it was launched on 1965). We note that its distance to the ground is similar to the Stella satellite and a similar μ_{sat} could be expected. Hence, the total downlink attenuation (including the detection setup losses) is between 60 dB and 70 dB.

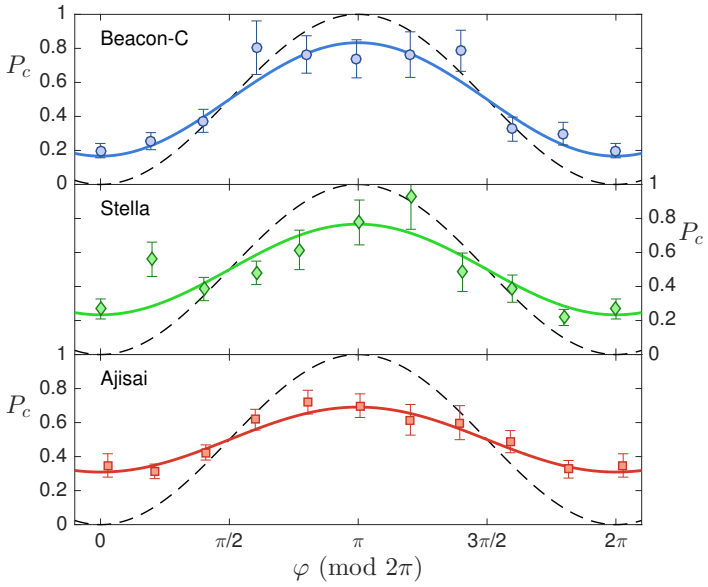

Figure 5.8: *Measured interference pattern.* Experimental probabilities $P_c^{(\text{exp})}$ as a function of the kinematic phase measured for three different satellites. By fitting the data we estimate the visibilities $\mathcal{V}_{\text{exp}} = 67 \pm 11\%$ for Beacon-C, $\mathcal{V}_{\text{exp}} = 53 \pm 13\%$ for Stella and $\mathcal{V}_{\text{exp}} = 38 \pm 4\%$ for Ajisai. Dashed lines correspond to the theoretical value of P_c predicted by eq. (5.3). The points are obtained by considering ten intervals of the phase defined by $I_j \equiv [\frac{2j-1}{10}\pi, \frac{2j+1}{10}\pi]\,(j = 0, \ldots, 9)$. For each interval we selected the data corresponding to $\varphi \mod 2\pi \in I_j$: from such data we determined the experimental probability of detection in the central peak $P_c^{(\text{exp})}$ and we averaged the corresponding phase φ. We note that at point $\varphi = 0$ and $\varphi = 2\pi$ the same subset of data were selected.

5.4 Future perspectives

In the work described in this chapter we observed interference at the single photon level between two temporal modes by exploiting a Space interferometer extending for thousands of kilometers. We demonstrated that the relative motion of the satellite with respect to the ground induces a varying phase that modulates the interference pattern. This varying phase is not present in the case of fixed terminals. The effect resulted from the measured interference pattern during passages of three satellites, Beacon-C, Stella and Ajisai, having different relative velocities and distances from the MLRO ground station.

Up to this work polarization encoding was the one exploited in long distance free-space quantum communications, time-bin encoding was never implemented a long-distance free-space channels, fearing that turbulence effects on the wavefront may spoil the interference. However, we demonstrated that the atmospheric turbulence is not detrimental for time-bin encoding in long distance free-space propagation if the two temporal modes are separated by a few nanoseconds. Indeed, they are identically distorted by the propagation in the turbulent air, whose dynamics is in the millisecond scale [127]: the key point is the careful matching of the interfering wavefronts in the two arms, obtained by using a double $4f$ optical system.

The interference patterns measured in the present experiment demonstrates that a coherent superposition between two temporal modes holds in the photon propagation and its interference can be indeed observed over very long channels involving moving terminals at fast relative velocity. The results here described attest the viability of the use of time-bin encoding for fundamental tests of Quantum Optics to be performed in Space, as we will present in the next chapter in our satellite realization of Wheeler' delayed-choice experiment [80].

Furthermore, the measurement of interference in Space is a milestone to investigate one of the big unresolved puzzle in Physics, namely the interplay of Quantum Theory with Gravitation. As recently proposed theoretically by M. Zych *et al.* [128, 64] (the optical version of the original Colella-Overhauser-Werner (COW) experiment realized with neutrons [129]), interference with single photons in Space is a witness of general relativistic effects: gravitational phase shift between a superposition of two photon wavepackets could be highlighted in the context of large distance Quantum Optics experiment. In the case of our setup, the gravitational shift for the Ajisai satellite corresponds to about 2 mrad (see equation (23) of [64]). We point out that, unlike the case of effects manifested by photon polarization rotation, such small gravitational effects may be enhanced by increasing the temporal separation of the two interfering modes. To reveal the effect of

gravity in Quantum Optics experiments several other proposals have been presented [64]: these include the exchange of elementary particles from moving and accelerated reference frames, which would allow to test Bell's inequalities and wavefunction collapse and possible gravity-induced decoherence [130] in laser interferometry with a long baseline.

Chapter 6

Extending Wheeler's delayed-choice experiment to Space

Gedankenexperiments have consistently played a major role in the development of quantum theory. A paradigmatic example is the *Wheeler's delayed-choice experiment*, a test of quantum *wave-particle duality* that cannot be fully understood using only classical concepts, like the Young's two-slit experiment. In this chapter we describe our implementation of Wheeler's idea along a satellite-ground interferometer which extends for thousands of kilometers in Space. We exploited both time-bin and polarization encodings of photons reflected by a fast moving satellite equipped with retro-reflecting mirrors. We observed the complementary wave-like or particle-like behaviours at the MLRO ground station by choosing the measurement apparatus while the photons are still propagating from the satellite to the ground. This experiment confirmed quantum mechanical predictions, demonstrating the need of the dual wave-particle interpretation, at this unprecedented scale. This work is the natural continuation of the works [84] and [89] described in the previous chapters. Some contents of this chapter are part of our work [80].

Pictorial representation of Wheeler's idea (by Elisabetta Vedovato).

6.1 The idea of the experiment

As discussed above, the recent developments of quantum communications in Space enable the investigation of the basic principles of Quantum Mechanics in a radically new scenario. These developments foster the implementation in Space of fundamental tests of Quantum Mechanics such as the gedankenexperiments which highlight the its counterintuitive aspects.

These thought experiments played a primary role in the famous debate between Einstein and Bohr [131], concerning the completeness of Quantum Mechanics [132, 133] and the concept of *complementarity* [134]. The most disturbing implication of complementarity is the wave-particle duality of quantum matter, that is the impossibility of revealing at the same time both the wave-like and particle-like properties of a quantum object. Bohr pointed out that it is necessary to consider the whole apparatus in order to determine which property is measured, stating that there is no difference "whether our plans of constructing or handling the instruments are fixed beforehand or whether we postpone the completion of our planning until a later moment" [131].

John Wheeler pushed this observation to the extreme and conceived his *delayed-choice Gedankenexperiment* [135, 136] to highlight the contradictory interpretation given by classical physics. In his idea, a photon emerging from the first beam-splitter (BS) of a Mach-Zehnder interferometer (see Figure 6.1) may find two alternative configurations. Given the presence or absence of a second BS at the output of the interferometer, the apparatus measures the wave-like or particle-like character of the photon. Indeed, if the BS is absent both detector can fire with 50% probability, reflecting the fact that the photon traveled along only one arm of the interferometer and revealing *which-path* it took, as a classical particle would have done. If the BS is present, *interference* depending of the phase-difference between the two arms can be observed, as explained in Section 2.1.2, reflecting the fact that the photon travelled both routes, as a classical wave would have done.

A naive interpretation of such experiment in which the photon decides how to behave at the entrance in the interferometer is allowed by classical physics. However, if the configuration is chosen after the entrance of the photon into the interferometer, a purely classical interpretation of the process in which the photon decides its nature at the first BS would imply a seeming violation of causality [126], since the photon may change its behaviour while passing through the interferometer, while having already decided its nature at the entrance. On the other hand, in the quantum mechanical interpretation of the experiment, the photon maintains its dual wave-particle nature until the very end of the experiment, when it is detected.

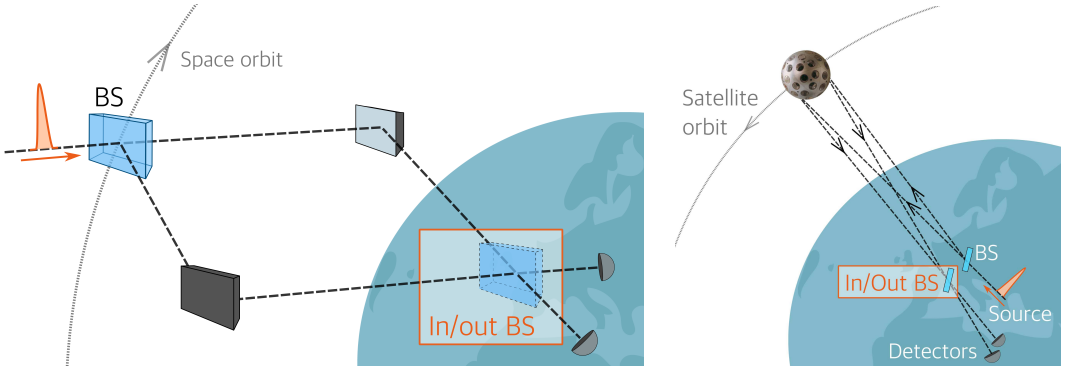

Figure 6.1: **(left panel)** A photon wavepacket enters the first beam splitter of an interferometer which extends along thousands of kilometers in Space. The interferometer can be randomly arranged according to two configurations that correspond to the presence or absence of the second beam splitter (In/Out BS) located on Earth. Following Wheeler's idea, the configuration choice is performed when the photon has already entered the interferometer. **(right panel)** In our actual implementation, the interferometer begins and terminates on the ground, extending up to the target satellite, and the measurement choice performed on ground is space-like separated from the photon reflection by the satellite. In our experiment, the two paths of the interferometer are represented by two time-bins, each with orthogonal polarization.

So far, several implementations of Wheeler's experiment have been realized on the ground (see the work by Jacques *et al.* [137] for the realization closest to the original idea and the paper by Ma *et al.* [138] for a interesting review). An alternative way of interpreting the delayed choice experiment is within the *quantum-erasure* framework [139, 140]. Furthermore, a quantum delayed choice version of the experiment, where a quantum ancilla controls the second BS, has been recently proposed [141] and realized [142, 143, 144]. Thanks to the availability of the Space interferometer described in the previous chapter, we extended the delayed-choice paradigm to Space, as sketched in Figure 6.1, by combining both time-bin and polarization encodings in our two-way scheme at MLRO[1].

6.2 Description of the experiment

6.2.1 The optical setup

In this experiment the key ingredients of the Quantum Optics setup of Figure 4.4 are a polarization-based unbalanced Mach-Zehnder interferometer (MZI) followed by a switchable half-waveplate (sHWP) set by a Quantum Random Number Generator (QRNG), as sketched Figure 6.2. The combined action of the first polarizing beam splitter (MZI-PBS) and of the unbalance of the MZI transforms each qubit pulse into a superposition of two temporal and polarization modes. In fact, the long arm of the MZI is traveled by the

[1]A nice video explaining Wheeler's experiment and our implementation is available (here) from the Quantum Future website. Many thanks to my sister Elisabetta for the video-making.

vertically polarized component of the beam while the horizontally polarized component travels along the short arm.

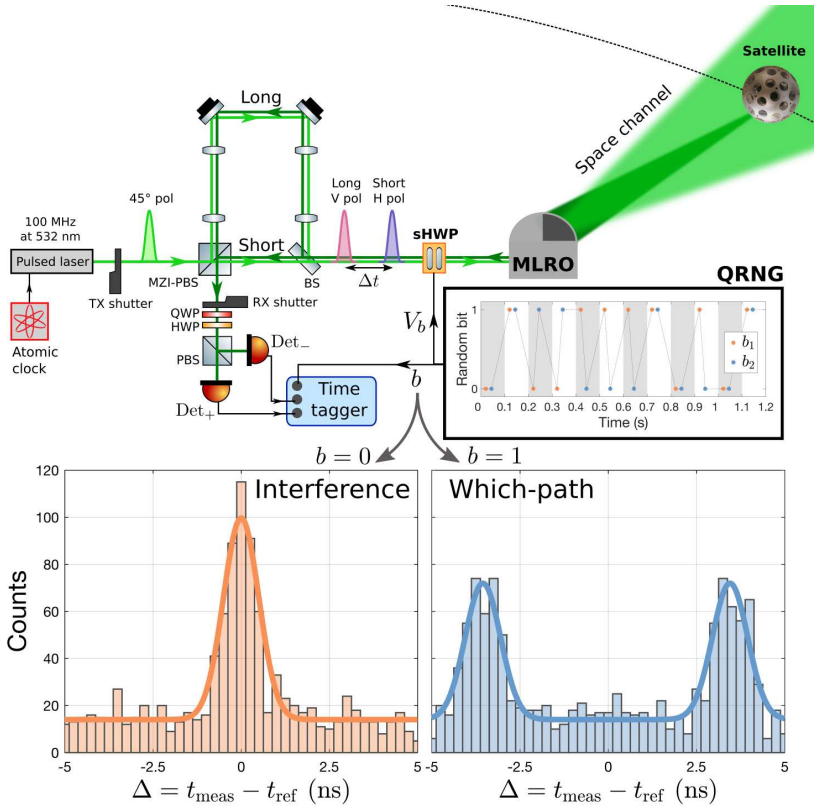

Figure 6.2: *Scheme of the experimental setup and detection histograms.* A pulsed laser synchronized with the MLRO atomic clock exits the MZI in two temporal and polarization modes. The sHWP leaves the pulses unperturbed and the telescope directs the beam to a target satellite. After the reflection, the photons are collected at the ground by the same telescope and injected into the optical table. The photons pass through the sHWP whose behavior is set according to the bit b extracted from an on-demand QRNG. The QRNG is inquired twice in each 100-ms cycle of the experiment, as detailed in the text. In the inset, a 1-s sample of the extracted bits is shown. At the MZI output, two waveplates, a PBS and two single photon detectors perform a polarization measurement in the $\{|D\rangle, |A\rangle\} \equiv \{|+\rangle, |-\rangle\}$ basis. According to the value b of the random bit, interference or which-path measurement is performed, as shown by the detection histograms for a passage of the Starlette satellite. The counts in the central peak on the left histogram are comparable to the sum of the counts associated to the lateral peaks on the right one, as expected.

The separation between the two temporal modes is about $\Delta t \approx 3.5$ ns. We precisely measured Δt by sending the pulsed train through it and using the SPAD by MPD in one of the beam-splitter output port. As expected, the detections appear at two different times in two well separated peaks. Each peak is characterized by a exponentially modified Gaussian distribution whose standard deviation is of the order of 40 ps (due to the timing jitter of the detector and the pulse duration). By fitting the distribution we estimate the unbalance of the MZI as $\Delta t = 3.498 \pm 0.002$ ns.

The pulses then pass through two liquid crystal retarders (LCRs) whose combined action is equivalent to a single switchable (**on/off**) half waveplate (sHWP) inclined at 45° with respect to the horizontal axes. The two LCRs are mounted with orthogonal

axes. Each LCR introduces a phase retardance Γ between the two orthogonal polarization modes of the impinging light, which is dependent on the applied voltage V_a. We characterized the two LCRs by measuring the birefringence introduced as a function of the applied voltage $\Gamma = \Gamma(V_a)$, see Figure 6.3 and then designed the two sHWP to act as a single fast switching HWP inclined at 45°. With this configuration, we obtain a switching time $t_{\text{sHWP}} \lesssim 500\ \mu$s.

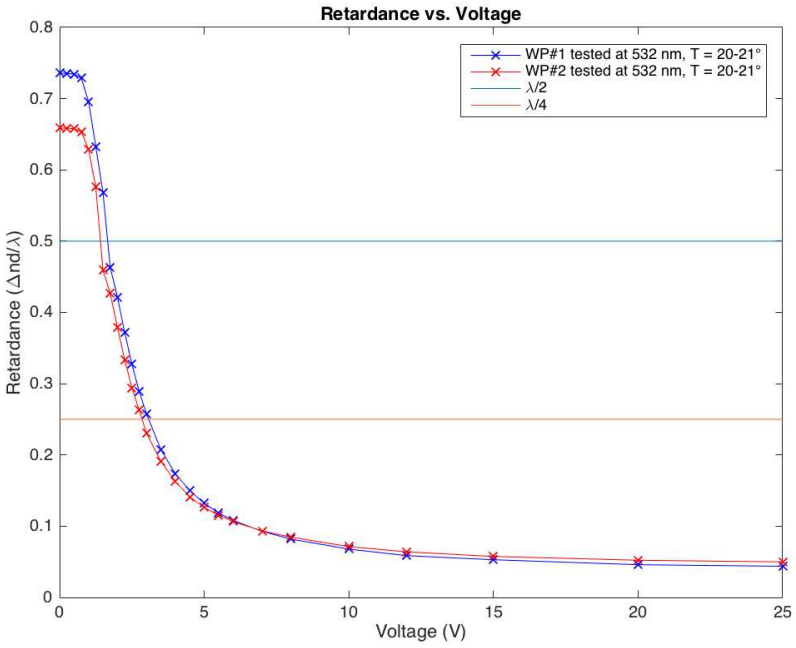

Figure 6.3: Retardance Γ as a function of the applied voltage V_a for the two LCRs.

During the transmission period, the sHWP is always **off**, leaving the outgoing beam unperturbed. The light is then directed to a target satellite equipped with polarization maintaining corner-cube retroreflectors via the MLRO telescope. The corner cubes of the target satellite redirect the beam back to the ground station. As in the interference experiment of the previous chapter, the radial motion of the satellite introduces a kinematic phase shift $\varphi(t)$ between the two time-bins given by (5.5). The photons returning from the satellite are collected by the same MLRO telescope and injected into the optical table where they re-encounter the same sHWP and the MZI. At an exit port of the MZI-PBS, we perform a polarization measurement in the diagonal and anti-diagonal basis $\{|D\rangle, |A\rangle\} \equiv \{|+\rangle, |-\rangle\}$, by using a QWP (to compensate for the additional phase-shift introduced by the imperfect beam spliters) and a HWP, as described in Section 2.2.2.

While the photons are propagating back to MLRO, a QRNG extracts a random bit $b \in \{0, 1\}$ with 50:50 probability. The QRNG is based on differences of the times of arrival

of single photons in attenuated light [145], and its relevant features will be detailed in the following. The bit value sets the voltages V_b applied to the LCRs, determining the **on** or **off** behavior of the sHWP. The latter determines whether we perform a measurement that reveals the particle-like (sHWP **on**) or wave-like (sHWP **off**) behavior of the photons returning from the satellite. Since the random bits are generated while the photons are traveling from the satellite to the ground station, we ensure a space-like separation between the measurement choice and the last interaction with the apparatus, i.e. the reflection by the satellite, as detailed in the following.

Let us first suppose that the QRNG extracts a $b = 0$ bit causing the sHWP to remain **off**, leaving the polarization of the photon unchanged as it re-enters the MZI. At the exit port of the MZI-PBS towards the detectors in Figure 6.2, only the horizontally polarized component that propagated through the long arm and the vertically polarized component that traveled along the short arm can be detected. Since this is the reverse situation compared to the outward passage through the MZI, the two polarization modes will recombine into a single temporal mode, loosing all which-path information and allowing us to observe the φ-dependent interference due to satellite motion, which is the fingerprint of the wave-like nature of the photon. Indeed, in this case the probabilities of a click in the detectors labelled $\mathrm{Det}_\pm$ are given by

$$P_\pm^{b=0}(t) = \frac{1}{2}[1 \pm \mathcal{V}(t)\cos\varphi(t)] \tag{6.1}$$

where $\mathcal{V}(t) \approx 1$ is the theoretical visibility as in (5.4) and $\varphi(t)$ is the kinematic phase introduced at the satellite reflection as in (5.5).

Let us now suppose that the QRNG extracts a $b = 1$ bit, switching the sHWP **on** and swapping the horizontal and vertical polarizations before the photon re-enters the MZI. The polarization transformation causes each component of the state to re-travel along the same arm compared to the outwards passage through the MZI. As a result, the photon can be detected at two distinct times separated by $2\Delta t$, with 50% probability for each detector $\mathrm{Det}_\pm$, i.e.

$$P_\pm^{b=1}(t) = \frac{1}{2}\,, \tag{6.2}$$

giving which-path information and evidencing the particle nature of the photon.

6.2.2 Implementation of the delayed-choice

Timing of the experiment.—A faithful realization of Wheeler's experiment requires that the entrance of the photon in the interferometer is not in the future light-cone of the

measurement choice. Moreover, the latter must be realized in a random manner: this prevents any causal influence of the measurement choice on the behavior of the photon.

Our implementation is performed over a Space channel with length of the order of thousands of kilometers, corresponding to a round trip time (rtt) of the order of 10 ms. We designed the experiment to guarantee that the choice of the measurement apparatus is space-like separated from the reflection of the photon from the satellite, as shown in the Minkowski diagram [125] of Figure 6.4. This guarantees that, in a purely classical interpretation, a photon "should have decided its nature" at most at the reflection by the satellite.

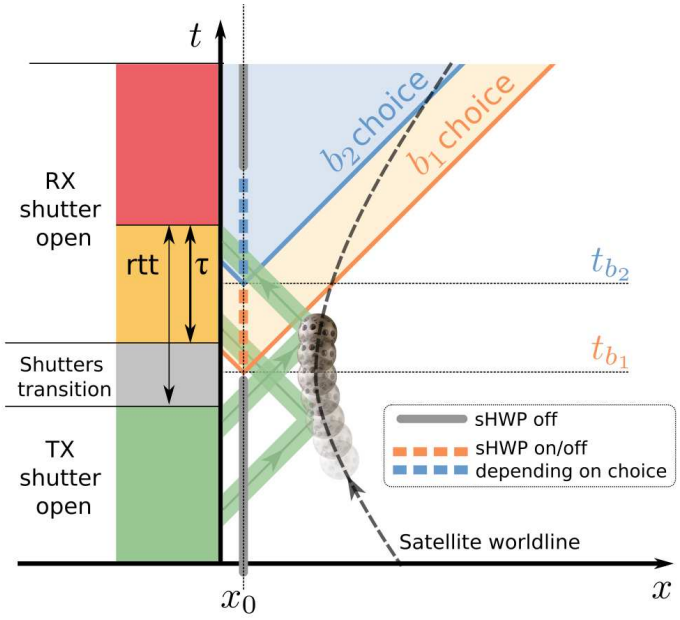

Figure 6.4: *Minkowski diagram of the experiment.* Along the temporal axis (not to scale) a 100 ms cycle between two SLR pulses is represented. The x-axis represents the radial coordinate (not to scale) from the detectors, where x_0 is the position of both the switchable HWP and the QRNG. The dotted line is the satellite worldline. As detailed in the main text, we only considered the detections in the temporal window τ. A fast FPGA controller synchronized in real time with the MLRO tracking system drives the two shutters and the QRNG. For each cycle, we perform two independent measurements via the random bit extracted by the QRNG at times t_{b_1} and t_{b_2}, causally disconnected from the photon reflection at the satellite. The cycle is repeated for each 100 MHz train between two SLR pulses.

For each 100-ms cycle between two strong SLR pulses, we performed two independent choices that will affect the detections in the acceptable temporal window τ (see Section 4.2.4) by driving the QRNG with the same FPGA controller used for the shutters. The sHWP behavior at the photon return is set according to the bits b_1 and b_2 extracted by the QRNG. The first choice is performed at t_{b_1}, corresponding to the middle of the shutter transition phase.

The second choice is at t_{b_2}, which occurs with a delay rtt/2 with respect to the first choice. The detected photons are divided into two groups, each characterized by a value

of the bit choice. In this way, all the photons of a given group were already reflected by the satellite when the corresponding bit choice was performed.

Details of the QRNG.—The QRNG device generates random numbers on demand by using a protocol based on the differences of the times of arrival of single photons in attenuated light [145]. This protocol requires a light source (a light-emitting diode in our case) attenuated to single-photon level and only one single photon detector (SPD). The device was realized with the FPGA technology for a full control over the time evolution of the generation process and for the integration with the data acquisition at MLRO. As described in the main text, our implementation of Wheeler's experiment requires two random bits b_1 and b_2 at specific times t_{b_1} and t_{b_2} (separated by rtt/2) to set the sHWP in each 100-ms cycle. Because the QRNG has an average latency in the random bit generation of about 20 ms and the sHWP requires $\sim$ 500 ms at most to change its state, the setup guarantees that the time from the inquiry of the QRNG to the generation of the random bit and the subsequent setting of the sHWP is much shorter than rtt/2. In the experiment, we used two identical QRNG setups (two light sources, two SPDs, and two FPGA architectures) and combined the two outputs with an XOR operation to extend the total entropy value and add robustness to the design. The QRNG final bit stream has a bias value (10^{-4} in a 100-megabit string) and correlation values of the first 100 lags between -2.5×10^{-4} and 2.5×10^{-4}. These values fulfil the statistical requirements for high-quality on-demand QRNG, guaranteeing the randomness of the output bits. The timing of the experiment ensures the required relativistic space-like separation between the bit extraction and the photon reflection at the satellite, as described previously.

6.3 Results

We selected the passages of two low-Earth-orbit (LEO) satellites equipped with polarization maintaining corner-cube retroreflectors, namely Beacon-C (with slant distance ranging from 1 264 to 1 376 km with respect to the MLRO Observatory) and Starlette (with slant distance ranging from 1 454 to 1 771 km).

The synchronization between our signal and the bright laser ranging pulses allowed us to predict the expected time of arrival t_{ref} of the photons, which is not periodic along the orbit due to the satellite motion. The effective time of arrival t_{meas} was tagged by a time-to-digital converter (time-tagger of Figure 6.2). Therefore, we may obtain a detection histogram as a function of the time difference $\Delta = t_{\text{meas}} - t_{\text{ref}}$, as shown in the bottom panel of Figure 6.2 for the data recorded in the Det_ detector in the passage of the Starlette satellite (results for the Det_+ are analogous).

As previously described, we separated the detections in two groups according to the setting of the sHWP. In Figure 6.2, on the left histogram, we gathered all the detections characterized by the bit value $b = 0$ and we obtain a single central peak where which-path information is erased and the interference effects should be observed. The peak width is determined mostly by the timing jitter of the detector which is about 0.5 ns RMS. On the right histogram, the extracted bit b was equal to 1, and we obtain a histogram with two well separated lateral peaks, manifesting the expected particle-like behavior. An indication of good assessment for the setup is given by the fact that the peak obtained when $b = 0$ is comparable with the sum of the two lateral peaks obtained when $b = 1$, as the number of "0" and "1" bits from the QRNG is balanced. We note that, even if interference is expected in the $b = 0$ case, it is not apparent in Figure 6.2, since we are not taking into account the phase shift $\varphi(t)$ introduced by the satellite, and thus the interference effect is completely averaged over all the data.

To evaluate the role of the kinematic phase $\varphi(t)$, these two data sets were further separated into ten phase intervals of length $\pi/5$ rads and defined by

$$I_j \equiv [(2j-1)\pi/10, (2j+1)\pi/10] \tag{6.3}$$

with $j = 0, \ldots, 9$, as in the analysis of the work described in the previous chapter. For each phase interval we selected the detection events characterized by $\varphi \pmod{2\pi} \in I_j$. Then, for each selected data set we evaluated the detection histogram as a function of the time difference Δ, as described above.

These histograms were used to determine the photon counts $N_\pm = N_\pm(I_j)$ for each phase interval I_j by taking all the events recorded by $\mathrm{Det}_\pm$ in a precise detection window centered at the expected arrival time of the photon. The width of the detection window (0.9 ns) was chosen to optimize the trade-off between signal-to-noise ratio and count rate. From the counts, we calculated the relative detection frequency

$$f_\pm = \frac{\eta_\mp N_\pm}{\eta_- N_+ + \eta_+ N_-}\,, \tag{6.4}$$

where $\eta_+ = 0.12$ and $\eta = 0.10$ account for the different quantum efficiencies of the detectors used. The resulting relative frequencies $f_\pm$ and their Poissonian errors are plotted in Figure 6.5 for the two satellites.

For the "interference" subset of the data we may observe the relative phase information by erasing the photon's "which-path" information. This is evident by the recovery of the interference pattern shown in the left part of Figure 6.5. By fitting the data with $P_\pm = (1 \pm \mathcal{V}_{\mathrm{exp}} \cos\varphi)/2$ given by (6.1), we obtained an experimental visibility value $\mathcal{V}_{\mathrm{exp}} \approx 40\%$

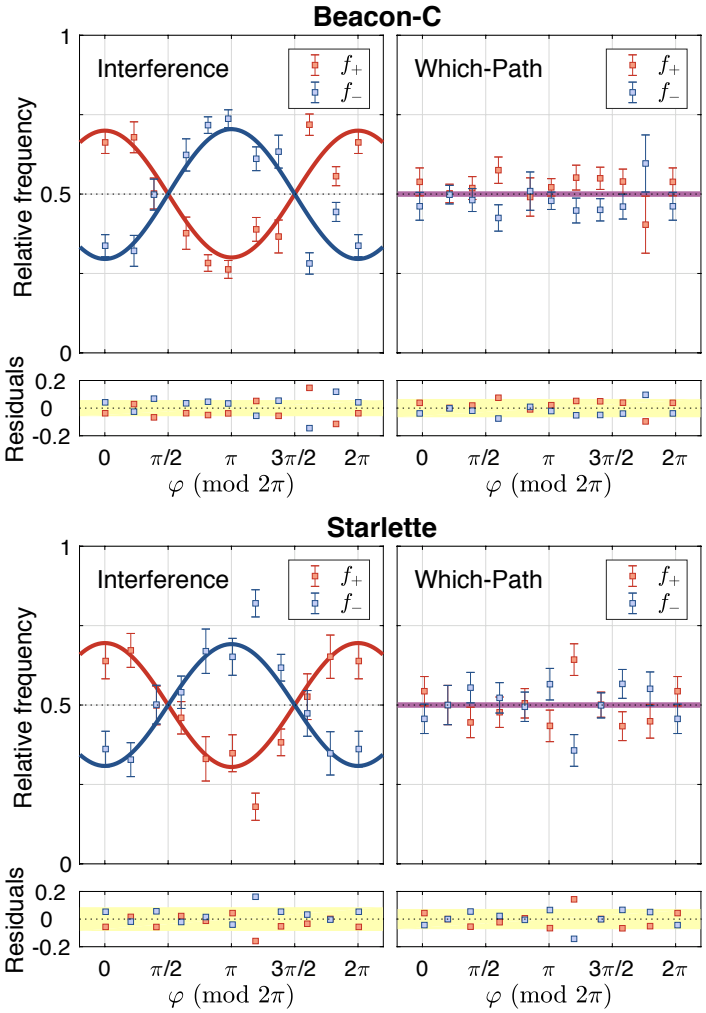

Figure 6.5: *Experimental results for the interference and which-path configurations.* Relative frequencies $f_\pm$ of counts in the two detectors $\mathrm{Det}_\pm$ as a function of the kinematic phase φ introduced by the satellite for the passages of Beacon-C and Starlette satellites. The error bars are estimated using the Poissonian error associated to counts. Below each plot we show the relative residuals as a function of φ. We note that at the point $\varphi \approx 0$ and $\varphi \approx 2\pi$ the same subset of data was selected. In the "interference" configuration, we estimated from the fitted data a visibility $\mathcal{V}^{\mathrm{B}} = 41 \pm 4\%$ for Beacon-C and $\mathcal{V}^{\mathrm{S}} = 40 \pm 4\%$ for Starlette.

for both satellites and a clear phase dependent modulation in the two detector outcomes. Furthermore, the visibility obtained during preliminary tests where the sHWP was fixed in the **off** mode, is compatible with the results obtained while performing the delayed choice, attesting that the latter had no influence in the observed interference pattern. The value of the experimental visibility, lower than the theoretical value of 100%, is due to experimental imperfections in the MZI and to residual birefringence caused by the Coudé path of the telescope.

On the other hand, the "which-path" relative frequencies are constant (within statistical fluctuations) for all values of φ, as predicted by the theoretical model $P_\pm = 0.5$. In this case, the "which-path" measurement destroys any information about the relative phase of the two time-bins.

When the photon's particle-like nature is inquired, we obtain conclusive which-path information with probability $p_{\text{wp}} = 88 \pm 1\%$ ($86 \pm 1\%$) for Beacon-C (Starlette). Such values are obtained by the ratio between the counts in the lateral peaks and the total ones: indeed, when the photon is detected in one of the two lateral peaks, *which-path* information is recovered. Since classical particles should always give complete which-path information, we could naively conclude that our photons behave as classical particles at least 86% of the time. If such interpretation were correct then we would expect interference with at most 14% visibility when the photon's wave-like nature is inquired. This is in remarkable contrast with the measured visibility, which is at least 5σ distant from that prediction, allowing us to exclude any model where the photon behaves as a purely classical particle.

The agreement between the theoretical model and the obtained results can be assessed by calculating the residuals between the fit and the experimental data. From Figure 6.5, we can observe that these residuals are randomly distributed within the foreseeable Poissonian fluctuations: indeed most points lay within $\pm 1.5\sigma$ from the expected values, where σ is the mean error. This can also be seen by calculating the root mean square of the residuals $\sigma_R \sim 0.05$ for both satellites, which is compatible with the expected statistical fluctuations.

Given the optical losses $\eta_{\text{opt}} = 0.13$ in the receiving setup and the detection efficiency $\eta_{\text{det}} = 0.1$, the mean number of photons μ in the received pulses can be derived by measuring the detection rate. At the primary mirror we received $\mu \approx 2.2 \times 10^{-3}$ for Starlette and $\mu \approx 1.9 \times 10^{-3}$ for Beacon-C. From these values we can conclude that the particle and wave-like properties are measured at the single photon level since the probability of having more than one photon per pulse passing through the MZI on the way back is $\sim \mu^2$, that is at most of the order of 10^{-6}.

6.4 Discussion

We realized Wheeler's *delayed-choice Gedankenexperiment* along a Space channel involving LEO satellites by combining two independent degrees of freedom of light. The experimental arrangement that allows the measurement of the complementary wave or particle behaviors of light quanta was randomly set according to two alternative configurations while the photons were already inside the apparatus, as required in the delayed-choice paradigm. In order to measure interference with the first configuration, it is crucial to take into account the kinematic phase-shift introduced by the satellite motion. By observing single-photon interference after the propagation along a 3 500 km Space channel, we can confute with clear statistical evidence of 5σ the description of light quanta as classical particles. In the alternative configuration of the detection scheme, the phase-

dependent modulation in the received clicks disappears, and the which-path information can be clearly reconstructed.

The high losses in the two-way propagation between the ground station and the satellite hampers the realization of this implementation scheme for the delayed-choice experiments using entangled particles, such as delayed-choice quantum erasure and entanglement swapping [146]. These experiments, already demonstrated on ground [138, 144, 147], require an active source on a satellite for the implementation in the Space scenario.

Our results extend the validity of the quantum mechanical description of complementarity to the spatial scale of LEO orbits. Furthermore, they support the feasibility of efficient encoding by exploiting both polarization and time-bin for high-dimensional free-space quantum key distribution [148] over long distances. Finally, our work paves the way for satellite implementation of other foundational-like tests and applications of quantum mechanics involving hyperentangled states [149, 150, 151] *around the planet and beyond*[2].

Two photos of the MLRO telescope tracking satellites (thanks to Daniele Dequal and Marco Tomasin).

[2]It is worth noticing that our three works [84, 89, 80] end with the same formula, to reinforce the inspiration from which they moved: the incredible beauty of quantum theory, which plays for us the same role the stars played for Dante [152].

Conclusions

In this thesis, I presented the work performed during my PhD. I focused on the activities which ended up in a peer-reviewed publication, as [21, 62, 63, 80, 89], presenting them in a coherent way. I had the possibility to work with state-of-the-art quantum technologies, ranging from different sources of entangled photons and CW- or pulsed-lasers, to modern systems of photon detection and temporal tagging. I manipulated both polarization and time-bin encodings, in experiments focused both on the technological advancement of quantum technologies, as the possibility of QKD with GNSS terminals and quantum satellites (Chapter 4), and on fundamental aspects of quantum theory, as the experimental realization of a Bell's test of local-realistic theories (Chapter 3), single-photon Space interferometry (Chapter 5) and the wave-particle duality though-experiment of Wheeler (Chapter 6).

Here, I summarize the main results of this thesis. In Chapter 3, I reported on the realization of a time-bin entanglement source which is free of the post-selection loophole. Such issue undermined the previous implementations of time-bin entanglement, in particular from the point of view of cryptographic applications. We obtained a clear violation of the Bell-CHSH inequality with our scheme, demonstrating its applicability. Further developments coming from our work may lead to the first loophole-free Bell's test realized with time-bin entanglement.

In Chapter 4, I focused on our last results obtained in the context of Space quantum communications. I reported, in particular, on the photon exchange realized with a terminal of the Russian GNSS constallation Glonass. This work demonstrates that Space quantum communications with discrete encoding, like polarization, may be feasible even at such distances, thus opening the possibility to exploit the long communication window given by high-orbit satellites. Moreover, I reported on the preliminary results obtained with a passage of the Chinese satellite Micius, which sent toward MLRO a strong polarized signal. Such results make MLRO, with little improvements, a candidate receiver of a world-wide network dedicated to quantum communications.

In Chapter 5, I reported on the first experiment exploiting time-bin encoding for satellite quantum communications. We were able to measure interference at the single-photon level (with 67% of visibility) after the two-way trip of a pulsed beam sent from the ground, reflected by a moving satellite and finally collected at the ground. This intererometric

technique may be exploited to overcome the first-order Doppler effect which makes the optical version of the COW experiment [64] not feasible. We are currently working on a proposal (see Ref. [153]) aimed at implementing a Doppler cancellation mechanism which can highlight the weak gravitational contribution in long-distance interferometric experiments. The goal of such proposal is to bound a possible violation of the Einstein Equivalence Principle [126], which sets the connection between geometry and gravitation, in the electromagnetic sector of the Standard Model.

In Chapter 6, I reported on the satellite realization of the Wheeler's delayed-choice experiment. We successfully adapted the interferometric scheme developed in Chapter 5 to implement Wheeler's idea over the unprecedented distance of thousands of kilometers. Such a work demonstrates that experiments testing the foundations of Quantum Mechanics can be performed out of labs, in particular in Space, without the needing of dedicated satellites in orbits.

The last three years were full of hard work, problems, but also of incredible satisfaction, thank to the great team I had the possibility to work with. However, such a work is not finished: many other ideas could be envisaged and fascinating experiments could be realized in the next future, thanks to the great advancement of satellite quantum technologies, ranging from secure communications at the global scale to new experiments testing gravitational effects on quantum particles over large distances. I am very proud to have participated in these efforts, and I hope to take part in this great scientific challenge even in the next future.

The *QuantumFuture* team at University of Padova (2018).

Bibliography

[1] L. D. Landau, E. M. Lifshitz, *Quantum Mechanics, Non-relativistic Theory*, Pergamon Press (1977)

[2] C. Cohen-Tannoudji, B. Diu, F. Laloe, *Quantum Mechanics, Volume 1*, Wiley-VCH (1991)

[3] C. Cohen-Tannoudji, B. Diu, F. Laloe, *Quantum Mechanics, Volume 2*, Wiley-VCH (1991)

[4] A. Peres, *Quantum Theory: Concepts and Methods*, Kluwer Academic Publishers (1993)

[5] J. J. Sakurai, J. J. Napolitano, *Modern Quantum Mechanics (2nd Edition)*, Pearson (2010)

[6] M. A. Nielsen, I. L. Chuang, *Quantum Computation and Quantum Information: 10th anniversary edition*, Cambridge University Press (2011)

[7] J. S. Bell, *On the Einstein Podolsky Rosen paradox*, Physics **1**, 195 (1964)

[8] N. Brunner, D. Cavalcanti, S. Pironio, V. Scarani, and S. Wehner, *Bell nonlocality*, Rev. Mod. Phys. **86**, 419 (2014)

[9] J. F. Clauser, M. A. Horne, A. Shimony, R. A. Holt, *Proposed Experiment to Test Local Hidden-Variable Theories*, Phys. Rev. Lett. **23**, 880 (1969)

[10] R. Loudon, *The Quantum Theory of Light, Third Edition*, Oxford University Press (2000)

[11] R. J. Glauber, *Quantum theory of optical coherence: selected papers and lectures*, Wiley-VCH (2007)

[12] C. Gerry, P. Knight, *Introductory Quantum Optics*, Cambridge University Press (2005)

[13] P. Kok, B. W. Lovett, *Introduction to Optical Quantum Information Processing*, Cambridge University Press (2010)

[14] B. E. A. Saleh, M. C. Teich, *Fundamentals of Photonics*, Wiley (2007)

[15] V. Scarani, H. Bechmann-Pasquinucci, N. Cerf, M. Dušek, N. Lütkenhaus, and M. Peev, *The security of practical quantum key distribution*, Rev. Mod. Phys. **81**, 1301 (2009)

[16] J. Skaar, J. C. García Escartín, H. Landro, *Quantum mechanical description of linear optics*, Am. J. Phys. **72**, 1385-1391 (2004)

[17] G. Vallone, P. Mataloni, *Generation and Applications of n-Qubit Hyperentangled Photon States*, Advances In Atomic, Molecular, and Optical Physics **60**, 291-314 (2011)

[18] P. Kolenderski, W. Wasilewski, K. Banaszek, *Modeling and optimization of photon pair sources based on spontaneous parametric down-conversion*, Phys. Rev. A **80**, 013811 (2009)

[19] P. G. Kwiat, E. Waks, A. G. White, I. Appelbaum, and P. H. Eberhard, *Ultrabright source of polarization-entangled photons*, Phys. Rev. A **60**, R773(R) (1999)

[20] P. G. Kwiat, K. Mattle, H. Weinfurter, A. Zeilinger, A. V. Sergienko, and Y. Shih, *New High-Intensity Source of Polarization-Entangled Photon Pairs*, Phys. Rev. Lett. **75**, 4337 (1995)

[21] F. Vedovato, C. Agnesi, M. Tomasin, M. Avesani, J.-Å. Larsson, G. Vallone, and P. Villoresi, *Postselection-Loophole-Free Bell Violation with Genuine Time-Bin Entanglement*, Phys. Rev. Lett. **121**, 190401 (2018)

[22] J. D. Franson, *Bell inequality for position and time*, Phys. Rev. Lett. **62**, 2205 (1989)

[23] Z. Y. Ou, X. Y. Zou, L. J. Wang, L. Mandel, *Observation of nonlocal interference in separated photon channels*, Phys. Rev. Lett. **65**, 321 (1990)

[24] J. Brendel, E. Mohler, W. Martienssen, *Experimental Test of Bell's Inequality for Energy and Time*, Europhys. Lett. **20**, 575 (1992)

[25] P. G. Kwiat, A. M. Steinberg, R. Y. Chiao, *High-visibility interference in a Bell-inequality experiment for energy and time*, Phys. Rev. A **47**, R2472(R) (1993)

[26] J. Brendel, N. Gisin, W. Tittel, H. Zbinden, *Pulsed Energy-Time Entangled Twin-Photon Source for Quantum Communication*, Phys. Rev. Lett. **82**, 2594 (1999)

[27] P. R. Tapster, J. G. Rarity, P. C. M. Owens, *Violation of Bell's Inequality over 4 km of Optical Fiber*, Phys. Rev. Lett. **73**, 1923 (1994)

[28] W. Tittel, J. Brendel, H. Zbinden, N. Gisin, *Violation of Bell Inequalities by Photons More Than 10 km Apart*, Phys. Rev. Lett. **81**, 3563 (1998)

[29] W. Tittel, J. Brendel, N. Gisin, H. Zbinden, *Long-distance Bell-type tests using energy-time entangled photons*, Phys. Rev. A **59**, 4150 (1999)

[30] I. Marcikic, H. de Riedmatten, W. Tittel, H. Zbinden, M. Legré, N. Gisin, *Distribution of Time-Bin Entangled Qubits over 50 km of Optical Fiber*, Phys. Rev. Lett. **93**, 180502 (2004)

[31] T. Inagaki, N. Matsuda, O. Tadanaga, M. Asobe, H. Takesue, *Entanglement distribution over 300 km of fiber*, Opt. Express **21**, 23241 (2013)

[32] W. Tittel, J. Brendel, H. Zbinden, N. Gisin, *Quantum Cryptography Using Entangled Photons in Energy-Time Bell States*, Phys. Rev. Lett. **84**, 4737 (2000)

[33] N. Gisin, G. Ribordy, W. Tittel, H. Zbinden, *Quantum cryptography*, Rev. Mod. Phys. **74**, 145 (2002)

[34] B. Hensen, H. Bernien, A. E. Dréau, A. Reiserer, N. Kalb, M. S. Blok, J. Ruitenberg, R. F. L. Vermeulen, R. N. Schouten, C. Abellán, W. Amaya, V. Pruneri, M. W. Mitchell, M. Markham, D. J. Twitchen, D. Elkouss, S. Wehner, T. H. Taminiau, R. Hanson, *Loophole-free Bell inequality violation using electron spins separated by 1.3 kilometres*, Nature **526**, 682-686 (2015)

[35] M. Giustina, M. A. M. Versteegh, S. Wengerowsky, J. Handsteiner, A. Hochrainer, K. Phelan, F. Steinlechner, J. Kofler, J.-Å. Larsson, C. Abellán, W. Amaya, V. Pruneri, M. W. Mitchell, J. Beyer, T. Gerrits, A. E. Lita, L. K. Shalm, S. W. Nam, T. Scheidl, R. Ursin, B. Wittmann, A. Zeilinger, *Significant-Loophole-Free Test of Bell's Theorem with Entangled Photons*, Phys. Rev. Lett. **115**, 250401 (2015)

[36] L. K. Shalm, E. Meyer-Scott, B. G. Christensen, P. Bierhorst, M. A. Wayne, M. J. Stevens, T. Gerrits, S. Glancy, D. R. Hamel, M. S. Allman, K. J. Coakley, S. D. Dyer, C. Hodge, A. E. Lita, V. B. Verma, C. Lambrocco, E Tortorici, A. L. Migdall, Y. Zhang, D. R. Kumor, W. H. Farr, F. Marsili, M. D. Shaw, J. A. Stern, C. Abellán, W. Amaya, V. Pruneri, T. Jennewein, M. W. Mitchell, P. G. Kwiat, J. C. Bienfang, R. P. Mirin, E. Knill, S. W. Nam, *Strong Loophole-Free Test of Local Realism*, Phys. Rev. Lett. **115**, 250402 (2015)

[37] W. Rosenfeld, D. Burchardt, R. Garthoff, K. Redeker, N. Ortegel, M. Rau, H. Weinfurter, *Event-Ready Bell Test Using Entangled Atoms Simultaneously Closing Detection and Locality Loopholes*, Phys. Rev. Lett. **119**, 010402 (2017)

[38] S. Aerts, P. Kwiat, J.-Å. Larsson, and M. Żukowski, *Two-Photon Franson-Type Experiments and Local Realism*, Phys. Rev. Lett. **83**, 2872 (1999)

[39] J.-Å. Larsson, *Loopholes in Bell inequality tests of local realism*, J. Phys. A: Math. Theor. **47**, 424003 (2014)

[40] J. Jogenfors, J.-Å. Larsson, *Energy-time entanglement, elements of reality, and local realism*, J. Phys. A: Math. Theor. **47**, 424032 (2014)

[41] J. Jogenfors, A. M. Elhassan, J. Ahrens, M. Bourennane, J.-Å. Larsson, *Hacking the Bell test using classical light in energy-time entanglement-based quantum key distribution*, Sci. Adv. **1**, e1500793 (2015)

[42] D. V. Strekalov, T. B. Pittman, A. V. Sergienko, Y. H. Shih, and P. G. Kwiat, *Postselection-free energy-time entanglement*, Phys. Rev. A **54**, R1(R) (1996)

[43] J. T. Barreiro, N. K. Langford, N. A. Peters, and P G. Kwiat, *Generation of Hyperentangled Photon Pairs*, Phys. Rev. Lett. **95**, 260501 (2005)

[44] F. Steinlechner, S. Ecker, M. Fink, B. Liu, J. Bavaresco, M. Huber, T. Scheidl, and R. Ursin, *Distribution of high-dimensional entanglement via an intra-city free-space link*, Nat. Commun. **8**, 15971 (2017)

[45] A. Cabello, A. Rossi, G. Vallone, F. De Martini, P. Mataloni, *Proposed Bell Experiment with Genuine Energy-Time Entanglement*, Phys. Rev. Lett. **102**, 040401 (2009)

[46] G. Lima, G. Vallone, A. Chiuri, A. Cabello, P. Mataloni, *Experimental Bell-inequality violation without the postselection loophole*, Phys. Rev. **A 81**, 040101 (2010)

[47] G. Vallone, I. Gianani, E. B. Inostroza, C. Saavedra, G. Lima, A. Cabello, P. Mataloni, *Testing Hardy nonlocality proof with genuine energy-time entanglement*, Phys. Rev. A **83**, 042105 (2011)

[48] Á. Cuevas, G. Carvacho, G. Saavedra, J. Cariñe, W. A. T. Nogueira, M. Figueroa, A. Cabello, P. Mataloni, G. Lima, G. B. Xavier, *Long-distance distribution of genuine energy-time entanglement*, Nat. Commun. **4**, 2871 (2013)

[49] G. Carvacho, J. Cariñe, G. Saavedra, Á. Cuevas, J. Fuenzalida, F. Toledo, M. Figueroa, A. Cabello, J.-Å. Larsson, P. Mataloni, G. Lima, G. B. Xavier, *Postselection-Loophole-Free Bell Test Over an Installed Optical Fiber Network*, Phys. Rev. Lett. **115**, 030503 (2015)

[50] J.-Å. Larsson, R. D. Gill, *Bell's inequality and the coincidence-time loophole*, Europhys. Lett. **67**, 707-713 (2004)

[51] I. Marcikic, H. de Riedmatten, W. Tittel, H. Zbinden, N. Gisin, *Long-distance teleportation of qubits at telecommunication wavelengths*, Nature **421**, 509-513 (2003)

[52] S. Braunstein, C. M. Caves, *Wringing out better Bell inequalities*, Ann. Phys. **202**, 22 (1990)

[53] M. Tomasin, E. Mantoan, J. Jogenfors, G. Vallone, J.-Å. Larsson, P. Villoresi, *High-visibility time-bin entanglement for testing chained Bell inequalities*, Phys. Rev. A **95**, 032107 (2017)

[54] H. J. Kimble, *The quantum internet*, Nature **453**, 1023-1030 (2008)

[55] P. Sibson, J. E. Kennard, S. Stanisic, C Erven, J. L. O'Brien, M. G. Thompson, *Integrated silicon photonics for high-speed quantum key distribution*, Optica **4**, 172-177 (2017)

[56] V. Sorianello, M. Midrio, G. Contestabile, I. Asselberghs, J. Van Campenhout, C. Huyghebaert, I. Goykhman, A. K. Ott, A. C. Ferrari, M. Romagnoli, *Graphene-silicon phase modulators with gigahertz bandwidth*, Nat. Photonics **12**, 40-44 (2018)

[57] A. Acín, N. Gisin, L. Masanes, *From Bell's Theorem to Secure Quantum Key Distribution*, Phys. Rev. Lett. **97**, 120405 (2006)

[58] A. Acín, N. Brunner, N. Gisin, S. Massar, S. Pironio, V. Scarani, *Device-Independent Security of Quantum Cryptography against Collective Attacks*, Phys. Rev. Lett. **98**, 230501 (2007)

[59] A. Acín, L. Masanes, *Certified randomness in quantum physics*, Nature **540**, 213-219 (2016)

[60] R. Arnon-Friedman, F. Dupuis, O. Fawzi, R. Renner, T. Vidick, *Practical device-independent quantum cryptography via entropy accumulation*, Nat. Commun. **9**, 459 (2018)

[61] G. Vallone, D. Dequal, M. Tomasin, M. Schiavon, F. Vedovato, D. Bacco, S. Gaiarin, G. Bianco, V. Luceri, and P. Villoresi, *Satellite quantum communication towards GEO distances*, Proc. SPIE 9900, Quantum Optics, 99000J (April 29, 2016)

[62] C. Agnesi, F. Vedovato, M. Schiavon, D. Dequal, L. Calderaro, M. Tomasin, D. G. Marangon, A. Stanco, V. Luceri, G. Bianco, G. Vallone, P. Villoresi, *Exploring the boundaries of quantum mechanics: advances in satellite quantum communications*, Phil. Trans. R. Soc. A **376**, 20170461 (2018)

[63] L. Calderaro, C. Agnesi, D. Dequal, F. Vedovato, M. Schiavon, A. Santamato, V. Luceri, G. Bianco, G. Vallone and P. Villoresi, *Towards Quantum Communication from Global Navigation Satellite System*, Quantum Science and Technology *(in press);* preprint available at arXiv:1804.05022 [quant-ph] (2018)

[64] D. Rideout, T. Jennewein, G. Amelino-Camelia, T. F. Demarie, B. L. Higgins, A. Kempf, A. Kent, R. Laflamme, X. Ma, R. B. Mann, E. Martín-Martínez, N. C. Menicucci, J. Moffat, C. Simon, R. Sorkin, L. Smolin and D. R. Terno, *Fundamental quantum optics experiments conceivable with satellites-reaching relativistic distances and velocities*, Classical and Quantum Gravity **29**, 224011 (2012)

[65] D. E. Bruschi, T. C. Ralph, I. Fuentes, T. Jennewein and M. Razavi, *Spacetime effects on satellite-based quantum communications*, Phys. Rev. D **90**, 045041 (2014)

[66] L. M. K. Vandersypen, M. Steffen, G. Breyta, C. S. Yannoni, M. H. Sherwood and I. L. Chuang, *Experimental realization of Shor's quantum factoring algorithm using nuclear magnetic resonance*, Nature **414**, 883-887 (2001)

[67] B. Korzh, C. C. Wen Lim, R. Houlmann, N. Gisin, M. J. Li, D. Nolan, B. Sanguinetti, R. Thew and H. Zbinden, *Provably secure and practical quantum key distribution over 307 km of optical fibre*, Nat. Photonics **9**, 163-168 (2015)

[68] N. Sangouard, C. Simon, H. de Riedmatten and N. Gisin, *Quantum repeaters based on atomic ensembles and linear optics*, Rev. Mod. Phys. **83**, 33 (2011)

[69] J. G. Rarity, P. R. Tapster, P. M. Gorman and P. Knight, *Ground to satellite secure key exchange using quantum cryptography*, New J. Phys. **4**, 82 (2002)

[70] A. Tomaello, C. Bonato, V. Da Deppo, G. Naletto, and P. Villoresi, *Link budget and background noise for satellite quantum key distribution,* Adv. Space Res., **47**, 802 (2011)

[71] D. Bacco, M. Canale, N. Laurenti, G. Vallone, P. Villoresi, *Experimental quantum key distribution with finite-key security analysis for noisy channels*, Nat. Commun. **4**, 2363 (2013)

[72] R. Ursin, T. Jennewein, J. Kofler, J. M. Perdigues, L. Cacciapuoti, C. J. de Matos, M. Aspelmeyer, A. Valencia, T. Scheidl, A. Acin, C. Barbieri, G. Bianco, C. Brukner, J. Capmany, S. Cova, D. Giggenbach, W. Leeb, R. H. Hadfield, R. Laflamme, N. Lütkenhaus, G. Milburn, M. Peev, T. Ralph, J. Rarity, R. Renner, E. Samain, N. Solomos, W. Tittel, J. P. Torres, M. Toyoshima, A. Ortigosa-Blanch, V. Pruneri, P. Villoresi, I. Walmsley, G. Weihs, H. Weinfurter, M. Zukowski and A. Zeilinger, *Space-quest, experiments with quantum entanglement in space*, Europhysics News **40** (3), 26-29 (2009)

[73] T. Scheidl, E. Wille, and R. Ursin, *Quantum optics experiments using the International Space Station: a proposal*, New J. Phys. **15**, 043008 (2013)

[74] T. Jennewein, C. Grant, E. Choi, C. Pugh, C. Holloway, J. P. Bourgoin, H. Hakima, B. Higgins and R. Zee, *The NanoQEY mission: ground to space quantum key and entanglement distribution using a nanosatellite*, Proc. SPIE 9254, Emerging Technologies in Security and Defence II; and Quantum-Physics-based Information Security III, 925402 (2014)

[75] S. K. Joshi, J. Pienaar, T. C. Ralph, L. Cacciapuoti, W. McCutcheon, J. Rarity, D. Giggenbach, J. G. Lim, V. Makarov, I. Fuentes, T. Scheidl, E. Beckert, M. Bourennane, D. E. Bruschi, A. Cabello, J. Capmany, A. Carrasco-Casado, E. Diamanti, M. Dušek, D. Elser, A. Gulinatti, R. H. Hadfield, T. Jennewein, R. Kaltenbaek, M. A. Krainak, H.-K. Lo, C. Marquardt, G. Milburn, M. Peev, A. Poppe, V. Pruneri, R. Renner, C. Salomon, J. Skaar, N. Solomos, M. Stipčević, J. P. Torres, M. Toyoshima, P. Villoresi, I. Walmsley, G. Weihs, H. Weinfurter, A. Zeilinger, M. Żukowski and R. Ursin, *Space QUEST mission proposal: Experimentally testing decoherence due to gravity*, arXiv:1703.08036 [quant-ph] (2017)

[76] J. Yin, Y. Cao, Y.-H. Li, S.-K. Liao, L. Zhang, J.-G. Ren, W.-Q. Cai, W.-Y. Liu, B. Li, H. Dai, G.-B. Li, Q.-M. Lu, Y.-H. Gong, Y. Xu, S.-L. Li, F.-Z. Li, Y.-Y. Yin, Z.-Q. Jiang, M. Li, J.-J. Jia, G. Ren, D. He, Y.-L. Zhou, X.-X. Zhang, N. Wang, X. Chang, Z.-C. Zhu, N.-L. Liu, Y.-A. Chen, C.-Y. Lu, R. Shu, C.-Z. Peng, J.-Y. Wang and J.-W. Pan, *Satellite-based-entanglement distribution over 1200 kilometers*, Science **356** (6343), 1140-1144 (2017)

[77] J.-G. Ren, P. Xu, H.-L. Yong, L. Zhang, S.-K. Liao, J. Yin, W.-Y. Liu, W.-Q. Cai, M. Yang, L. Li, K.-X. Yang, X. Han, Y.-Q. Yao, J. Li, H.-Y. Wu, S. Wan, L. Liu, D.-Q. Liu, Y.-W. Kuang, Z.-P. He, P. Shang, C. Guo, R.-H. Zheng, K. Tian, Z.-C. Zhu, N.-L. Liu, C.-Y. Lu, R. Shu, Y.-A. Chen, C.-Z. Peng, J.-Y. Wang and J.-W. Pan, *Ground-to-satellite quantum teleportation*, Nature **549**, 70-73 (2017)

[78] S.-K. Liao, W.-Q. Cai, W.-Y. Liu, L. Zhang, Y. Li, J.-G. Ren, J. Yin, Q. Shen, Y. Cao, Z.-P. Li, F.-Z. Li, X.-W. Chen, L.-H. Sun, J.-J. Jia, J.-C. Wu, X.-J. Jiang, J.-F. Wang, Y.-M. Huang, Q. Wang, Y.-L. Zhou, L. Deng, T. Xi, L. Ma, T. Hu, Q. Zhang, Y.-A. Chen, N.-L. Liu, X.-B. Wang, Z.-C. Zhu, C.-Y. Lu, R. Shu, C.-Z. Peng, J.-Y. Wang and J.-W. Pan, *Satellite-to-ground quantum key distribution*, Nature **549**, 43-47 (2017)

[79] S.-K. Liao, W.-Q. Cai, J. Handsteiner, B. Liu, J. Yin, L. Zhang, D. Rauch, M. Fink, J.-G. Ren, W.-Y. Liu, Y. Li, Q. Shen, Y. Cao, F.-Z. Li, J.-F. Wang, Y.-M. Huang, L. Deng, T. Xi, L. Ma, T. Hu, L. Li, N.-L. Liu, F. Koidl, P. Wang, Y.-A. Chen, X.-B. Wang, M. Steindorfer, G. Kirchner, C.-Y. Lu, R. Shu, R. Ursin, T. Scheidl, C.-Z. Peng, J.-Y. Wang, A. Zeilinger and J.-W. Pan, *Satellite-Relayed Intercontinental Quantum Network*, Phys. Rev. Lett **120**, 030501 (2018)

[80] F. Vedovato, C. Agnesi, M. Schiavon, D. Dequal, L. Calderaro, M. Tomasin, D. G. Marangon, A. Stanco, V. Luceri, G. Bianco, G. Vallone and P. Villoresi, *Extending Wheeler's delayed-choice experiment to space*, Sci. Adv. **3**, e1701180 (2017)

[81] R. Bedington, J. M. Arrazola and A. Ling, *Progress in satellite quantum key distribution*, npj Quantum Information **3**, 30 (2017)

[82] I. Khan, B. Heim, A. Neuzner and C. Marquardt, *Satellite-Based QKD*, Optics and Photonics News **29**, 26-33 (2018)

[83] C. Bonato, M. Aspelmeyer, T. Jennewein, C. Pernechele, P. Villoresi and A. Zeilinger, *Influence of satellite motion on polarization qubits in a Space-Earth quantum communication link*, Opt. Express **14**, 10050-10059 (2006)

[84] G. Vallone, D. Bacco, D. Dequal, S. Gaiarin, V. Luceri, G. Bianco and P. Villoresi, *Experimental satellite quantum communications*, Phys. Rev. Lett. **115**, 040502 (2015)

[85] C. H. Bennett and G. Brassard, *Quantum cryptography: Public key distribution and coin tossing*, Theoretical Computer Science **560**, 7-11 (2014)

[86] A. Carrasco-Casado, H. Kunimori, H. Takenaka, T. Kubo-Oka, M. Akioka, T. Fuse, Y. Koyama, D. Kolev, Y. Munemasa and M. Toyoshima, *LEO-to-ground polarization measurements aiming for space QKD using Small Optical TrAnsponder (SOTA)*, Optics Express **24**, 12254-12266 (2016)

[87] H. Takenaka, A. Carrasco-Casado, M. Fujiwara, M. Kitamura, M. Sasaki and M. Toyoshima, *Satellite-to-ground quantum-limited communication using a 50-kg-class microsatellite*, Nat. Photonics **11**, 502-508 (2017)

[88] H.-K. Lo, X. Ma and K. Chen, *Decoy State Quantum Key Distribution*, Phys. Rev. Lett. **94**, 230504 (2005)

[89] G. Vallone, D. Dequal, M. Tomasin, F. Vedovato, M. Schiavon, V. Luceri, G. Bianco and P. Villoresi, *Interference at the Single Photon Level Along Satellite-Ground Channels*, Phys. Rev. Lett. **116**, 253601 (2016)

[90] D. Dequal, G. Vallone, D. Bacco, S. Gaiarin, V. Luceri, G. Bianco and P. Villoresi, *Experimental single-photon exchange along a space link of 7000 km*, Phys. Rev. A **93**, 010301(R) (2016)

[91] K. Günthner, I. Khan, D. Elser, B. Stiller, Ö. Bayraktar, C. R. Müller, K. Saucke, D. Tröndle, F. Heine, S. Seel, P. Greulich, H. Zech, B. Gütlich, S. Philipp-May, C. Marquardt and G. Leuchs, *Quantum-limited measurements of optical signals from a geostationary satellite*, Optica **4**, 611-616 (2017)

[92] P. Villoresi, T. Jennewein, F. Tamburini, M. Aspelmeyer, C. Bonato, R. Ursin, C. Pernechele, V. Luceri, G. Bianco, and A. Zeilinger, *Experimental verification of the feasibility of a quantum channel between space and Earth*, New J. Phys. **10**, 033038 (2008)

[93] G. Bianco, R. Devoti, V. Luceri, and C. Sciarretta, *A Review Of Slr Contributions To Geophysics In Eurasia By Cgs*, Surveys in Geophysics 22: 481 (2001)

[94] M.R. Pearlman, J.J Degnan, and J.M. Bosworth, *The International Laser Ranging Service*, Advances in Space Research **30**, 135-143 (2002)

[95] J. J. Degnan, *Millimiter Accuracy Satellite Laser Ranging: A Review*, Geodynamics Series **25**, 133 (1993)

[96] *Handbook of Satellite Applications*, J. N. Pelton, S. Madry and S. Camacho-Lara, Eds. (Springer, 2017)

[97] D. Roddy, *Satellite Communications, Fourth Edition*, McGraw-Hill (2006)

[98] *The SAGE Handbook of Remote Sensing*, T. A. Warner, M. D. Nellis and G. M. Foody, Eds. (SAGE Publishing, 2009)

[99] S.-Y. Tan, *Meteorological Satellite Systems*, Springer (2014)

[100] *Springer Handbook of Global Navigation Satellite Systems*, P. J. G. Teunissen and O. Montenbruck, Eds. (Springer, 2017)

[101] *Near Earth Laser Communications*, H. Hemmati, Ed. (CRC Press, 2009)

[102] M. Pfennigbauer, W. R. Leeb , M. Aspelmeyer, T. Jennewein and A. Zeilinger, *Free-Space Optical Quantum Key Distribution Using Intersatellite Links*, Proceedings of the CNES - Intersatellite Link Workshop (2003)

[103] A. Tomaello, A. Dall'Arche, G. Naletto and P. Villoresi, *Intersatellite quantum communication feasibility study*, Proc. SPIE 8163, Quantum Communications and Quantum Imaging IX, 816309 (2011)

[104] F. Gerlin, N. Laurenti, G. Naletto, G. Vallone, P. Villoresi, L. Bonino, S. Mottini and Z. Sodnik, *Design optimization for quantum communications in a GNSS intersatellite network*, International Conference on Localization and GNSS (ICL-GNSS) (2013)

[105] R. Zajdel, K. Sosnica and G. Bury, *A New Online Service for the Validation of Multi-GNSS Orbits Using SLR*, Remote Sens. **9**, 1049 (2017)

[106] T. W. Murphy and S. D. Goodrow, *Polarization and far-field diffraction patterns of total internal reflection corner cubes*, Appl. Opt. **52**, 117-126 (2013)

[107] D. A. Arnold, *Method of Calculating Retroreflector-Array Transfer Functions*, SAO Special Report **382** (1979)

[108] T. Otsubo, G. M. Appleby and P. Gibbs, *Glonass Laser Ranging Accuracy With Satellite Signature Effect*, Surveys in Geophysics **22**, 509-516 (2001)

[109] O. Montenbruck, R. Schmid, F. Mercier, P. Steigenberger, C. Noll, R. Fatkulin, S. Kogure and A.S. Ganeshan, *GNSS satellite geometry and attitude models*, Advances in Space Research **56**, 1015-1029 (2015)

[110] G. Kirchner, L. Grunwaldt, R. Neubert, F. Koidl, M. Barschke, Z. Yoon, H. Fiedler, C. Hollenstein, *Laser Ranging to Nano Satellites in LEO Orbits: Plans, Issues, Simulations*, Proceedings, 18th International Workshop on Laser Ranging (Fujiyoshida, Japan 2013)

[111] W.-Y. Hwang, *Quantum Key Distribution with High Loss: Toward Global Secure Communication*, Phys. Rev. Lett. **91**, 057901 (2003)

[112] H.-K. Lo, X. Ma, K. Chen, *Decoy State Quantum Key Distribution*, Phys. Rev. Lett. **94**, 230504 (2005)

[113] T. Schmitt-Manderbach, H. Weier, M. Fürst, R. Ursin, F. Tiefenbacher, T. Scheidl, J. Perdigues, Z. Sodnik, C. Kurtsiefer, J. G. Rarity, A. Zeilinger, and H. Weinfurter, *Experimental Demonstration of Free-Space Decoy-State Quantum Key Distribution over 144 km*, Phys. Rev. Lett. **98**, 010504 (2007)

[114] J.-Y. Wang *et al.*, *Direct and full-scale experimental verifications towards ground-satellite quantum key distribution*, Nat. Photonics **7**, 387-393 (2013)

[115] S. Nauerth *et al.*, *Air-to-ground quantum communication*, Nat. Photonics **7**, 382-386 (2013)

[116] S.-K. Liao *et al.*, *Long-distance free-space quantum key distribution in daylight towards inter-satellite communication*, Nat. Photonics **11**, 509-513 (2017)

[117] Z. Wei *et al.*, *Decoy-state quantum key distribution with biased basis choice* Scientific Reports **3**, 2453 (2013)

[118] C. H. Bennet, G. Brassard, in *Proceedings of the IEEE International Conference on Computers, Systems and Signal Processing*, Bangalore, India (IEEE, New York), pp. 175-179 (1984)

[119] N. Bohr, *Can Quantum-Mechanical Description of Physical Reality Be Considered Complete?*, Phys. Rev. **48**, 696 (1935)

[120] G. I. Taylor, *Interference fringes with feeble light*, Proceedings of the Cambridge Philosophical Society **15**, 114 (1909)

[121] P. Grangier, A. Aspect, and J. Vigue, *Quantum Interference Effect for Two Atoms Radiating a Single Photon*, Phys. Rev. Lett. **54**, 418 (1985)

[122] C. Jönsson, *Electron Diffraction at Multiple Slits*, Am. J. Phys. **42**, 4 (1974)

[123] H. Rauch and S. A. Werner, *Neutron Interferometry*, OUP Oxford (2015)

[124] S. Eibenberger, S. Gerlich, M. Arndt, M. Mayor, and J. Tüxen, *Matter-wave interference of particles selected from a molecular library with masses exceeding 10,000 amu*, Phys. Chem. Chem. Phys., **15**, 14696 (2013)

[125] A. P. French, *Special Relativity, The M.I.T Introductory Physics Series*, W.W. Norton and Company Inc. (1966)

[126] L. D. Landau, E. M. Lifshitz, *The Classical Theory of Fields*, Pergamon Press (1975)

[127] I. Capraro, A. Tomaello, A. Dall'Arche, F. Gerlin, R. Ursin, G. Vallone, and P. Villoresi, *Impact of Turbulence in Long Range Quantum and Classical Communications*, Phys. Rev. Lett. **109**, 200502 (2012)

[128] M. Zych, F. Costa, I. Pikovski, and Č. Brukner, *Quantum interferometric visibility as a witness of general relativistic proper time*, Nat. Commun. **2**, 505 (2011)

[129] R. Colella, A. W. Overhauser, and S. Werner, *Observation of gravitationally induced quantum interference*, Phys. Rev. Lett. **34**, 1472 (1975)

[130] G. Ghirardi, R. Grassi, and A. Rimini, *Continuous-spontaneous-reduction model involving gravity*, Phys. Rev. A **42**, 1057 (1990)

[131] N. Bohr, *Discussion with Einstein on epistemological problems in atomic physics*, in *Quantum Theory and Measurement*, edited by J. A. Wheeler and W. H. Zurek (Princeton University Press, New Jersey, 1984), pp 9–49

[132] A. Einstein, B. Podolsky, and N. Rosen, *Can Quantum-Mechanical Description of Physical Reality Be Considered Complete?*, Phys. Rev. **47**, 777 (1935)

[133] N. Bohr, *Can Quantum-Mechanical Description of Physical Reality be Considered Complete?*, Phys. Rev. **48**, 696 (1935)

[134] N. Bohr, *The Quantum Postulate and the Recent Development of Atomic Theory*, Nature **121**, 580-590 (1928)

[135] J. A. Wheeler, *The "Past" and the "Delayed-Choice" Double-Slit Experiment*, in *Mathematical Foundations of Quantum Theory*, edited by A. R. Marlow (Academic Press, New York, 1978), pp. 9-48

[136] J. A. Wheeler, *Law without law*, in *Quantum Theory and Measurement*, edited by J. A. Wheeler and W. H. Zurek (Princeton University Press, New Jersey, 1984), pp. 182-213

[137] V. Jacques, E Wu, F. Grosshans, F. Treussart, P. Grangier, A. Aspect, J.-F. Roch, *Experimental Realization of Wheeler's Delayed-Choice Gedanken Experiment*, Science **315**, 966-968 (2007)

[138] X. Ma, J. Kofler, and A. Zeilinger, *Delayed-choice gedanken experiments and their realizations*, Rev. Mod. Phys. **88**, 015005 (2016)

[139] M. O. Scully and K. Drühl, *Quantum eraser: A proposed photon correlation experiment concerning observation and "delayed choice" in quantum mechanics*, Phys. Rev. A **25**, 2208 (1982)

[140] M. O. Scully, B-G. Englert, and H. Walther, *Quantum optical tests of complementarity*, Nature **351**, 111-116 (1991)

[141] R. Ionicioiu and D. R. Terno, *Proposal for a Quantum Delayed-Choice Experiment*, Phys. Rev. Lett. **107**, 230406 (2011)

[142] J.-S. Tang, Y.-L. Li, X.-Ye Xu, G.-Y. Xiang, C.-F. Li, and G.-C. Guo, *Realization of quantum Wheeler's delayed-choice experiment*, Nat. Photonics **6**, 600-604 (2012)

[143] A. Peruzzo, P. Shadbolt, N. Brunner, S. Popescu, J. L. O'Brien, *A Quantum Delayed-Choice Experiment*, Science **338**, 634-637 (2012)

[144] F. Kaiser, T. Coudreau, P. Milman, D. B. Ostrowsky, S. Tanzilli, *Entanglement-Enabled Delayed-Choice Experiment*, Science **338**, 637-640 (2012)

[145] M. Stipčević and B. M. Rogina, *Quantum random number generator based on photonic emission in semiconductors*, Rev. Sci. Instrum. **78**, 045104 (2007)

[146] M. Zukowski, A. Zeilinger, M. A. Horne, and A. K. Ekert, *"Event-ready-detectors" Bell experiment via entanglement swapping*, Phys. Rev. Lett. **71**, 4287 (1993)

[147] X.-S. Ma, S. Zotter, J. Kofler, R. Ursin, T. Jennewein, Č. Brukner, and A. Zeilinger, *Experimental delayed-choice entanglement swapping*, Nature Physics **8**, 479-484 (2012)

[148] T. Zhong, H. Zhou, R. Horansky, C. Lee, V. B. Verma, A. E. Lita, A. Restelli, J. C. Bienfang, R. P. Mirin, T. Gerrits, S. W. Nam, F. Marsili, M. D. Shaw, Z. Zhang,

L. Wang, D. Englund, G. W. Wornell, J. H. Shapiro, F. N. .C. Wong, *Photon-Efficient High-Dimensional Quantum Key Distribution*, New J. Phys. **17**, 022002 (2015)

[149] A. Cabello, *Bipartite Bell Inequalities for Hyperentangled States*, Phys. Rev. Lett. **97**, 140406 (2006)

[150] M. Barbieri, F. De Martini, P. Mataloni, G. Vallone, A. Cabello, *Enhancing the violation of the Einstein-Podolsky-Rosen local realism by quantum hyper-entanglement*, Phys. Rev. Lett. **97**, 140407 (2006)

[151] T. Graham, C. Zeitler, J. Chapman, P. Kwiat, H. Javadi, and H. Bernstein, *Superdense teleportation and quantum key distribution for space applications*, 2015 IEEE Int. Conf. Sp. Opt. Syst. Appl. ICSOS 2015, pp. 1-7, 2016

[152] D. Alighieri, *Commedia* (1321)

[153] D. R. Terno, F. Vedovato, M. Schiavon, A. R. H. Smith, P. Magnani, G. Vallone, and P. Villoresi, *Proposal for an Optical Test of the Einstein Equivalence Principle*, arXiv:1811.04835 [gr-qc] (2018)

Ringraziamenti

Prima di tutti, voglio sinceramente ringraziare il mio supervisore prof. Paolo Villoresi per avermi dato la possibilità di lavorare nel gruppo *QuantumFuture* prima durante la tesi magistrale e poi durante il dottorato. E' stata un'esperienza molto gratificante, formativa ed estremamente stimolante dal punto di vista scientifico e lavorativo, ma anche un'incredibile opportunità di crescita personale. Non dimenticherò mai le riunioni annunciate il giorno prima, le deadline improbabili, la lotta alla burocrazia, le tecniche di allineamento non-standard ma efficaci, l'instancabile passione e dedizione per il suo lavoro, la capacità di tenere alto l'umore del gruppo.

Certo, lavorare in questo gruppo non sarebbe stata la stessa cosa senza la costante (figlio permettendo) presenza del prof. Giuseppe Vallone (Pino), capace di rinnovare e rinvigorire la passione per la fisica, dura e pura, con poche parole, ma dette molto bene. Penso sinceramente che Pino sia un genio, lui le cose *le vede* (e guida pure i kart da paura!).

Un ringraziamento sincero è dovuto al prof. Giampiero Naletto, direttore del corso di dottorato del CISAS, per il continuo sostegno che ha dato a tutti noi studenti e lo sforzo compiuto per far sì che questo corso di dottorato non chiuda i battenti.

Ringrazio di cuore la mia famiglia, a cominciare da mio papà Redi, mia mamma Stefania e mia sorella Elisabetta, a cui questa tesi é dedicata, i miei nonni, gli zii e i cugini tutti.

Vengo poi ai miei colleghi del Luxor, in ordine sparso: Costantino Agnesi, impareggiabile compagno di gran parte delle avventure scientifiche, per i suoi continui oscillamenti, gli incazzamenti e le morbide carezze; Luca Calderaro, per i suoi codici ben scritti, l'eleganza e la pacatezza disarmanti, anche se alla fine si é smollato anche lui; Marco Avesani (e tutta casa sua), perché senza di lui potremmo chiudere baracca domani, grazie davvero; il dott. Matteo Schiavon per le sue freddure, ma in fondo in fondo ha un cuore anche lui; il dott. Alberto(ne!) Santamato, belinooooooooo, per la sua insanabile voglia di fisica *whatsoever*; Alessia Scriminich, che é sempre bellissima e bravissima, pur stando troppo in America; Andrea Stanco, il presidente, che alla fine ha lavorato anche lui; la dott.ssa Alessandra Slemer (Slater), new-entry, ma già dei nostri, perché ride di gusto; il dott. Daniele Dequal, che é un vero ASI expert, per le grigliate a Jesolo e Padova tra le altre cose; il dott. Marco Tomasin, per l'elettronica creativa e i momenti condivisi in Quantum; il dott. Davide Giacomo Marangon per la sua integrità e la sua abnegazione, che bravo che é Davide Giacomo;

il dott. Davide Bacco, Cosí Unico, Eclettico e Abile, guai a non menzionarlo; il dott. Simone Gaiarin, perchè comunque usiamo ancora i suoi codici; il dott. Alberto Donazzan, un maestro per tante cose; il dott. Enrico Tessarolo, perché come dice certe cose lui non può dirle nessun altro.

Come non ringraziare poi il Civico e le sue bariste, l'Anytime che é bbbuona; il bar Agli Amici, perchè ogni tanto bisogna anche cambiare; il Berlino che non ci fa più giocare ai dadi; la Cantina del Gufo anche se é imbucata; le piadine che poi hanno chiuso, il pastaro che ha chiuso anche lui, il Maniaco che non chiuderà mai; Idea Pizza e i rotolini che però te ne servono due; Giacomino, fratello, le trote smerigliate, i canederli, il Brenta, il tornio, il Goto e il Plan, Lea e Mara; Fabio e Marialaura, viva!, grazie di avermi accettato in casa; Mirko Pittaluga e sua sorella; Giacomo Pantaleoni che mi ha fatto tanta compagnia; Giulio Foletto che ride ai meme; Kza e il lavoro che lo rende contento; Yale e Ancona che é bellissima; Livio che sta a Padova ma non ci vediamo mai; Mionz e il Fernet; Zane che qualche grigliata in più potrebbe farla; Dega e Omar che anche se li vedo poco comunque ci sono; Gio, perchè é Gio; Enrico e le 4 serate in a row; le coinquiline di Marco: Olimpia, Chiara e Giulia che sono fantastiche; Giulia per averla ritrovata a Padova dopo tanto e Alessandra per averla conosciuta; Elena e le amiche chioggiotte non so perchè; i bixime-baxime di Piero; la Sagra dei Mussi, la sagra del Bordugo a casa di Giacomo e la Sagra dei Laser a Monaco; Trombone Shorty per essere venuto a Fiorenzuola; i Bud Spencer Blues Explosion che spaccano; Paolone Nutini e Candy; The Sound of Silence fatta dai Disturbed; De André, Guccini e Dalla; la Zanzara, Cruciani, Parenzo e quelli che chiamano; il vecchio da Milano; l'Abbazia di Montescaglioso, padre Peppe e Franco Caputo, il prossimo sindaco (speriamo) di Montescagliato Francesco e sua moglie Elisabetta; Fortunato della mensa di MLRO; la Festa della Bruna; Pippo e Cinzia per l'ospitalità; l'operatore di MLRO quello bravo che ci ha fatto fare tutti gli esperimenti, Rosy Abate che distraeva gli altri; le norme di sicurezza; Nicola e il Gran Casale, che non ci dobbiamo preoccupare in qualche modo facciamo; Matteo e Leo per i carichi di viveri, Dilena e la sua stracciatella, le macellerie di Santeramo, dove i cavalli vivi sono cavalli crudi, i fornelli di Laterza, i sassi di Matera, le Botteghe, Stano e l'Osteria Lucana; CF; Carlo Rovelli per avermi ospitato; Danny Terno con cui ho anche lavorato; e infine Ajisai, che se non lo prendi *chiudi la cupola e te ne vai*.